Technical Report

Introduction to DLBreach – A Simplified Physically-Based Dam/Levee Breach Model

(Version 2016.4)

Weiming Wu, PhD
Professor

Department of Civil and Environmental Engineering
Clarkson University
Box 5710, 8 Clarkson Avenue
Potsdam, NY 13699, USA

April 26, 2016

Disclaimer

The DLBreach model (Version 2016.4) was developed by Dr. Weiming Wu, Department of Civil and Environmental Engineering, Clarkson University, NY, USA. A user is required engineering expertise to use DLBreach correctly. The reliability and accuracy of any results obtained from DLBreach should be carefully examined by experienced engineers.

In no event shall Dr. Weiming Wu and Clarkson University be liable for lost profits or any special, incidental or consequential damages arising out of or in connection with use of DLBreach regardless of cause.

Table of Contents

Chapter 1. Introduction

Embankments, such as dams, levees, dikes and barriers, have been widely used for flood defense along rivers, lakes and coastal lines all over the world. However, these structures may fail due to various trigger mechanisms, such as overtopping, piping, and foundation defects, particularly under extreme weather conditions. Failures of these structures may generate disastrous floods causing loss of human lives, damage of properties and infrastructure, and interruption of their services. Understanding and modeling of the embankment failure processes is crucial for risk assessment and decision making.

Embankments can be classified as non-erodible (concrete), erodible (earth/rock), or of the mixed type. Manmade dams may be constructed with one of these but are mostly built as homogeneous or zoned earthfill, rockfill with a clay core and/or a concrete face. According to the U.S. Committee on Large Dams (1975), almost 80% of the large dams in the U.S. were formed by embankments constructed from natural erodible materials. Landslide dams are usually comprised of erodible earth and rock materials. Most levees and dikes are constructed using clay, silt or sand with a clay core or cover, often on a foundation of erodible substrata. Natural coastal barriers often consist mostly of sandy material (ASCE/EWRI Task Committee 2011).

Embankment failures are very sensitive to the structures' materials and configurations, impacting forces, and other environmental factors. In general, a concrete embankment is prone to fail instantaneously (break) when the entire structure or only a portion loses stability under certain loading conditions; thus, the breach dimensions are often determined based on structural stability analysis and the resulting flood can then be simulated using numerical tools. An earth embankment, however, is likely to fail gradually (breaching) due to erosion of its materials by water flow or wave action involving mixed-regime flows, strong sediment transport and rapid morphological changes. Therefore, determination of the earth embankment breach characteristics (width, shape, peak outflow, failure time) is quite complex and challenging, requiring the prediction of complex interactions between soil, water, and structure (ASCE/EWRI Task Committee 2011).

In the last decades, numerous models have been developed for prediction of earthen embankment breaching processes. These models can be classified as parametric, simplified and detailed multidimensional physically-based breach models (ASCE/EWRI Task Committee 2011). The parametric breach models estimate the breach width, breach side slope, peak outflow and failure time using regression equations statistically derived based on data from dozens of historic dam failures, without considering the detailed breaching processes (e.g., MacDonald and Langridge-Monopolis 1984; Froehlich 1995; Walder and O'Connor 1997; Xu and Zhang 2009). In the simplified physically-based breach models, the breach cross-section is usually simplified as a rectangle, trapezoid or triangle, the flow at the breach is estimated using the broad-crested weir relation, and the erosion is estimated using different simplified models (e.g., Fread 1984; Singh and Scarlatos 1985). Multidimensional physically-based models simulate in more detail

the flow and morphodynamic processes due to embankment breaching (Broich 1998; Wang and Bowles 2006; Faeh 2007; Wu et al. 2012; Marsooli and Wu 2015). Because embankment breach flows are usually in mixed flow regimes and with discontinuities, the numerical schemes often used are shock-capturing approximate Riemann solvers and Total Variation Diminishing schemes in 1-D and depth-averaged 2-D models (e.g., Wu et al. 2012) and volume-of-fluid and smooth particle hydrodynamics methods in vertical 2-D and 3-D models (e.g., Shigematsu et al. 2004; Marsooli and Wu 2015).

Because the parametric breach models consider only the characteristic parameters rather than the involved physical processes and the multidimensional detailed models are relatively costly to use, the simplified physically-based breach models are attractive for engineering application. The simplified models may be based on either analytical or numerical solutions. To derive the analytical solutions, simplifications have to be made by approximating the reservoir rating curve with a linear or simple power function between the water level and surface area (or volume) and assuming the erosion rate at the breach to be a power function of the flow velocity (Singh and Scarlatos 1988; Rozov 2003; Franca and Almeida 2004) or shear stress (Macchione 2008). Such simplifications limit the applicability of the analytical models. Therefore, better approximations have been used in the numerically-solved simplified breach models for dams (Cristofano 1965; Harris and Wagner 1967; Lou 1981; Ponce and Tsivoglou 1981; Nogueira 1984; Fread 1984 & 1988; Singh and Scarlatos 1985; Broich 1998; Temple et al. 2005&2006; Wang et al. 2006; Morris et al. 2009), sea dikes (Visser 1998; D'Eliso 2007), and barriers (Kraus and Hayashi 2005). The reservoir or bay characteristics are represented more accurately using the water level and surface area (or volume) curve, and the erosion at the breach is modeled using improved sediment transport models. However, most of the simplified breach models are based on local equilibrium bed-load sediment transport (Harris and Wagner 1967; Lou 1981; Nogueira 1984; Singh and Scarlatos 1985; Fread 1988), and only a few recent models have considered the breach formation by headcut erosion (Temple et al. 2005&2006; Zhu et al. 2006; D'Eliso 2007). Uncertainties in predicted breach parameters and the flood hydrograph exist due to significant model simplifications (Mohamed et al. 2002; ASCE/EWRI Task Committee 2011).

Presented in this report is a newly developed comprehensive simplified physically-based Dam and Levee Breach (DLBreach) model, which is able to simulate the breaching processes of non-cohesive and cohesive, homogeneous and composite embankments due to overtopping and piping. The model considers the non-equilibrium sediment transport from clear water in the reservoir to downstream turbid water, and simulates the cohesive embankment breach erosion processes in the form of headcut migration and the breaching of composite embankment with clay core and cover. The model handles dam and levee breaching by implementing different algorithms to determine the head and tail water levels and allowing embankment base erosion.

The first version of DLBreach was based on the journal article of Wu (2013), which considers only a one-direction breach or a breach by unidirectional flow. It is mostly used for dam breach and levee breach in inland rivers. In the case of coastal levee and barrier, the breach

can occur in two directions by either elevated bay water level by strong rainfall in the watershed or elevated sea water level by storm surge and waves. In addition, tide flow in an estuary or return flow from a floodplain cause flow reversal, which also affects the breach in two directions. Therefore, DLBreach is revised to consider a two-direction breach for the modeling of coastal and estuarine levee and barrier breaching. The present version of DLBreach can handle both one- and two-direction breaches. The technical details and validations of the model are described in the following chapters.

Chapter 2. Earthen Embankment Breaching and the Approximations

The most common mechanisms for earthen embankment failures are external erosion due to overtopping flow and internal erosion due to seepage and piping. The breach geometry differs for different failure modes (overtopping or piping), embankment materials (cohesive, non-cohesive or mixed), and structures (homogeneous or composite embankments). Each type of breach is approximated in DLBreach according to the breaching processes and characteristics as described below.

2.1. Embankment Breach by Overtopping

Overtopping flow or waves over an embankment can result in erosion on the crest and downstream face and then failure of the embankment. Overtopping may occur due to a variety of reasons, such as large inflows into the reservoir caused by excessive rainfall or by the failure of an upstream dam; extreme waves and surge; inadequate design, construction and maintenance of the structure; debris blockage in spillway and flood channel; and settlement of embankment crest.

Laboratory experiments and case studies have found that there is a distinct difference between the erosion processes of non-cohesive and cohesive earthen embankments due to overtopping flow (Pugh, 1985; Ralston, 1987; Powledge et al., 1989; Singh, 1996; Visser, 1998; Hanson et al., 2005). Thus, DLBreach uses different approximations for the geometries of non-cohesive and cohesive embankments, as well as the composite ones, as explained in the following subsections.

2.1.1. Homogeneous Non-cohesive Embankment Breach by Overtopping

As shown in Fig. 2.1, the critical overtopping erosion mode usually is progressive surface erosion (sediment transport in dispersed particles) for embankments with non-cohesive or loose cohesive without compaction. The breach bed erosion is often accompanied by lateral erosion and mass failure of side walls. When the embankment crest vanishes, the breach flow starts to increase significantly, and the breach is then further lowered and widened at a much higher rate until the headwater is depleted or the tailwater level increases to the headwater level.

DLBreach can handle both one- and two-way breaches. In the longitudinal direction, the breach is approximated as a flat top connected with straight slopes at upstream and downstream, as shown in Figs. 2.2-2.4. The flat top is the dam crest at the beginning of the breaching process. The upstream slope starts from the upstream toe and ends at the upstream edge of the crest. The downstream slope is from the downstream edge of the flat top to the downstream toe of the embankment. For a one-way breach, the upstream slope does not have erosion, whereas the breach top lowers by downcutting and its downstream edge advances upstream as the

downstream slope rotates about the downstream dam toe, as shown in Fig. 2.2. The approximation of the one-way breach is more clearly shown in Fig. 2.3 with a 3D view. For a two-way breach (Fig. 2.4), if the flow is from upstream to downstream, only the breach top and downstream slope have erosion and the upstream slope does not. If the flow reverses, erosion occurs only at the breach top and upstream slope have erosion.

Each of the three sections of the breach has a trapezoidal cross-section and constant bottom width along its course. The breach side slope is set as the same for the three sections, but the bottom widths of the three sections are different because the flow conditions are different. The upstream and downstream slopes should have a varying bottom width to continuously connect with the flat top reach, but for simplicity a constant bottom width is assumed so that a uniform flow can be assumed on each of the upstream and downstream slopes.

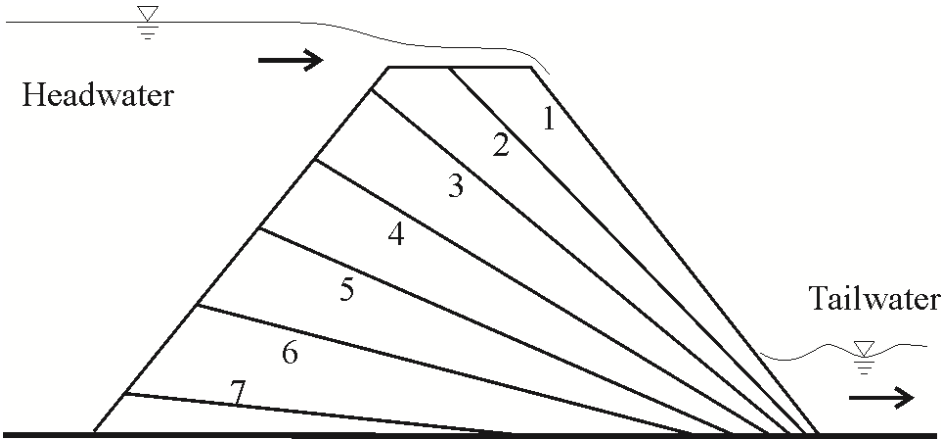

Fig. 2.1. Dam Breaching by Surface Erosion (Numbers denote time slots; after Hanson (2007))

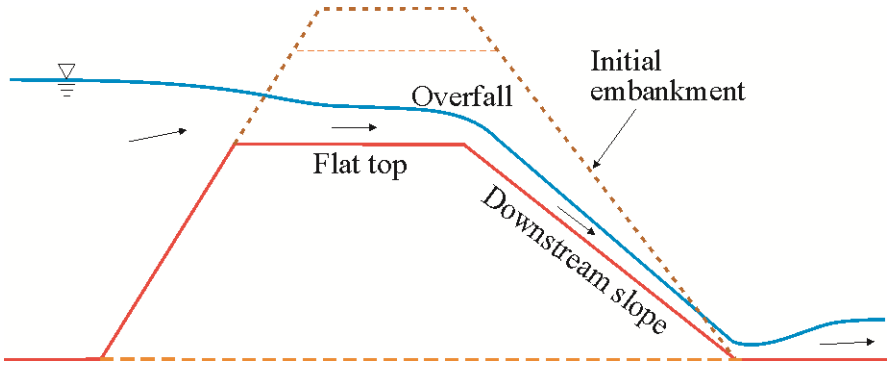

Fig. 2.2. Side View of One-Way Breach of Non-cohesive or Loose Earthen Embankment by Overtopping Approximated by DLBreach

The one-way breach was designed to simulate the breaching process of inland dams and levees, in which the breach flow is usually unidirectional from the reservoir or river to the

downstream channel or storage basin. The two-way breach is added to simulate coastal levee and barrier breaching, in which the flow can change direction. Now the one-way breach is actually set as a special case of the two-way breach in the DLBreach.

Though the model now still uses the terms “upstream” and “downstream” for the two sides of the embankment, the flow can be either from “upstream” to “downstream” or from “downstream” to “upstream” depending on whether the “upstream” or “downstream” side has higher water level. In the inland context, the reservoir or the river is set as the upstream side. In the coastal context, the user can set either the bay or seaside as the “upstream” side, as long as the input data are specified correctly.

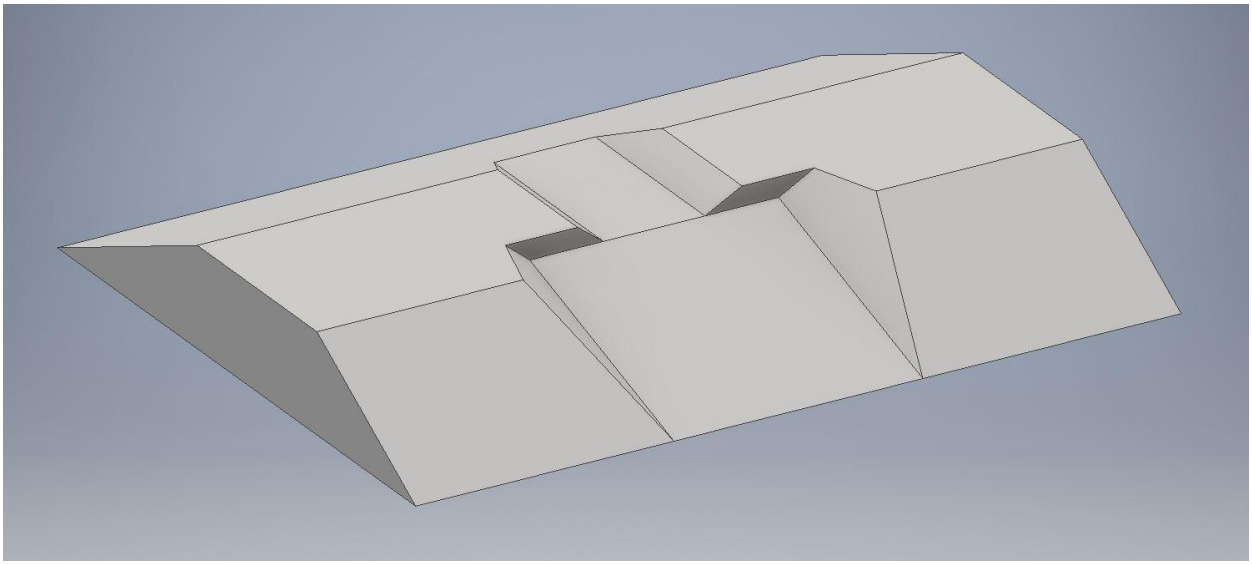

Fig. 2.3. 3D View of One-Way Breach of Non-cohesive or Loose Earthen Embankment by Overtopping Approximated by DLBreach

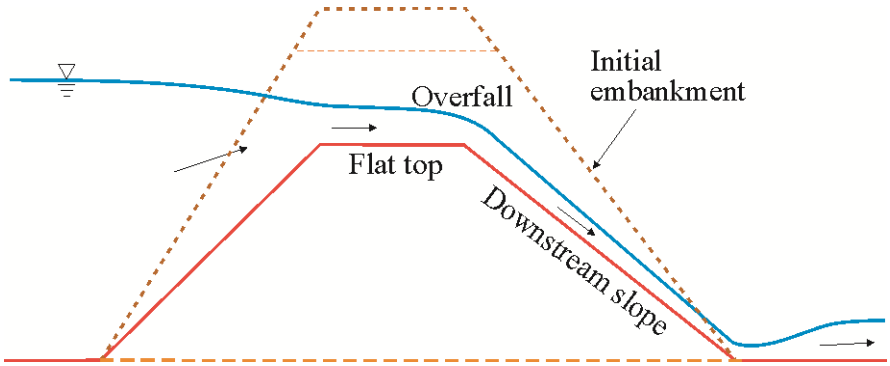

Fig. 2.4. Side View of Two-Way Breach of Non-cohesive or Loose Earthen Embankment by Overtopping Approximated by DLBreach

2.1.2. Homogeneous Cohesive Embankment Breach by Overtopping

Breaching of a cohesive or compacted non-cohesive embankment is more likely in the form of headcut migration (formation and migration of a vertical or nearly vertical drop on the bed). Initial overtopping flow results in sheet and rill erosion, with one or more master rills developing into a series of cascading overfalls and then a large headcut on the downstream slope, as illustrated in Figs. 2.5 and 2.6 (Hanson et al., 2005). Headcut advance is accompanied with breach downcutting and widening. As the headcut advances to the upstream slope, the embankment crest vanishes, and the breach flow increases significantly. Then, the breach further widens until the headwater is depleted or the tailwater level increases to the headwater level.

Fig. 2.5. Cohesive dam breaching by overtopping: (a) rills and cascade of small overfalls at t=7 min; (b) consolidation of small overfalls at t=13 min; (c) headcut at downstream crest at t=16 min; (d) headcut at upstream crest at t=31 min; (e) flow through breach at t=40 min; (f) transition to final breach stage at t=51 min (Experiment by Hanson et al., 2005)

Figs. 2.7 and 2.8 show the conceptualized geometry for this type of breach under unidirectional flow, which consists of a flat top and a downstream headcut. Overfall flow occurs

at the headcut. In nature, headcut migration consists of a series of discontinuous mass failure events. In DLBreach, the headcut is assumed to start at the downstream toe of the dam and migrates upstream gradually. The cross-sections of breach flat top and the section downstream of the headcut are approximated as trapezoidal, and undergo downcutting and widening.

For a two-way breach, the model approximates the breach as shown in Fig. 2.9. When the flow reverses, headcut occur on the other side of the breach. Therefore, two headcuts may exist. Each is assumed starting from the embankment toe.

Note that the point of transition between headcut and surface erosion modes is not well defined. Thus, DLBreach has two options for cohesive embankment breaching: one is the surface erosion mode shown in Fig. 2.4, and the other one is the headcut erosion mode shown in Fig. 2.9. Both options are available to the users. In general, cohesive embankment soil is compacted, and the headcut mode is suggested as the default option.

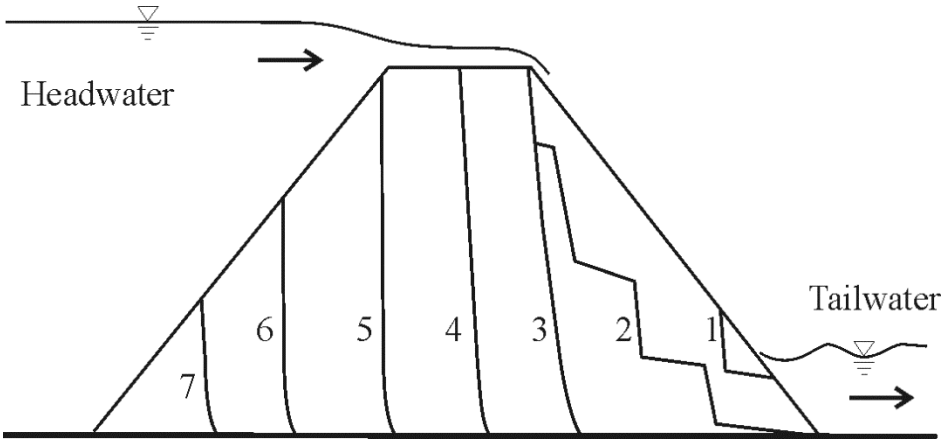

Fig. 2.6. Dam Breaching by Headcut Migration (Numbers denote time slots; after Ralston (1987) and Hanson et al. (2005))

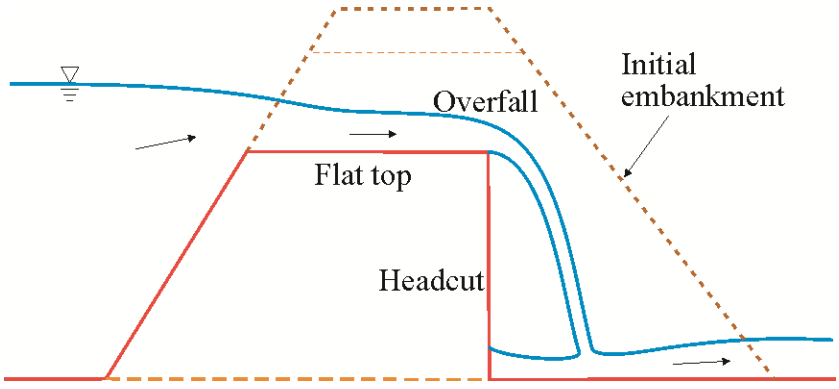

Fig. 2.7. Side View of One-Way Breach of Cohesive or Compacted Earthen Embankment by Overtopping

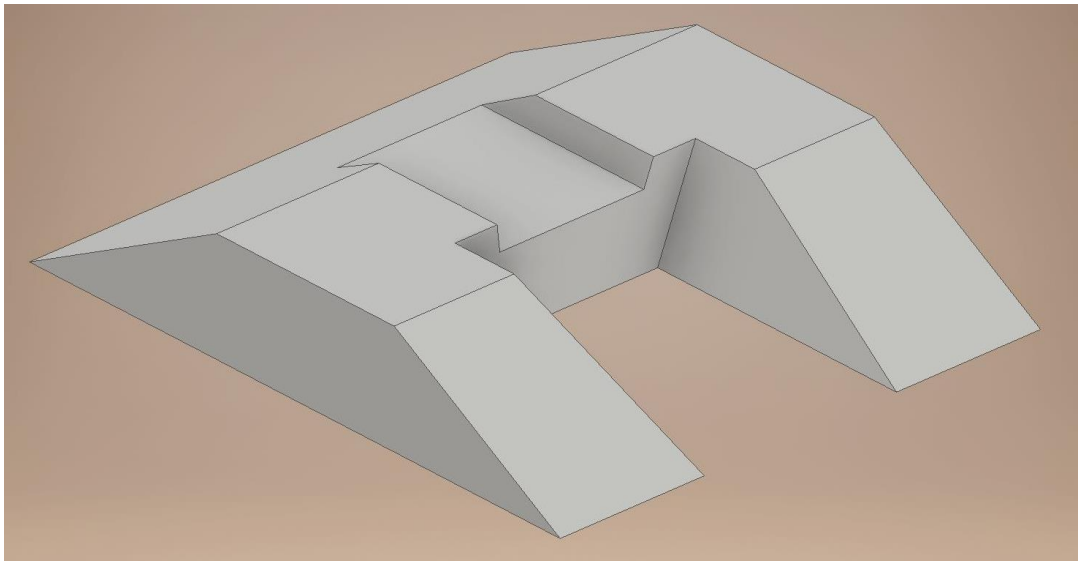

Fig. 2.8. 3D View of One-Way Breach of Cohesive or Compacted Earthen Embankment by Overtopping

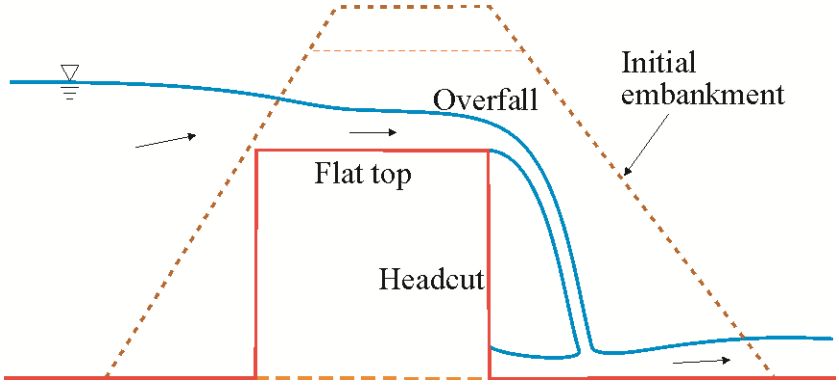

Fig. 2.9. Side View of Two-Way Breach of Cohesive or Compacted Earthen Embankment by Overtopping

2.1.3. Composite Embankment Breach by Overtopping

The overtopping failure of composite embankments differs from that of homogenous embankments (Tinney and Hsu, 1961; Chee, 1984; Pugh, 1985; Fletcher and Gilbert, 1992; Morris and Hansen, 2005; D'Eliso, 2007). For an embankment with a less erodible cover, overtopping flow may erode or damage the cover first, and then retrograde (headcut) erosion may start in the more erosive embankment body from the location where the cover is removed (D'Eliso, 2007). DLBreach considers a clay cover over the embankment shown in Fig. 2.10. The

erosion starts at the breach top and downstream slope. Once the clay cover is eroded away, the internal soil will start to erode.

When water overflows or waves overtop a composite embankment with an internal clay, steel or concrete core or a concrete floodwall on the crest, erosion starts on the embankment surface in form of either surface erosion or headcut migration until the core or floodwall is reached. This erosion may affect the stability of the core and floodwall and eventually lead to their respective failures. The likely failure mechanisms of the core and floodwall include sliding, overturning, and bending (Powledge et al., 1989; Fletcher and Gilbert, 1992; Mohamed et al., 2002; Allsop et al., 2007; Sills et al., 2008; Orendorff, 2009). The failed materials may be quickly washed out or relocated downstream by the increasing breach flow and then the breach channel may be further lowered by down cutting and widened by lateral erosion and mass failure.

DLBreach considers a composite embankment with a clay core, and applies the surface erosion model in the previous section to calculate the erosion caused by overtopping flow at the top flat breach channel and the downstream slope at the early stage before the clay core is exposed to the flow. Once the clay core is exposed, the longitudinal section of the breach is conceptualized as shown in Fig. 2.11 for one-way breach and Fig. 2.12 for two-way breach. The breach consists of a flat top and two downstream straight slopes corresponding to the core and shoulder materials in two sides.

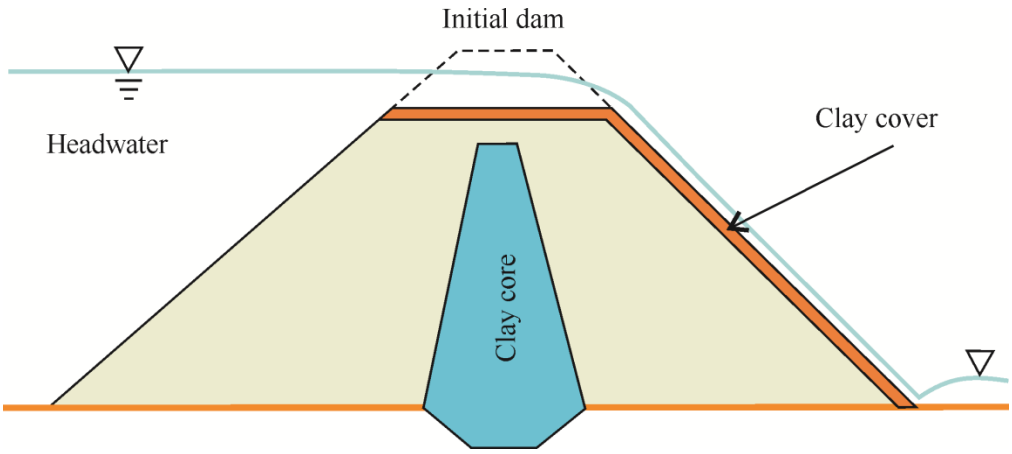

Fig. 2.10. Sketch of Overtopping Breach of a Composite Dam with Clay Core and Cover

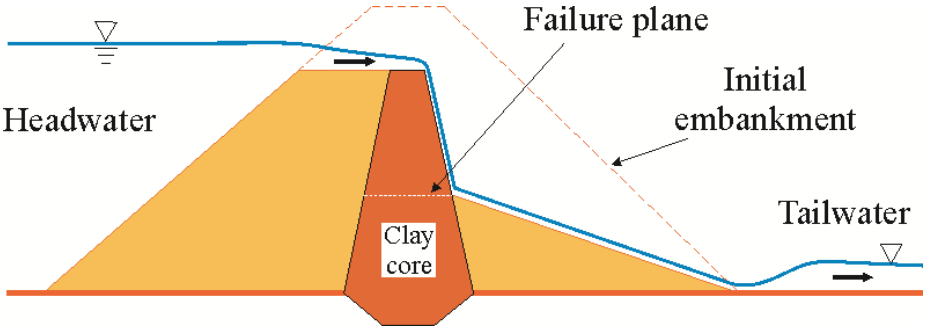

Fig. 2.11. One-Way Breach of a Composite Dam with Clay Core by Overtopping

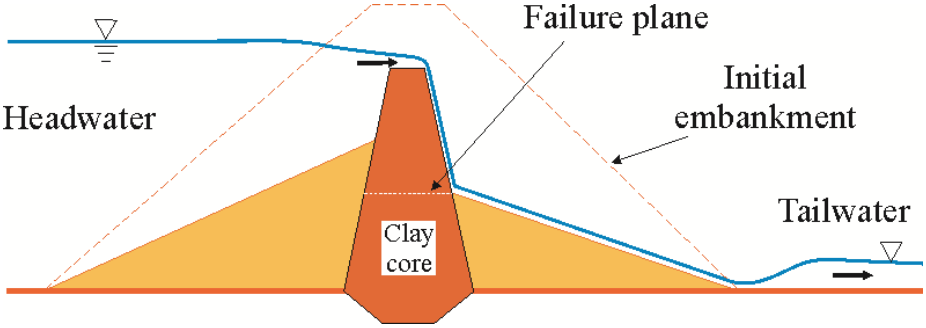

Fig. 2.12. Two-Way Breach of a Composite Dam with Clay Core by Overtopping

2.2. Embankment Breach by Piping

Failure by piping or internal erosion is the process by which seepage forces can result in the removal of fines along a path between the upstream and downstream faces. The pipe increases in diameter due to removal of material at the wall primarily due to shear stress forces until local collapse or slumping of the crest 'roof' occurs (Figs. 2.13-2.15). After the collapse of the crest, overtopping breach characteristics dominate, including down cutting and lateral widening. The Teton dam failure shown in Fig. 2.13 is a classic case of piping failure (Ponce, 1982). The typical piping failure process is documented in Fig. 2.14 observed through experiment (Hanson et al., 2010). Some case studies have shown that the pipe initiation and erosion stages may take several days or weeks, whereas the subsequent embankment breaching may take only few hours or less.

Piping and liquefaction may occur as just mentioned due to seepage or leakage flow through weak layers, desiccation cracks, structural joints, dead tree roots, and animal burrows in the embankment, without the necessity for the water level to have reached the full height of the embankment (Foster et al., 2000; Fell et al., 2003; Richards and Reddy, 2007). Under certain conditions, seepage can liquefy the sediment-water mixture and cause sliding of the embankment

mass or allow large volumes of material to be transported quickly as slurry. The weak layers and crakes can be caused by differential settlement, earthquakes, foundation defects, etc. Excessive seepage through permeable substrata is often accompanied by the formation of sand boils, which often look like miniature volcanoes ejecting water and sediment and may result in piping failure if not controlled.

Fig. 2.13. Teton Dam failed on June 5, 1976. The failure released nearly 300,000 acre feet of water, then flooded farmland and towns downstream with the eventual loss of 14 lives and with a cost estimated to be nearly $1 billion. Photo by Mrs. Eunice Olson.

Fig. 2.14. Dam breaching due to piping: (a) initiation; (b) t=5 min; (c) 8 min; (d) 13 min; (e) 13 min, following collapse of piping roof; (f) 60 min, continued widening (Experiment by Hanson et al., 2010)

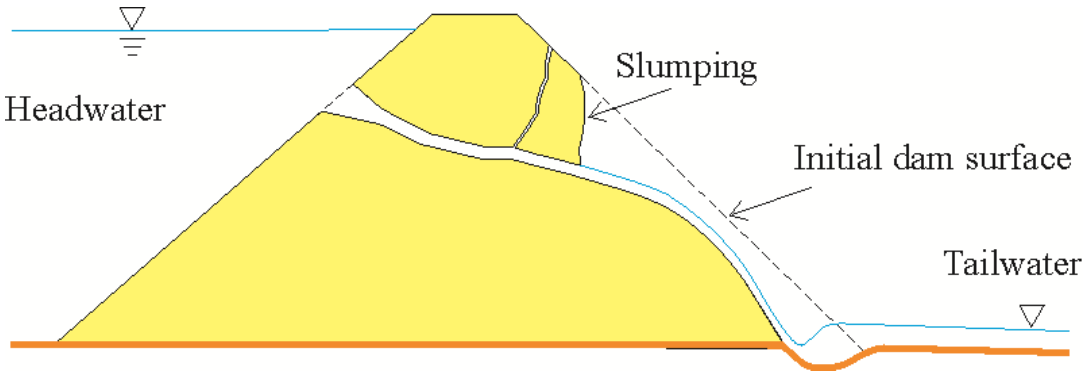

Fig. 2.15. Sketch of Dam Breaching due to Piping Observed in Experiments

DLBreach approximates the piping breach as a horizontal pipe with a rectangular cross-section, shown in Fig. 2.16. The flow can be one-way or two-way. The pipe is uniformly enlarged along its length due to hydraulic shear on the pipe surface. The pipe roof may lose its

stability as the pipe increases in dimension. Once the pipe roof fails and vanishes, open channel flow similar to the overtopping flow takes places. One can say that piping is an initial stage, followed by breach development by overtopping flow.

The reason to use a rectangular cross-section is the convenience of transition between the piping and the follow-up overtopping, as well as handling one-sided breach and roof stability analysis.

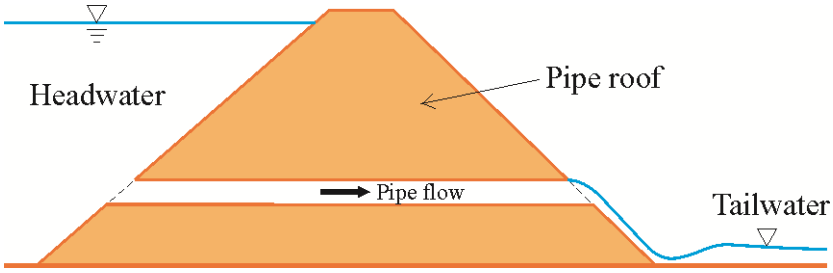

Fig. 2.16. Dam Breaching due to Piping Approximated in DLBreach

2.3. Embankment Breach Cross-Section

The embankment breach cross-section may be an approximate trapezoid, rectangle, triangle or parabola, depending on embankment geometry, soil properties, water conditions, failure mode, and so on (ASCE/EWRI 2011). Most historic dam failure events suggest a trapezoidal breach shape (Figs. 2.5 and 2.14). However, many dam breaching experiments and field levee, dike and barrier breaches demonstrate a breach shape with vertical, near-vertical or undercut sides in both cohesive and non-cohesive soils. The possible explanation is that prototype dams are usually higher than laboratory model dams and field levees, dikes and barriers. The stability of a side slope depends on the relative strength of the resistance forces, such as soil cohesion and suction, against the driving forces, such as gravity. Soil cohesion and suction tend to allow for vertical breach sides in lower embankments, whereas gravity tends to cause collapse of side walls in high embankments. In addition, chemicals (such as salinity) and organic materials in water and soil may also affect the breach shape since they modify the geotechnical properties.

The bottom of a fully formed dam breach is usually the foundation, which is more resistant to erosion than the embankment materials. However, base erosion often occurs in the breaching of levees, dikes and barriers whose foundations may be erodible. The maximum breach depth may be limited by the volume of headwater at the time of failure, by tailwater rise, or by the presence of a layer of erosion-resistant material located in the embankment.

DLBreach approximates the breach cross-section by overtopping as a trapezoid, shown in Fig. 2.17. The breach slope is determined by using the slope stability analysis. The side slope can be vertical (equivalent to a rectangular cross-section), for soils with strong cohesion; or the

bottom width can be zero, corresponding to triangular cross-section. Thus the trapezoid approximation is more general than the triangular and rectangular breach. The breach depth or the bottom height can be predefined by the user according to the embankment foundation characteristics. This allows the model to handle subbase erosion and improve the model prediction.

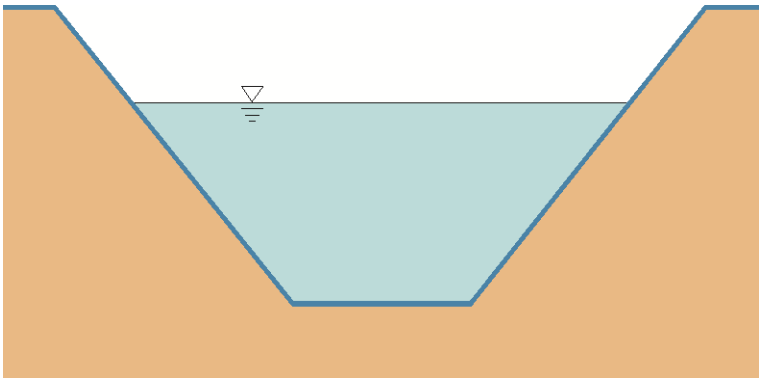

Fig. 2.17. Sketch of Trapezoidal Breach Cross-Section Approximated in DLBreach

2.4. Dam Breach versus Levee Breach

Earthen dam and levee breaches exhibit differences. One of the most significant differences is the effect of the upstream and downstream water conditions. In a dam breaching event, the upstream reservoir water level drops and the breach outflow discharge increases to a peak as the breach enlarges; subsequently the discharge decreases as water level decreases and storage volume in the reservoir is depleted. The dam breach size and outflow are thus usually limited by reservoir characteristics rather than downstream tailwater conditions. However, in a levee or dike failure along a large lake, the water level either does not drop or drops minimally. The breach size and outflow continue to increase until the tailwater downstream of the breach rises to reduce and eventually stop the flow through the breach. This downstream tailwater rise is likely to be the limiting condition. Tailwater rise has a similar effect on a riverine levee breach, but upstream river inflow also affects the breach size and outflow by sustaining the water level in the river. In addition, in the case of a riverine levee breach, the flow is parallel to the embankment, whereas in a dam breach, the flow is more or less perpendicular to. A difference between dam and river levee breaching would then be expected due to the direction of the momentum flux.

DLBreach handles dam and levee breaches using the same erosion and breach evolution model with different headwater and tailwater conditions. In the dam breach case, the upstream reservoir is modeled with the water balance equation. In the levee breach case, the upstream water level is prescribed with a time series of water level. In both dam and levee breaches, and

the downstream channel is assumed to have uniform flow or the downstream can be a water storage (such as lake, bay, and lowland basin) modeled with the water balance equation.

Because DLBreach is a simplified 1-D model, it does not consider the difference in the direction of momentum flux in the front of dam and levee breaches. How important is this difference is a problem yet to be investigated. In the time being, this difference is ignored in the model.

Chapter 3. Hydrodynamic Routing

3.1. Overtopping Flow through the Breach

3.1.1. Overtopping Discharge of Breach Flow

The breach flow in the early stage of breaching is usually supercritical or transcritical (Fig. 3.1(a)), and the breach formation period is often short. For a dam breach, breaching stops once the upstream reservoir water is depleted. However, for a levee or barrier breach in riverine or coastal context, the breach may continue to evolve due to continuous river flow or tidal flow after the intensive breaching period, even though the flow through the breach becomes subcritical (Fig. 3.1(b)). Therefore, DLBreach divides the breaching process into two periods: intensive breaching period and general evolution period. The model uses different equations to calculate the flow discharge through the breach in the two periods. The breach flow is estimated using the weir flow equation and the Keulegan equation for the first and second periods, respectively.

The broad-crested weir equation reads:

$$Q = k_{sm}\left(c_1 b H^{1.5} + c_2 m H^{2.5}\right) \tag{3.1}$$

where $H = z_s - z_b$, z_s = headwater level, z_b = elevation of breach bottom shown in Fig. 3.1, b = bottom width of the breach shown in Fig. 3.2, m = side slope (horizontal/vertical) of the breach, c_1 = 1.7, c_2 = 1.3 (Singh 1996), and k_{sm} = submergence correction for tailwater effects on weir outflow. k_{sm} is determined using the following empirical relation (see Fread 1984; Singh 1996):

$$k_{sm} = \begin{cases} 1.0 & \dfrac{z_t - z_b}{z_s - z_b} < 0.67 \\ 1.0 - 27.8\left(\dfrac{z_t - z_b}{z_s - z_b} - 0.67\right)^3 & \text{otherwise} \end{cases} \tag{3.2}$$

where z_t = tailwater level.

The Keulegan equation is the simplified energy equation for steady nonuniform flow with local head loss due to channel contraction and expansion. Even though the flow through a breach or coastal inlet is unsteady, the flow inertia effects are ignored, and thus the 1-D energy equation through the breach is written as

$$z_s - z_t = \left(\frac{2gn^2 L}{R^{4/3}} + \lambda_{en} + \lambda_{ex}\right)\frac{Q|Q|}{2gA^2} - LB\frac{\rho_a C_d U_{win}^2 \cos\theta_{win}}{\rho g A} \tag{3.3}$$

where L is the length of the breach or inlet in the breach flow direction, Q is the flow through the breach, A is the flow area in the breach, R is the hydraulic radius, B is the breach width at water surface, n is the

Manning's roughness coefficient, g is the gravitational acceleration, λ_{en} and λ_{ex} are the local head loss at the breach entrance and exit, respectively, ρ is the water density, ρ_a is the air density, C_d is the drag coefficient of wind, U_{win} the wind speed, and θ_{win} is the angle of wind with respect to the breach axis pointing from the headwater side to tailwater side.

Eq. (3.3) is the Keulegan equation revised by adding the wind driving force to consider the effect of wind.

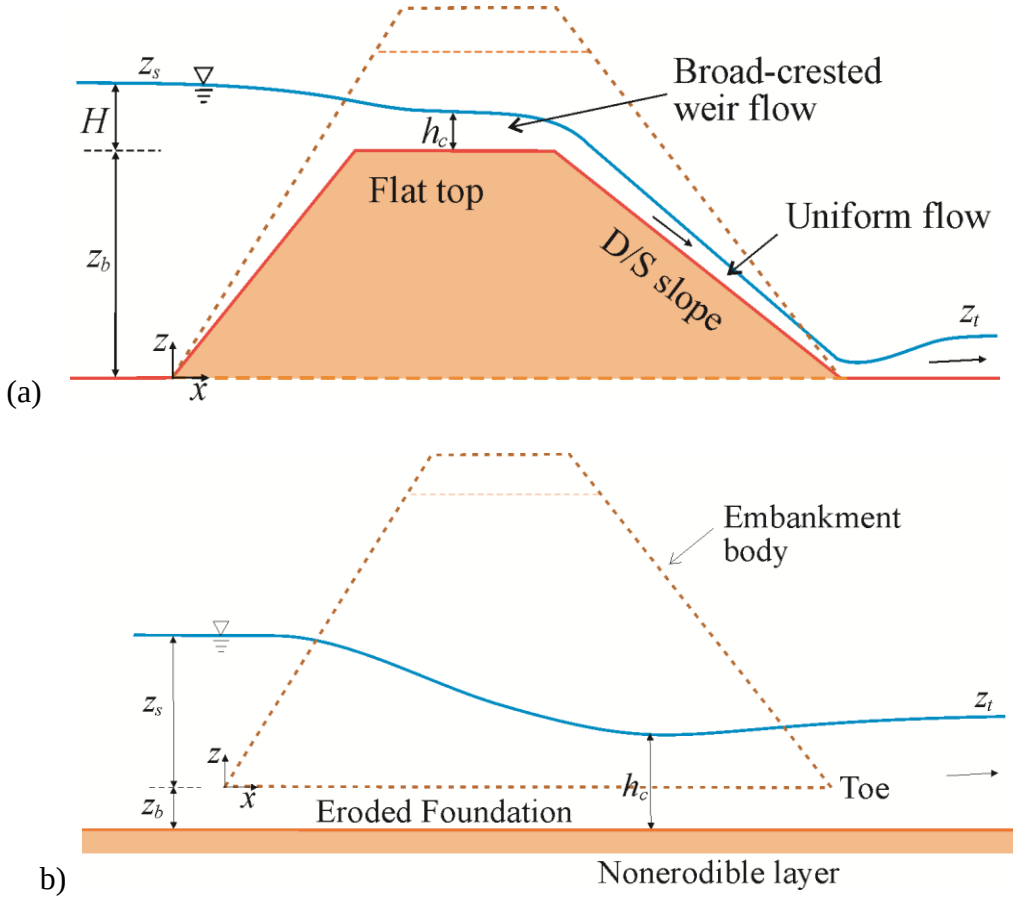

Fig. 3.1. Longitudinal Section of Breach with Variable Definitions:
(a) Intensive Formation Period; (b) General Evolution Period
(z_s = headwater level; H = headwater level above the breach bottom; z_b = breach bottom elevation; h_c = flow depth at the breach flat top; z_t = tailwater level)

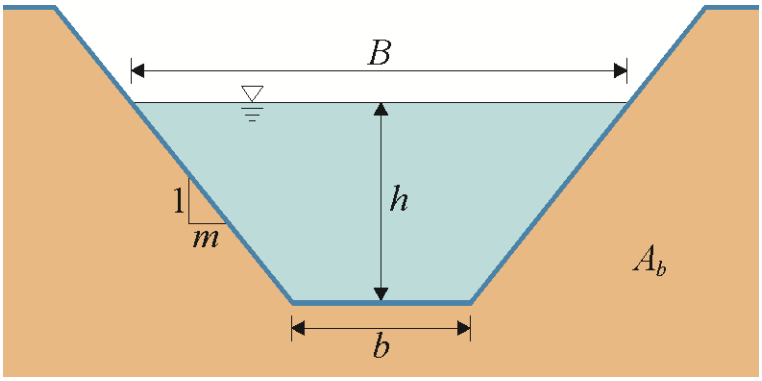

Fig. 3.2. Breach Cross-Section with Variable Definitions
(m = side slope: horizontal/vertical; B = water surface width; b = bottom with; h = flow depth; A_b = cross-sectional area of breach bed above a reference datum)

In the intensive breaching period, the breach flat top is treated as a broad-crested weir, on which critical flow can be used to represent the flow condition responsible for breach erosion. In the second period, the flow may be subcritical, so that the critical flow assumption is not valid. Therefore, the following equation is used to determine the representative flow depth at the breach, h_c, for both periods:

$$h_c = \max\left[\frac{2}{3}(z_s - z_b),\ \left(\frac{z_s + z_t}{2} - z_b\right)\right] \tag{3.4}$$

where the first term in the brackets is the critical flow depth at the broad-crested weir, and the second term is the average of the headwater and tailwater levels above the breach bottom. When the tailwater is low, the first term is larger than the second term and thus Eq. (3.4) specifies the critical flow depth at the breach, which is corresponding to the first period of breaching. When the tailwater rises to a certain extent, the second term becomes larger. This is corresponding to the second period of breaching.

Note that Eq. (3.4) requires $z_t > z_b$. If $z_t < z_b$, z_t is replaced by z_b in Eq. (3.4). For general application in case of two-way breach, Eq. (3.4) is implemented as follows:

$$h_c = \max\left\{\frac{2}{3}\max(z_s - z_b,\ z_t - z_b), \frac{1}{2}\left[\max(z_s - z_b,\ 0) + \max(z_t - z_b,\ 0)\right]\right\} \tag{3.5}$$

The intensive breaching period is specified using three options in DLBreach. The first option sets the intensive breaching period equal to the simulation period. This means no general evolution period is considered. This is the default option, often used for dam breach, or levee breach with short evolution period.

The second option sets the intensive breaching period as the time when the following conditions have met: (1) breach erosion reaches the embankment base (i.e. broad-crested weir

disappear); (2) both the upstream and downstream water levels are higher than the breach bottom elevation; and (3) the difference between the upstream and downstream water levels is less than 30% of the upstream super-elevation above the breach bottom. The three conditions read:

$$z_b \le 0,\ \min\left(z_s, z_t\right) > z_b,\ \text{and}\ \left|z_s - z_t\right| < 0.3\left[\max\left(z_s, z_t\right) - z_b\right] \tag{3.6}$$

The second option can be used in the case of levee and barrier breach. The third option allows the user to specify the intensive breaching period according to the specific conditions of the study case.

3.1.2. Overtopping Discharge by Waves

In the case of coastal levee and barrier breach, the effect of overtopping is important and needs to be considered. DLBreach uses a simple phase-averaged model to determine the net wave overtopping discharge.

When the surge level is lower than the breach bottom elevation, the average discharge due to wave overtopping is calculated by using the formula of van der Meer and Janssen (1995):

$$\frac{q_w}{\sqrt{gH_s^3}} = \begin{cases} 0.06\dfrac{\xi_{op}}{\sqrt{\tan\alpha}}\exp\left(-5.2\dfrac{R_c}{H_s}\dfrac{1}{\xi_{op}}\dfrac{1}{\gamma_r\gamma_b\gamma_h\gamma_\beta}\right) & \xi_{op} < 2 \\ 0.2\exp\left(-2.6\dfrac{R_c}{H_s}\dfrac{1}{\xi_{op}}\dfrac{1}{\gamma_r\gamma_b\gamma_h\gamma_\beta}\right) & \xi_{op} > 2 \end{cases} \tag{3.7}$$

where q_w is the average wave-only overtopping discharge per unit structure length, H_s is the significant wave height, tanα is the seaward structure slope, and R_c is the freeboard (vertical distance between the still water elevation and crest. For wave-only overtopping, R_c >0. The Iribarren number, ξ_{op}, is defined based on deepwater wave length and peak wave period as $\xi_{op} = \tan\alpha \Big/ \sqrt{H_s / L_{op}}$ with $L_{op} = gT_p^2 / (2\pi)$ and T_p = the peak wave period. The γ-factors are reduction factors related to surface roughness, seaward berms, shallow water, and oblique wave approach. The γ-factors are not considered in the present model.

When the surge level is higher than the breach bottom elevation, the overtopping discharge is a combined effect of surge and waves. Hughes and Nadal (2009) developed a formula to calculate the combined discharge due to surge overflow and wave overtopping:

$$q_{ws} = 0.0336\sqrt{gH_{m0}^3} + 0.973 q_s \left(\frac{-R_c}{H_{m0}}\right)^{0.083} \quad \text{for } R_c<0 \tag{3.8}$$

where q_s is the surge overflow discharge per unit breach (structure) width. The last term on the right-hand side of Eq. (3.8) is approximately equal to the surge overflow discharge q_s. Since q_s is calculated already using Eqs. (3.1) and (3.3), only the wave overtopping discharge is needed.

Thus, as an approximation, when the surge and wave overtopping coexist, the wave overtopping discharge is calculated by using the first term on the right-hand side of Eq. (3.8) as follows:

$$q_w = 0.0336\sqrt{gH_{m0}^3} \quad \text{for } R_c<0 \tag{3.9}$$

In summary, DLBreach determines the wave overtopping discharge by using Eq. (3.7) when $R_c>0$, and Eq. (3.9) when $R_c<0$. The total overtopping discharge by surge overflow and overtopping is q_s+q_w.

3.1.3. Uniform Flow Equation on Downstream Slope

A uniform flow is assumed on the downstream slope reach in Fig. 3.1 for the homogeneous noncohesive breach and those in Fig. 2.12 for the composite dam breach. The Manning's equation is written as

$$Q = \frac{1}{n} AR^{2/3} S_0^{1/2} \tag{3.10}$$

where A = flow area, R = hydraulic radius, S_0 = downstream slope of the breach channel, and n = Manning's roughness coefficient. $A = h(b+mh)$, and $R = A/(b+2h\sqrt{1+m^2})$, with h being the flow depth on the downstream slope. Eq. (3.10) is solved iteratively to obtain h.

3.1.4. Bed Shear Stress

Once the flow depths at the breach top and on the downstream slope reach are determined, the bed shear stresses on these reaches are determined from the estimated flow depths and discharges by using Manning's equation:

$$\tau_b = \frac{\rho g n^2 Q^2}{A^2 R^{1/3}} \tag{3.11}$$

where τ_b = bed shear stress, and ρ = water density.

3.1.5. Manning's Roughness Coefficient

Different Manning's n values can be specified for the breach top and downstream slope reaches, if the soil properties on these sections are different.

The Manning's n is related to sediment median size d_{50} (in meter) by

$$n = \frac{d_{50}^{1/6}}{A_n} \tag{3.12}$$

where A_n is an empirical coefficient. A_n is about 20 on fixed stream beds and may reduce to about 10 due to bed forms on movable stream beds (Wu 2007). For a rapidly-varying dam breach flow, bed forms may not have enough time or distance to fully develop. However, unlike stream

bed sediments, the dam sediments that have not gone through abrasion may be highly irregular, and correspondingly A_n has smaller values.

Model testing shows that A_n = 16 for the laboratory cases and 12 for the field cases, considering differences in sediment transport and bed forms between laboratory and field settings. For many earthfill dams or the cohesive portion of composite dams, the sediment representative sizes are estimated as 0.03 mm because cohesive soil moves in aggregates or flocs. The corresponding Manning's n is less than 0.016 according to Eq. (3.6), but the lowest value of 0.016 is specified.

3.2. Piping Flow through the Breach

In the case of piping, the model assumes the breach flow through a pipe with a rectangular cross-section at the initial stage, show in Fig. 3.3. If the pipe is partially filled with water, the breach flow in the pipe is treated as open-channel flow and determined using Eq. (3.1). If the pipe is fully filled with water, the flow through the pipe is determined using the orifice flow equation, which is derived by applying the energy equation:

$$Q = A\sqrt{\frac{2g\left(z_s - \max(z_{bp}, z_t)\right)}{K_u + K_d + fL/(4R_h)}} \tag{3.13}$$

where A = cross-section area of the pipe, z_{bp} = elevation of pipe center line, z_t = tailwater level, K_u = local head loss coefficient due to contraction at the pipe entrance, K_d = local head loss or kinetic energy coefficient at the pipe outlet, L = pipe length, R_h = hydraulic radius of the pipe cross-section, and f = Darcy-Weisbach friction factor of the pipe surface. $R_h = ab/\left[2(a+b)\right]$, with b = breach width and a = breach height (Fig. 3.3).

The entrance head loss coefficient K_u is set as about 0.05. If the pipe outlet is submerged by the tailwater, the flow kinetic energy will be dissipated by the enlarged cross-section of downstream water body; if the pipe outlet is exposed to air, the flow will exit the pipe with the same velocity as in the pipe. In both cases K_d can be assumed to be about 1.

The Darcy-Weisbach friction factor f is determined using Swamee and Jain's (1976) formula that approximates the Moody diagram:

$$f = \frac{0.25}{\left[\log_{10}\left(\frac{k_s}{3.7D_h} + \frac{5.74}{\mathrm{Re}^{0.9}}\right)\right]^2} \tag{3.14}$$

where k_s is the equivalent roughness height on the pipe surface, set as d_{50}; D_h=4R_h; and Re=UD_h/v. U is the average velocity in the pipe.

An alternative approach is to relate f with the Manning's n as follows:

$$f = \frac{8gn^2}{R_h^{1/3}} \tag{3.15}$$

Once the flow in the pipe is determined, the average shear stress on the pipe surface is determined using Eq. (3.11) with R replaced by R_h.

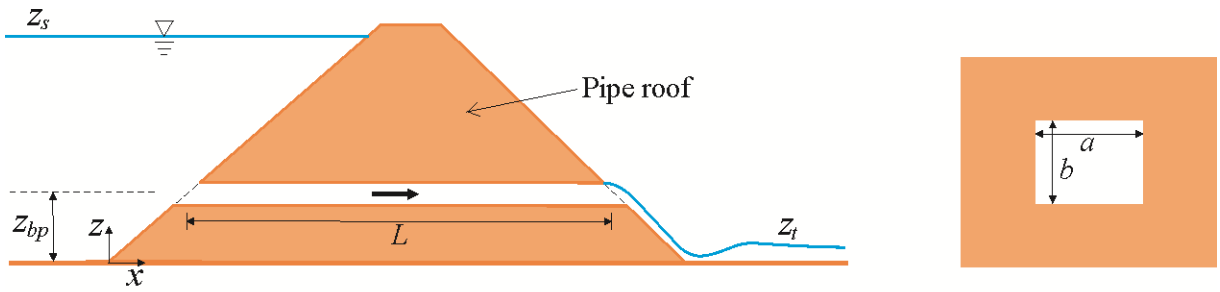

Fig. 3.3. Piping Breach with Variable Definitions: (a) Longitudinal Section; (b) Cross-Section of the Pipe (z_{bp} = elevation of pipe centerline referring to the dam bottom; L = Pipe length; a = pipe width; b = pipe height; z_s = headwater level; z_t = tailwater level)

3.3. Upstream Flow Routing

3.3.1. Headwater Level

In the case of levee breaching, time series of headwater surface elevation needs to be given using either measured data, or calculated with another hydrodynamic model for upstream river flow. The time series of water level is represented by pair values of elapsed time t and water level z_s:

t_1, $z_{s,1}$

t_2, $z_{s,2}$

…

t_{i-1}, $z_{s,i-1}$

t_i, $z_{s,i}$

…

t_{N-1}, $z_{s,N-1}$

t_N, $z_{s,N}$

The water level at a given elapsed time is calculated from the above pair values of time and water level by using piecewise linear interpolation.

3.3.2. Reservoir Routing

In the case of dam breaching, the water volume in the reservoir changes due to inflows from upstream basin and outflows from the breach, spillway, sluice gate, etc. as shown in Fig. 3.4. The water balance in the reservoir can be described by

$$\frac{dV}{dt} = A_s \frac{dz_s}{dt} = Q_{in} - Q - Q_{on-site\ spill/sluice} - Q_{off-site\ spill/sluice} \tag{3.16}$$

where t = time, V = volume of water in the reservoir, A_s = surface area of reservoir, z_s = water surface elevation, Q_{in} = inflow discharge, Q = breach flow, and $Q_{spill/sluice}$ = flow through spillways and sluice gates.

The spillways and sluice gates include those built on the embankment (on-site) and auxiliary ones not built on the embankment (off-site). In DLBreach, only on-site spillways and sluice gates contribute flows to the downstream channel or storage basin. The flows from the off-site spillways and sluice gates will not be included in the downstream flow routing.

Eq. (3.16) is discretized using the following semi-implicit difference scheme:

$$\frac{V^{n+1} - V^n}{\Delta t} = A_s^{n+1/2} \frac{z_s^{n+1} - z_s^n}{\Delta t} = Q_{in}^{n+1/2} - Q^{n+1/2} - Q_{on-site\ spill/sluice}^{n+1/2} - Q_{off-site\ spill/sluice}^{n+1/2} \tag{3.17}$$

where Δt is the time step length, and n is the counter of time level. n+1/2 denotes the middle between time levels n and n+1.

Because it is semi-implicit, Eq. (3.17) needs to be solved iteratively, coupled with the weir flow equation (3.1), (3.3) or the orifice flow equation (3.13) and the equations for upstream and downstream flows.

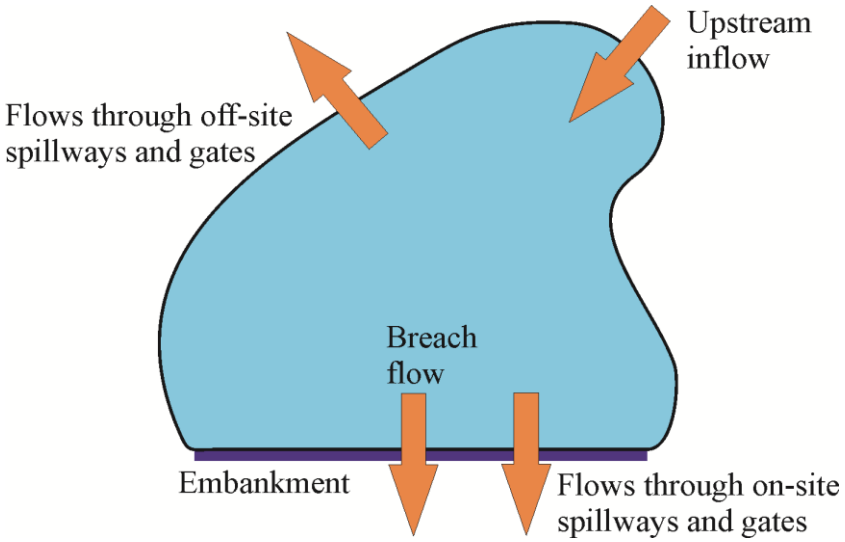

Fig. 3.4. Water Balance in the Reservoir

3.3.3 Reservoir Geometric Characteristics

The reservoir geometric characteristics are represented by the surface area and water level curve, $A_s(z)$, or the storage volume and water level curve, $V(z)$. The water level z is defined above

the embankment toe elevation. The $A_s(z)$ curve is usually given as pair values of water level and surface area of the reservoir:

z_1, $A_{s,1}$
z_2, $A_{s,2}$
…
z_{i-1}, $A_{s,i-1}$
z_i, $A_{s,i}$
z_{i+1}, $A_{s,i+1}$
…
z_{N-1}, $A_{s,N-1}$
z_N, $A_{s,N}$

The $V(z)$ curve is also usually given as pair values of water level and storage volume of the reservoir:

z_1, V_1
z_2, V_2
…
z_{i-1}, V_{i-1}
z_i, V_i
z_{i+1}, V_{i+1}
…
z_{N-1}, V_{N-1}
z_N, V_N

Piecewise linear interpolation is used to calculate the surface area or storage volume with a given water level from the above pair values of surface area and level.

Note that the reservoir volume and water level curve is known can be converted to the surface area and water level curve, or vice versa. The conversion uses the relation between reservoir volume and surface area expressed in the first equation in Eq. (3.16). It is rewritten and discretized as

$$A_s = \frac{dV}{dz} = \frac{V_i - V_{i-1}}{z_i - z_{i-1}} \tag{3.18}$$

For the pair values of volume-level curve given above, the converted pair values of surface area-level curve are:

$(z_1+z_2)/2$, $(V_2-V_1)/(z_2-z_1)$
…
$(z_{i-1}+z_i)/2$, $(V_i-V_{i-1})/(z_i-z_{i-1})$
$(z_i+z_{i+1})/2$, $(V_{i+1}-V_i)/(z_{i+1}-z_i)$

…

$(z_{N-1}+z_N)/2$, $(V_N-V_{N-1})/(z_N-z_{N-1})$

In many field cases, the reservoir surface area - water level curve is not available, and only the reservoir storage capacity (or available water volume above the breach at failure) and/or surface area at certain level (such as normal pool level or water height before the failure) are known. The surface area is thus assumed to be a power function of water depth:

$$A_s = \alpha_r z^{m_r} \tag{3.19}$$

where α_r and m_r are coefficients. Integration of Eq. (3.19) from the bottom to the water level z leads to the volume and level relation:

$$V = \int_0^z A_s dz = \frac{\alpha_r}{m_r + 1} z^{m_r+1} \tag{3.20}$$

If both the reservoir storage, V_N, and surface area, A_{sN}, at the normal pool level (or the water level before the failure), z_N, are known, one can derive the following relation of exponent m_r by substituting these two conditions into Eqs. (3.19) and (3.20):

$$m_r = \frac{A_{sN} z_N}{V_N} - 1 \tag{3.21}$$

Table 3.1 shows reservoirs with known storage capacity and surface area at a reference water level, for which the exponent m_r has values between 1.0–3.1 and an average value of 2.0. This implies that if only the reservoir storage or surface area is known, m_r can be approximately assumed to be 2.0. Once the coefficient m_r is determined or assumed, the coefficient α_r can be derived by using Eq. (3.19) or (3.20).

Table 3.1. Exponent m_r for Eq. (3.19) in Reservoirs with Known Surface Area and Volume

Case Name	z_N	V_N	A_{sN}	m_r
Apishapa	34.14	2.25×10^7	2.59×10^6	2.93
Baldwin Hills	47.2	1.1×10^6	7.689×10^4	2.30
Castlewood	21.34	4.23×10^6	8.094×10^5	3.08
Horse Creek	12.19	2.1×10^7	4.856×10^6	1.82
Kelly Barnes	11.58	7.77×10^5	1.7×10^5	1.53
Lake Frances	15.24	8.65×10^5	1.74×10^5	2.07
Poerua Landslide	80	$(5\text{-}7)\times10^6$	2×10^5	1.67
Sheep Creek	17.07	2.91×10^6	3.44×10^5	1.02
Spring Lake	5.49	1.35×10^5	7.284×10^4	1.96
Average				2.04

3.4. Downstream Flow Routing

3.4.1. Uniform Channel Flow

If the downstream of the breach is connected with a channel, the tailwater level is calculated by assuming uniform flow there. The downstream channel is approximated as a rectangular channel, with a channel width, bed slope and Manning's *n* specified by the user. Eq. (3.10) is used to calculate the water depth at the downstream channel, and then the tailwater level of the breach.

3.4.2. Downstream Water Storage Routing

If the downstream is connected to a water storage body, such as bay, lake or lowland basin (Fig. 3.5), the tailwater level is determined by solving the following water balance equation in the downstream water body:

$$\frac{dV}{dt} = A_s \frac{dz_s}{dt} = Q_{in} + Q + Q_{on-site\ spill/sluice} - Q_{off-site\ spill/sluice} \tag{3.22}$$

where V = volume of water in the water body, A_s = surface area of the water body, z_s = water surface elevation, Q_{in} = inflow discharge from the watershed or from the connected water body, Q = breach flow, $Q_{on\text{-}site\ spill/sluice}$ = flow from spillways and sluice gates built on the embankment, and $Q_{off\text{-}site\ spill/sluice}$ = flows out through auxiliary spillways and sluice gates that are not built on the embankment.

Similar to reservoir, the water surface area and depth curve is needed for the water storage body. Currently, DLBreach allows for the user to provide the pair values of water level and surface area or volume for the downstream water body, or use Eq. (3.19) to determine the curve with known basin surface area and/or volume at a pool level.

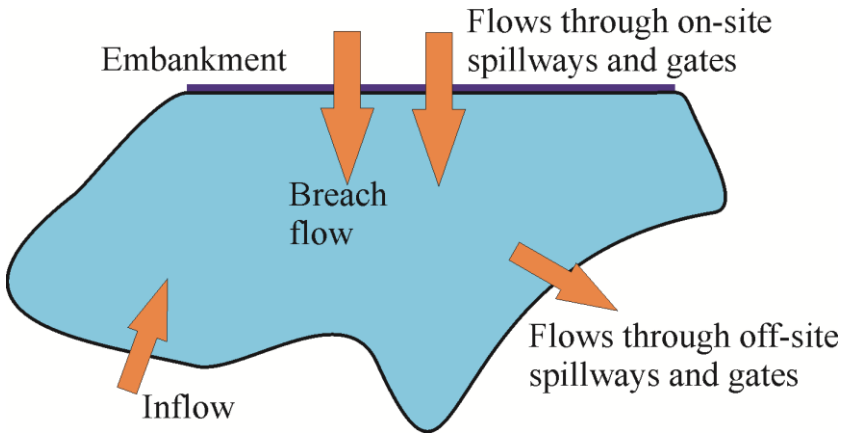

Fig. 3.5. Water Balance in the Downstream Storage Body

3.4.3. Tailwater Level

Time series of tailwater surface elevation is given using either measured data, or calculated with another hydrodynamic model for downstream water body. The time series of water level is represented by pair values of elapsed time t and water level z_s, like those for headwater.

3.5. Other Flow Calculations

3.5.1. Inflow to Reservoir and Storage Basin

Time series of inflow discharge to the reservoir or storage basin needs to be given using either measured data, or calculated with an upstream river flow model or a watershed model. The time series of water level is represented by pair values of elapsed time t and discharge Q_{in}:

t_1, $Q_{in,1}$
t_2, $Q_{in,2}$
…
$t_{i\text{-}1}$, $Q_{in,i\text{-}1}$
t_i, $Q_{in,i}$
…
$t_{N\text{-}1}$, $Q_{in,N\text{-}1}$
t_N, $Q_{in,N}$

3.5.2. Flows through Spillways and Sluice Gates

The flow through a spillway is calculated as

$$Q_{spill} = \alpha_{sm} C_{spill} B_{spill} \left(z_s - z_{b,spill} \right)^{1.5} \tag{3.23}$$

where Q_{spill} is the discharge through the spillway, α_{sm} is the downstream submergence coefficient, C_{spill} is the discharge coefficient, B_{spill} is the spillway flow width, z_s is the water level in the reservoir or basin, and $z_{b,spill}$ is the elevation of the spillway crest.

The flow through a sluice gate is calculated as

$$Q_{sluice} = C_{sluice} A_{sluic} \left[z_{s,up} - \max(z_{b,sluice}, z_{s,down}) \right]^{0.5} \tag{3.24}$$

where Q_{sluice} is the discharge through the sluice gate, C_{sluice} is discharge coefficient, A_{sluice} is the cross-sectional area of sluice gate opening, $z_{s,up}$ and $z_{s,down}$ are the water levels in the upstream and downstream, and $z_{b,sluice}$ is the elevation of the sluice gate bottom.

3.5.3. Flow over Other Portions of the Embankment Crest

When the headwater level is higher than the embankment crest elevation, overtopping flow occurs on the other portions of the crest excluding the breach. This flow is calculated using the weir equation:

$$Q_{sc} = c_1 w\left(z_s - z_D\right)^{1.5} \tag{3.25}$$

where Q_{sc} is the flow discharge overtopping the other portions of the embankment crest, z_s is the headwater level, z_D is the elevation of embankment crest, and w is the width of the crest portions excluding the breach. The coefficient c_1 is assumed to be the same as that in Eq. (3.1).

Q_{sc} is added to the flow through on-site spillways and sluice gates in the model result output.

3.5.4. Wave Setup

Wave setup is the increase of water level within the surf zone due to the transfer of wave-related momentum to the water column during wave breaking (Dean and Walton, 2010). There are many empirical formulas to estimate the wave setup. In the present model, the wave setup on the seaside shore, $\bar{\eta}$, is roughly estimated as

$$\bar{\eta} = \alpha_w H_s \tag{3.26}$$

where H_s is the significant wave height, and α_w is an empirical coefficient.

In a North Sea field wave setup experiment, Hansen (1978) found that for the average wave setup, α_w is about 0.3, whereas for the maximum wave setup this coefficient can be about 0.5. Through a field experiment study, Guza and Thornton (1981) suggested α_w ranges approximately from 0.05 to 0.5, and has an average of 0.17. Holman and Sallenger (1985) conducted a field experiment at USACE's field research pier in Duck, NC, and found α_w in their data has higher values. A detailed review on this can be found in Dean and Walton (2010).

3.5.5. Wind Setup

Wind blowing the water surface of lakes, reservoirs, bays and seas generates not only surface waves, but also the surface tilt from the windward side to the downwind side of the basin. Wind induces a current in the upper layers of the water body in the direction of the wind and causes the water to pile up at the downwind shore, while a return current is established along the bottom layers of the water in the opposite direction of the wind. Therefore, the water level is depressed at the upwind side of the basin and raised at the downside side. The rise in water level at the downwind side of the water body is called wind setup. The wind setup can be predicted using sophisticated 2-D and 3-D numerical models. In the present simplified model, the wind setup is predicted using the following relation (see McCartney, 1976)

$$S = \frac{U_{win}^2 F_{win}}{1440 D} \tag{3.27}$$

where S is the wind setup in feet, U_{win} is the wind speed in miles per hour, F_{win} the wind setup fetch in miles, and D is the average depth over the wind setup fetch in feet.

Eq. (3.27) provides generally conservative wind setup estimate at all locations in a relatively deep water body except at those locations where the basin geometry converges to the shore site of interest. For sites located in a highly convergent zone it may be justified to increase the wind setup as much as 50% to account for an additional pileup of water (Bodine and Hebler, 1978).

Eq. (3.27) is implemented in the present model by considering wind direction and converting to the SI system (U_{win} in m/s, F_{win} in meter and D in meter) as follows:

$$S = 2\times10^{-7}\frac{U_{win}^2\lambda_w F_{win}}{D}\cos\theta_{win} \tag{3.28}$$

where λ_w is a correction factor to consider the geometry convergence for the site of study, and θ_{win} is the angle of wind with respect to the breach axis pointing from the bay to the seaside. The correction factor λ_w is about 1.0-1.5. It is combined with the fetch F_{win} as the effective fetch $F_{win,e}$:

$$F_{win,e} = \lambda_w F_{win} \tag{3.29}$$

The model requires the user provides $F_{win,e}$ on both the bay and sea sides. If wind blows from the bay to the sea, the wind setup is positive and raises the water level on the bay side, whereas the wind setup is negative and reduces the water level on the sea side.

Chapter 4. Sediment Transport and Breach Evolution

4.1. Non-cohesive Sediment Transport

4.4.1 Non-equilibrium Transport Equation of Total Load

Sediment transport in open channel has a tendency to adjust from a non-equilibrium state to the state of equilibrium in which sediment concentration is equal to the flow carrying-sediment capacity. However, this adjustment is not instantaneous and needs a certain distance or time to complete. Embankment breaching is a typical erosion process, with upstream condition of clear water or little sediment concentration. The breach channel is so short that sediment transport usually does not reach the equilibrium state at the end of the breach. Non-cohesive sediment transport in the breach should be described using a non-equilibrium transport model.

Sediment moving with water is often classified as bed load and suspended load, which move near the bed and in the upper water column, respectively. In the case of embankment breaching, the flow is quite strong, so both bed load and suspended load exist. The following total-load (bed load + suspended load) non-equilibrium transport equation (Wu 2007) is used in DLBreach to describe the non-cohesive sediment transport in the breach:

$$\frac{\partial\left(AC_t\right)}{\partial t}+\frac{\partial\left(QC_t\right)}{\partial x}=-\frac{Q}{L_s}\left(C_t-C_{t*}\right) \tag{4.1}$$

where t = time, x = longitudinal coordinate, A = cross-sectional flow area in the breach channel, Q = flow discharge in the breach, C_t = actual total-load sediment concentration, C_{t*} = sediment transport capacity or concentration at the equilibrium state, and L_s = adaptation length characterizing the adjustment of sediment from a non-equilibrium state to the equilibrium state.

The sediment mass balance equation is written as

$$\frac{\partial\left(AC_t\right)}{\partial t}+\frac{\partial\left(QC_t\right)}{\partial x}+\left(1-p'\right)\frac{\partial A_b}{\partial t}=0 \tag{4.2}$$

where p' = porosity of embankment materials, and A_b = cross-sectional area of breach channel bed above a reference datum (shown in Fig. 3.2).

4.4.2. Solution of Sediment Transport

Because the breach is short and the breach flow is fast, the longitudinal variation of flow discharge at the breach is assumed negligible, i.e. a constant Q is applied along the breach at each time step. In addition, the temporal storage term (first term) in Eq. (4.1) is assumed small in comparison with the convection and near-bed exchange terms. As shown in Fig. 4.1, the breach of non-cohesive embankment is divided into three reaches: the upstream straight slope, the flat top and the downstream straight slope. The upstream slope does not have erosion. On each of the

flat top and downstream slope reaches, C_{t*} and L_s can be assumed as constant, so that Eq. (4.1) without the temporal storage term has the following analytical solution:

$$C_{t,out} = C_{t*} + \left(C_{t,in} - C_{t*}\right)\exp\left(-\frac{\Delta x}{L_s}\right) \tag{4.3}$$

where $C_{t,in}$ and $C_{t,out}$ = sediment concentrations at inflow and outflow cross-sections of each reach considered, and Δx = reach length.

Eq. (4.2) without the temporal storage term is discretized at each of the flat top and downstream slop reaches using the following finite difference scheme:

$$\left(1-p'\right)\frac{\Delta A_b}{\Delta t} = Q\frac{C_{t,in} - C_{t,out}}{\Delta x} \tag{4.4}$$

where Δt is the time step length. Define the bed volume change $\Delta V_b = \Delta A_b \Delta x$. Thus, the bed volume change in each reach is determined by

$$\Delta V_b = \frac{Q\left(C_{t,in} - C_{t,out}\right)\Delta t}{1-p'} \tag{4.5}$$

Using the clear water condition in the reservoir or a given sediment discharge from the headwater, application of Eq. (4.3) in the flat top reach results in the sediment concentration at the downstream edge of the flat top. Then, using the obtained sediment concentration as the inflow sediment concentration for the downstream slope, Eq. (4.3) with Δx replaced by Δs can give the sediment concentration at the outlet of the breach. Once the inflow and outflow sediment concentrations are known, the embankment volume change of each reach can be calculated using Eq. (4.5). The volume change will be allocated on the breach, as described in Section 4.3.

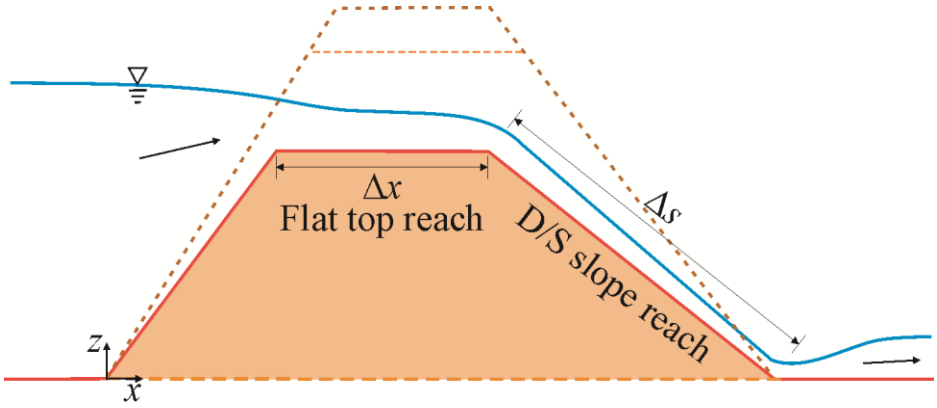

Fig. 4.1. Longitudinal Section of Breach for Sediment Calculations

4.4.3. Sediment Transport Capacity and Adaptation Length

Several formulas, including Meyer-Peter and Mueller (1948), Zhang (1961), Engelund and Hansen (1967) and Wu et al. (2000), have been implemented in DLBreach to determine the sediment transport capacity C_{t*}. After extensive testing, the combination of the suspended-load formula of Zhang (1961) and the bed-load formula of Wu et al. (2000) considering the effect of steep slope (see Wu 2007) is chosen to determine the total-load transport capacity C_{t*}.

Based on the energy balance of sediment-laden flow, Zhang (1961; also see Zhang and Xie, 1993) derived the relation between suspended-load transport capacity C_* and parameter $U^3/(gR\omega_s)$, as shown in Fig. 4.2, using measured data from the Yangtze River, the Yellow River, etc. Here, C_* is the suspended-load concentration at equilibrium, R is the hydraulic radius of the channel, and ω_s is the settling velocity of sediment. The reason to choose Zhang's (1961) formula is due to that the data used to drive the formula covers sediment concentrations up to ~100 kg/m^3, and the slope of the curve reduces as $U^3/(gR\omega_s)$ increases. It has the potential to handle the high sediment concentration in embankment breach flows. Guo (2002) approximated the $C_* - U^3/(gR\omega_s)$ curve in Fig. 4.2 by the following equation:

$$C_* = \frac{1}{20}\left(\frac{U^3}{gR\omega_s}\right)^{1.5} \Bigg/ \left[1+\left(\frac{1}{45}\frac{U^3}{gR\omega_s}\right)^{1.15}\right] \tag{4.6}$$

Wu et al. (2000) related the bed-load transport rate to the grain shear stress. The formula was calibrated by using extensive data sets from laboratory experiments and field measurements, as shown in Fig. 4.3. The formula for single-sized bed load is expressed as follows:

$$\frac{q_{b*}}{\sqrt{(\gamma_s/\gamma - 1)gd^3}} = 0.0053\left(\frac{\tau_b'}{\tau_c} - 1\right)^{2.2} \tag{4.7}$$

where q_{b*} = bed-load transport rate by volume per unit time and width (m^{2}s^{-1}), d = sediment size, $\tau_c = 0.03(\gamma_s - \gamma)d$, and τ_b' is the grain shear stress. $\tau_b' = (n'/n)^{3/2}\tau_b$ with $n' = d^{1/6}/20$, n = Manning roughness coefficient of channel bed, and τ_b = bed shear stress.

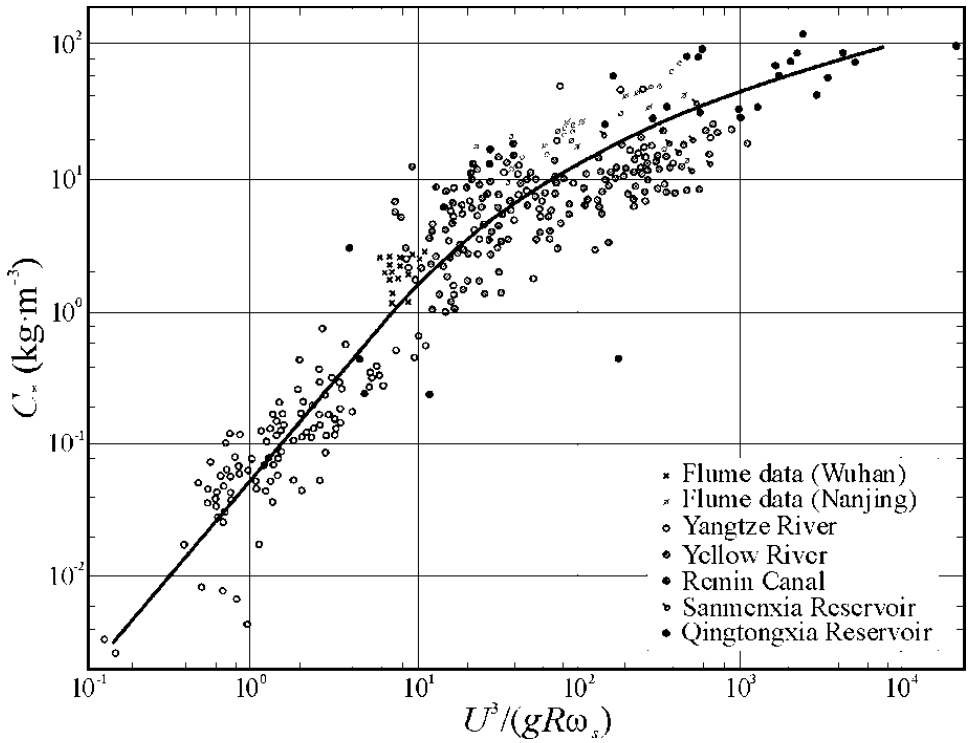

Fig. 4.2. Suspended-Load Transport Capacity (Zhang, 1961)

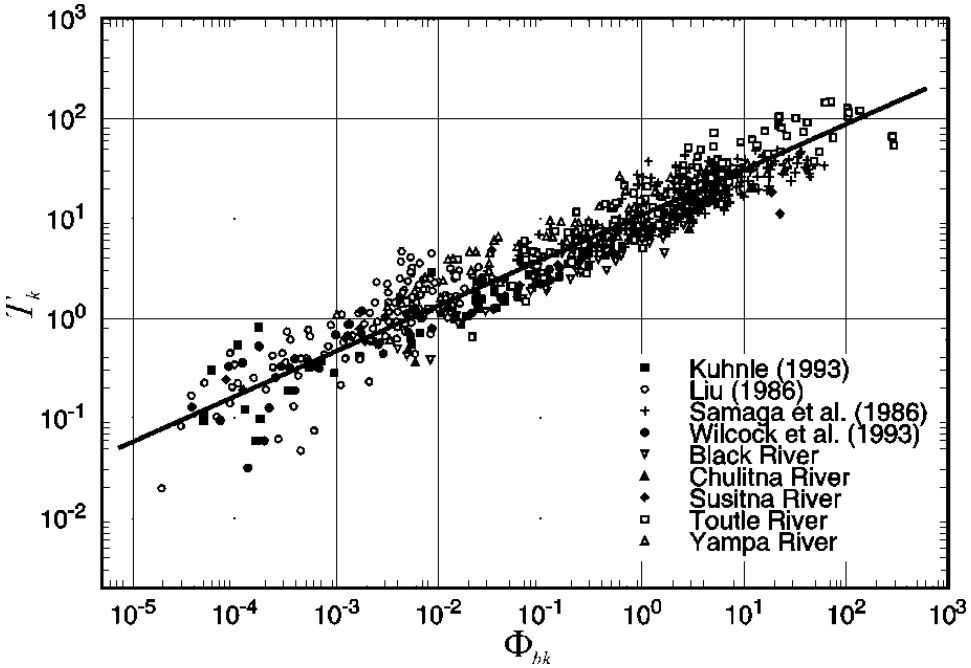

Fig. 4.3. Bed-Load Transport Capacity (Wu et al., 2000)

($\Phi_{bk} = q_{b*k} \Big/ \left[p_{bk} \sqrt{(\gamma_s/\gamma - 1) g d_k^3} \right]$, $T_k = \tau_b' / \tau_{ck} - 1$, p_{bk} = bed material gradation, and k = sediment size fraction counter)

Eq. (4.7) was compared with Meyer-Peter and Mueller (1948) formula and several other bed-load formulas, and found to be more reliable for a wide range of flow and sediment conditions (Wu 2007). Eq. (4.7) is extended to consider sediment transport over steep slope by replacing τ_b' with the effective shear stress τ_e as follows:

$$\tau_e = \tau_b' + \lambda_0 \tau_c \frac{\sin\phi}{\sin\varphi_r} \tag{4.8}$$

where ϕ = longitudinal slope angle of the channel bed, φ_r = repose angle of sediment, and λ_0 = correction factor as

$$\lambda_0 = \begin{cases} 1 & \phi \le 0 \\ 1 + 0.22\left(\tau_b'/\tau_c\right)^{0.15} e^{2\sin\phi/\sin\varphi_r} & \phi > 0 \end{cases} \tag{4.9}$$

The total-load transport capacity C_{t*} is calculated with

$$C_{t*} = C_* + \frac{q_{b*}}{Q} \tag{4.10}$$

The adaptation length L_s in Eq. (4.1) is related to flow, sediment transport, bed forms, and channel geometry, as discussed in detail in Wu (2007). It is related to the water surface width, B, as

$$L_s = \lambda B \tag{4.11}$$

where λ is an empirical coefficient, and is determined as 3 and 6 in small- and large-scale cases, respectively. For field applications of dam breach, λ is suggested to be 6 as default. For levee and barrier breach, λ is about 3.

4.2. Cohesive Sediment Erosion

4.2.1. Soil Erosion Equation

In the case of cohesive sediment, the bed erosion rate, $d\varepsilon/dt$, is determined using the following linear function of excess shear stress:

$$\frac{d\varepsilon}{dt} = k_d\left(\tau_b - \tau_c\right) \tag{4.12}$$

where τ_c = critical shear stress, and k_d = erosion coefficient.

Eq. (4.12) is applied to calculate the erosion thickness, $\Delta\varepsilon$, at the bed and side walls of the breach for a given time step Δt. According to Knight et al. (1984), for narrow rectangular channels (e.g. b/h=2), experiments showed that the average bed shear stress is approximately

equal to the average side-wall shear stress. This is approximately valid for narrow trapezoidal channels (Javid and Mohammadi 2012). As the ratio *b/h* increases, the ratio of wall to bed shear stress decreases (to about 0.65 for a trapezoidal channel with 45^o side slope). Considering the breach channel is usually narrow, the ratio of wall to bed shear stress is close to 1. On the other hand, the effect of side slope (gravity) on sediment erosion may increase the erosion rate on the side walls of the channel. Therefore, it can be assumed that the erosion thickness at the bed and the side walls are equal. With this assumption, the erosion area change at the breach cross-section can be obtained by multiplying the erosion thickness with the erodible wetted perimeter p_e, i.e., $\Delta A_b = p_e \Delta\varepsilon$. Note that p_e excludes the non-erodible side wall if exists. It also excludes the non-erodible bed when downcutting reaches to the non-erodible foundation.

DLBreach has two options to handle cohesive sediment erosion at the downstream slope of the breach. The first option is called "surface erosion", shown in Fig. 4.1, which is the same as the non-cohesive sediment case. In this option, the volume change at each reach of the breach is obtained by $\Delta V_b = A_e \Delta\varepsilon$. Here, A_e is the erodible surface area of the breach channel under water. The volume change will be allocated on the breach, as described in Section 4.3. The second option is called "headcut erosion", which will be described in Section 4.5.

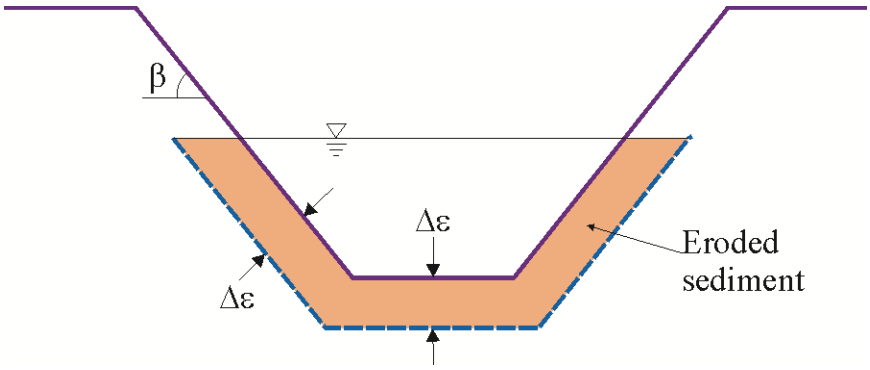

Fig. 4.4. Erosion at channel bed and side walls

4.2.2. Soil Erosion Rate Coefficient and Critical Shear Stress

Preferably τ_c and k_d are measured using the Jet Erosion Test (Hanson and Cook, 2004), SedFlume (McNeil et al., 1996)), Erosion Function Apparatus (Briaud et al., 2001), open channel flume in laboratory and other devices. When the measurements are not available, the following guidance can be used to estimate these two parameters.

The SITES program (USDA-NRCS 1997) suggested that the critical shear stress is calculated using the Shields diagram. Because cohesive sediment transports and erodes in flocs, Wu (2013) suggested the representative cohesive sediment size to be 0.03 mm to consider the floc size in DLBreach. Thus, the critical shear stress τ_c is about 0.15 Pa according to the Shields Diagram. This value is at the lower bound of the τ_c values of cohesive soils in practice.

The SITES program (USDA-NRCS 1997) suggested the following relation for k_d:

$$k_d = \frac{10\gamma}{\gamma_d}\exp\left[-0.121 c_{\%}^{0.406}\left(\frac{\gamma_d}{\gamma}\right)^{3.1}\right] \tag{4.13}$$

where k_d is in cm^3/N-s, $c_{\%}$ = clay percent in the soil, γ = specific weight of water, and γ_d = dry specific weight of the soil.

Wu (2013) found the k_d values given by Eq. (4.13) are too small. The reason may be that the flows are very strong during the breaching process, whereas Eq. (4.13) was developed under the common flow conditions in open channels or other measurement devices. Eq. (4.13) is usually for surface erosion mode (corresponding to low shear stresses), whereas the soil erosion by breach flows may have reached to mass erosion mode (corresponding to high shear stresses). In the model test section of this report, the values of k_d were calibrated in thirty five cases of field dam breach experiments and case studies using DLBreach, and found to be in the range of 2.5-30 cm^3/N-s.

Among the two parameters in Eq. (4.12), k_d usually is more important than τ_c. Except for the initial and final stages of the breaching process, τ_c is usually much smaller than τ_b, so that τ_c does not affect much the peak breach flow and final breach width (may affect the breach formation time somehow). k_d significantly affects the erosion rate and in turn the breach flow and geometry. It is preferable to measure k_d value for each specific case. If measurement data is not available, sensitivity study by using several different k_d values is recommended.

4.3. Allocation of Breach Morphology Changes

Sections 4.1 and 4.2 described how to calculate the volumetric bed change ΔV_b for each time step Δt for both non-cohesive and cohesive embankment breaches in the mode of surface erosion. The volume change needs to be converted to bed change and width change allocated along the breach cross-section. This allocation involves the sliding or failure of the side walls as described below.

4.3.1. Allocation of Breach Morphology Changes in the Flat Top Reach

The sediment on the side walls above the water surface will fall into the breach channel by particle sliding in the case of non-cohesive sediment and by mass failure in the case of cohesive sediment. Shown in Fig. 4.5, the sediment erosion occurs only in the water area, and the side walls experience undercutting by the flow. For non-cohesive sediment, the sediment particles hanged on the walls above the water surface slide down to the breach bottom. The breach channel side slopes are at the repose angle. This sliding process can be treated as a continuous process, and the actual erosion thickness is calculated at each time step as follows:

$$\Delta z_b = \frac{\Delta V_b}{A_{e,tot}} \tag{4.14}$$

where $A_{e,tot}$ is the total erodible surface area of the breach channel including both the portion below and above water. Since $A_{e,tot}$ is larger than A_e, the actual erosion thickness Δz_b is less than $\Delta\varepsilon$.

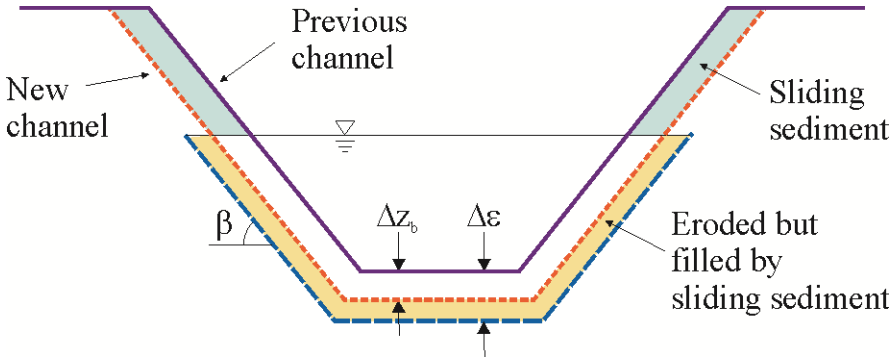

Fig. 4.5. Adjustment of Sediment Erosion Considering Mass Sliding or Failure

In the case of cohesive sediment, the mass failure is a discontinuous process. Occurrence of each mass failure event is determined by the slope stability which is affected by the soil properties, such as cohesion and internal friction. Section 4.4 introduces how to analyze the slope stability. However, exactly considering such discontinuous process needs to consider the disturbance of the failure block in the breach channel and the irregular cross-section geometry. For convenience and simplicity, DLBreach assumes the failure block to be gradually released to the channel bottom like non-cohesive sediment particle sliding, and thus keeps the side slope unchanged until the next mass event occurs. Therefore, Eq. (4.14) is also used to calculate the erosion thickness for cohesive sediment at the flat top, as well as at the downstream slope if the surface erosion mode is used.

$A_{e,tot}$ consists of the breach bed area and side wall area. The bed area, A_{bed}, is equal to the breach width times the length of flat top reach, where the side area needs consider the trapezoidal shape of the embankment body. Fig. 4.6 shows the projection area (grey shaded), A_{side}, of the breach side wall onto the vertical plane normal to the embankment length. The total erodible area is given as

$$A_{e,tot} = A_{bed} + n_{loc} A_{side} \frac{1}{\sin\beta} \tag{4.15}$$

where β = breach side slope angle with respect to the horizontal (Fig. 4.7); the factor $\sin\beta$ is introduced to convert the projection side area to the area of the inclined side surface of the breach; and n_{loc} = indicator of breach location: =1 for one-sided breach and 2 for breach located at the middle of embankment length. The one-sided breach means that one side of the breach is not erodible and the breach can extend only on the other side.

As shown in Fig. 4.7. the breach width at the water surface or at the dam crest, ΔB, has the following relation with Δz_b:

$$\Delta B = \frac{n_{loc}\Delta z_b}{\sin\beta} \tag{4.16}$$

where the factor $\sin\beta$ is introduced in Eq. (4.16) to convert the erosion layer thickness (normal to the side wall) to the horizontal width.

For the bottom width change of the breach, Δb, has the following relation:

$$\Delta b = n_{loc}\Delta z_b\left(\frac{1}{\sin\beta} - \frac{1}{\tan\beta}\right) \tag{4.17}$$

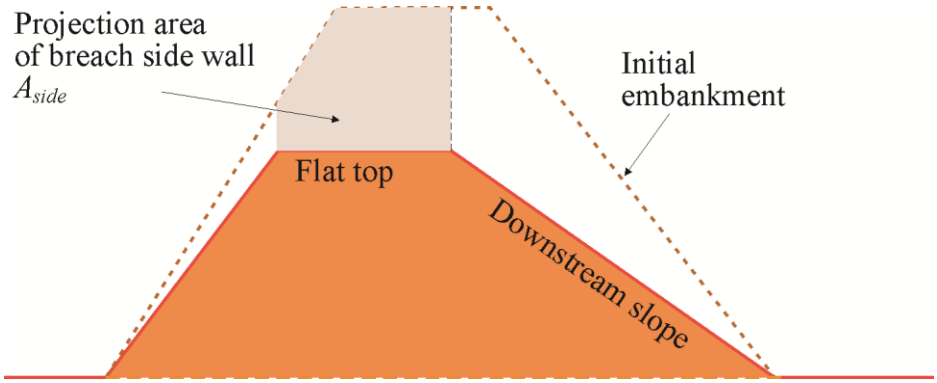

Fig. 4.6. Breach Side Area on the Flat Top

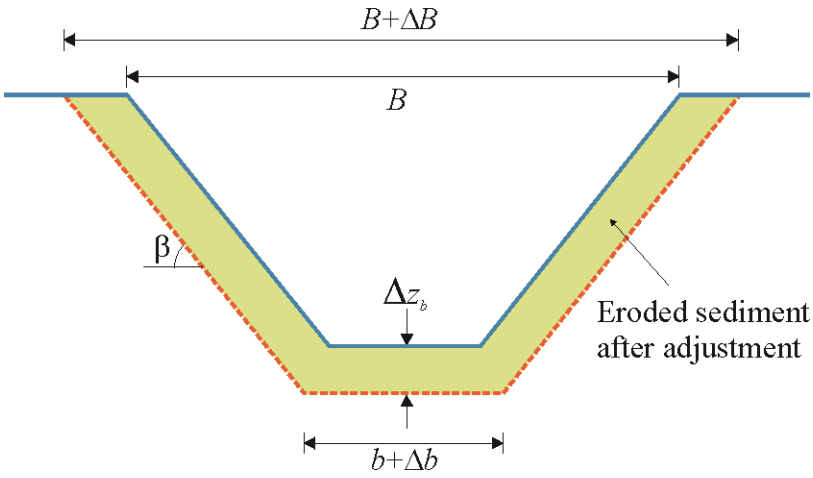

Fig. 4.7. Allocation of Sediment Erosion along Cross-Section

4.3.2. Allocation of Breach Morphology Changes in the Downstream Slope Reach

For the downstream slope reach, the lateral erosion rate is affected by the ratio of the breach widths of the downstream slope and flat top reaches. If the downstream breach width is much larger than the flat top breach width, separation or slow flow will appear along the two downstream side walls and the lateral erosion will be reduced. Therefore, a correction factor c_b is introduced in Eq. (4.16) to determine the width change of the downstream slope reach as follows:

$$\Delta B = \frac{n_{loc} c_b \Delta z_b}{\sin \beta} \tag{4.18}$$

with the correction factor c_b:

$$c_b = \min\left[1,\ \max\left(0,\ 1.8\frac{b_{up}}{b_{down}} - 0.8\right)\right] \tag{4.19}$$

where b_{up} = bottom with of the flat top reach, and b_{down} = bottom width of the downstream slope reach.

Correspondingly, the bottom width change at the downstream slope reach is determined with

$$\Delta b = n_{loc} \Delta z_b \left[\max\left(\frac{c_b}{\sin\beta}, \frac{1}{\tan\beta}\right) - \frac{1}{\tan\beta}\right] \tag{4.20}$$

However, because the downstream slope rotates about the downstream embankment toe, the erosion thickness is zero at the downstream toe, and linearly increases along this slope, as shown in Fig. 4.8. Thus, it is needed to consider the linear profile of erosion thickness in the determination of the total erodible area $A_{e,tot}$ in Eq. (4.14) for the downstream slope reach. Details are not given here because of the complex geometry.

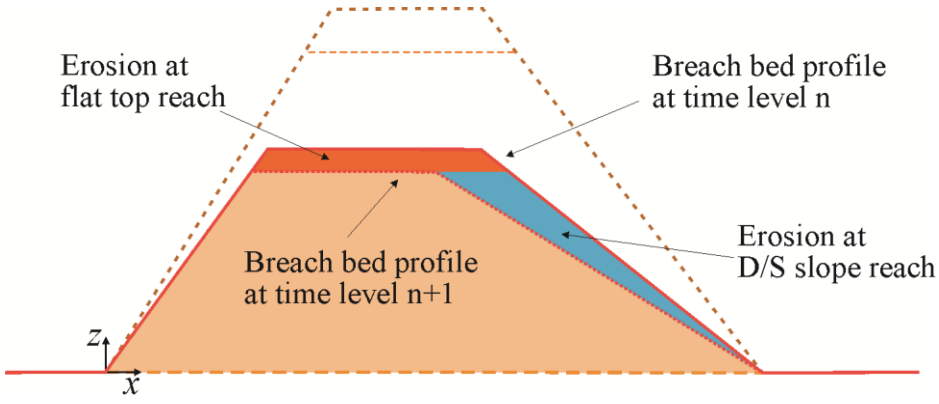

Fig. 4.8. Erosion Distribution along the Downstream Slope

After the allocation of the erosion along the breach cross-section and longitudinal section, the model simulates the temporal evolution of the longitudinal profile for one-way breach as shown in Fig. 4.9. The upstream slope does not change if the flow direction is unidirectional. The flat top lowers due to erosion, and the downstream slope rotates about the downstream toe. In the latter stage the flat top disappears because of the advance of the edge between the two reaches, and then the breach profile consists of only the slope. Once the slope erodes away, the breach reaches to the embankment bottom, but widening continues along the two sides of the breach (this is not shown in the side view of Fig. 4.9).

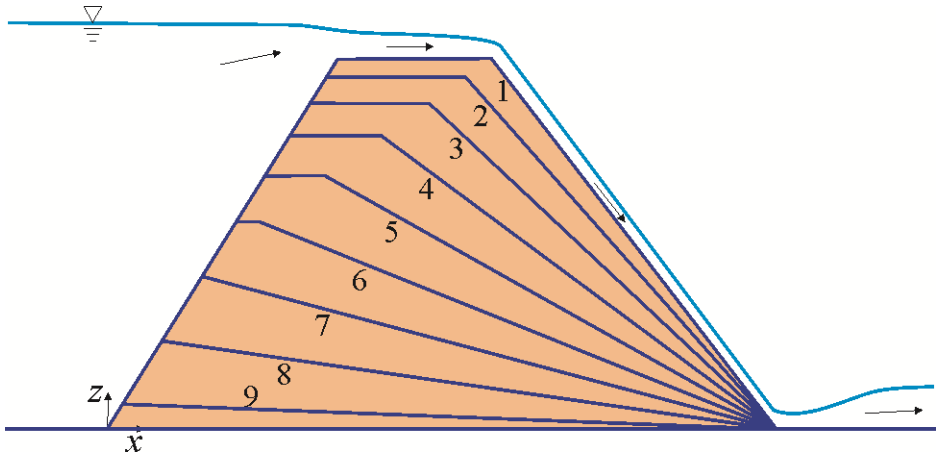

Fig. 4.9. Temporal Evolution of Longitudinal Profile of One-Way Breach by Surface Erosion in the case of Homogeneous Embankment (Numbers denote time slots)

After the embankment body is eroded away, erosion may continue into the embankment base (if the base is erodible) and undercut the breach side slopes. In this stage, DLBreach assumes the breach widening rate to be 1.6 times the deepening rate, and thus Eq. (4.18) is applied to the breach with c_b=1.6. This treatment considers the fact that subbase erosion should be suppressed by the downstream inverse bed slope.

4.4. Breach Side Slope

The breach side slope depends on the soil properties, breach bank height, water table and so on. Fig. 4.10 shows the force diagram of a side slope with angle β. Like a river bank, the breach side wall may fail by various mechanisms, including planar, rotational, cantilever, or piping-sapping type (see Osman and Thorne 1988; Wu 2007). The planar failure mechanism is considered here. Assuming the failure plane has an angle of α and intersects the slope at the bank toe. The driving force for the failure, F_d, is the weight of the failure block, and the resistance force, F_r, includes the friction and cohesion forces:

$$F_d = W\sin\alpha = \frac{1}{2}\gamma_b H^2\left(\frac{1}{\tan\alpha}-\frac{1}{\tan\beta}\right)\sin\alpha \tag{4.21}$$

$$F_r = W\cos\alpha\tan\phi + \frac{CH}{\sin\alpha} = \frac{1}{2}\gamma_b H^2\left(\frac{1}{\tan\alpha}-\frac{1}{\tan\beta}\right)\cos\alpha\tan\phi + \frac{CH}{\sin\alpha} \tag{4.22}$$

where H = slope height, W = weight of the failure block, γ_b = bulk specific weight, ϕ = friction angle, and C = cohesion of the soil. Note that the water pressures from the breach flow and groundwater are assumed to be equal, so that they are not included in Eqs. (4.21) and (4.22). The bulk specific weight has a relationship:

$$\gamma_b = (1-p')\gamma_s + f_w p'\gamma_w \tag{4.23}$$

where p' = porosity of embankment soil, γ_s = sediment specific weight, γ_w = water specific weight, and f_w = fraction of porosity occupied by water. f_w is related to the weather conditions, reservoir water level and ground water table. It has values between 0 and 1, and here is set as 0.5 considering breach side walls submerged partly.

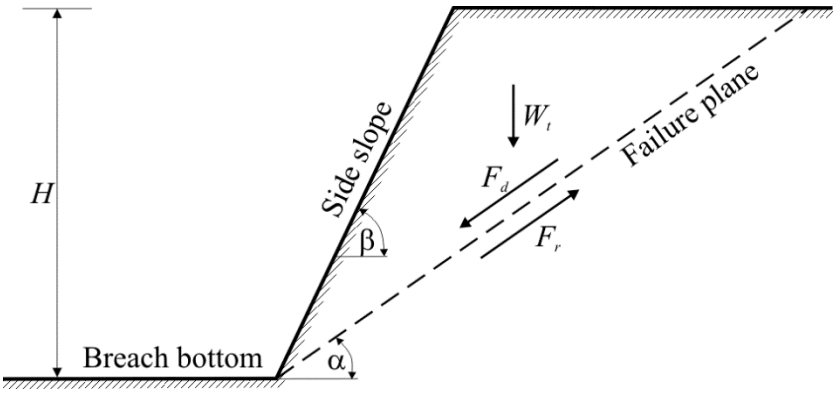

Fig. 4.10. Breach Slope Mass Failure: Planar Failure

The slope stability requires $F_d \le F_r$, which leads to the following inequality:

$$\left(\tan\alpha - \frac{1}{2}\frac{1+\frac{\tan\phi}{\tan\beta}}{\frac{2C}{\gamma_b H}+\frac{1}{\tan\beta}}\right)^2 \ge \frac{1}{4}\left(\frac{1+\frac{\tan\phi}{\tan\beta}}{\frac{2C}{\gamma_b H}+\frac{1}{\tan\beta}}\right)^2 - \frac{\frac{2C}{\gamma_b H}+\tan\phi}{\frac{2C}{\gamma_b H}+\frac{1}{\tan\beta}} \tag{4.24}$$

which is always satisfied for any given α, if $\frac{1}{4}\left(\frac{1+\frac{\tan\phi}{\tan\beta}}{\frac{2C}{\gamma_b H}+\frac{1}{\tan\beta}}\right)^2 < \frac{\frac{2C}{\gamma_b H}+\tan\phi}{\frac{2C}{\gamma_b H}+\frac{1}{\tan\beta}}$. This leads to the following slope stability condition:

$$\frac{1}{\tan\beta} \geq \frac{1}{\tan\phi} + \frac{1}{\tan^2\phi}\left[\frac{4C}{\gamma_b H} - \sqrt{\left(\frac{16C^2}{\gamma_b^2 H^2} + \frac{8C}{\gamma_b H}\tan\phi\right)\left(1+\tan^2\phi\right)}\right] \tag{4.25}$$

The steepest stable slope angle, denoted as β_s, can then be determined by changing inequality (4.25) to an equation, i.e. replacing "≥" by "=". This slope corresponds to a failure angle, α_s, determined by

$$\tan\alpha_s = \frac{1}{2}\frac{1+\frac{\tan\phi}{\tan\beta}}{\frac{2C}{\gamma_b H}+\frac{1}{\tan\beta}} \tag{4.26}$$

Note that for a non-cohesive soil, C=0, Eqs. (4.25) and (4.26) reduce to $\beta_s = \alpha_s = \phi$.

An embankment breaching usually starts from a side slope less than β_s. As the breach erodes vertically on the bottom and laterally at the side slope toes, the side slopes become steeper, until the angle β_s is reached and a failure occurs. The new slope will have the angle of α_s. The breach will repeat this deepening, widening and failure process. Therefore, the breach side slope is between the steepest stable angle β_s and its corresponding failure angle α_s. DLBreach assumes the breach side slope β as the average of β_s and α_s:

$$\beta = \frac{\alpha_s + \beta_s}{2} \tag{4.27}$$

The above model suggests that for non-cohesive soils β is close to the repose angle, and for cohesive soils β tends to be steeper. A higher bank tends to be less stable and have a smaller β. On the other hand, a soil with more cohesion tends to be more stable and have a larger β.

At each time step, the slope angle β is determined by using Eq. (4.27). It is then used in Eqs. (4.16) and (4.18). If the β value changes between the previous and current time steps, mass failure occurs. The soil block between the old and new slope angles is washed downstream instantaneously. Because Eq. (4.27) uses the average value as the new slope angle, the soil block between the old and new slope angles is only half the actual mass failure block. The other half of the block is gradually released to the channel bottom by keeping the same side slope angle until the next mass failure event.

Fig. 4.11 shows the temporal evolution of the breach cross-section modeled by DLBreach for a cohesive embankment or non-cohesive embankment with apparent cohesion. At the beginning, the breach side slope is usually vertical due to a shallow depth of the initial pilot breach. As breach deepens, it widens. When the breach is deep enough, its side walls loose stability and mass failure occurs. This leads to reduction of the side slope. As the breach continues deepening, it widens and its side walls fail again. When the erosion reaches to the non-erodible foundation, only lateral widening continues. Even though no obvious mass failure occurs after erosion reaches the erosion-resistant bottom, the model actually considers mass failure during the final widening by using the average side slope expressed in Eq. (4.27).

The breach side slope determined above using Eq. (4.27) is for the flat top reach. For simplicity, the breach side slope in the downstream slope reach is assumed to be the same as that in the flat top reach.

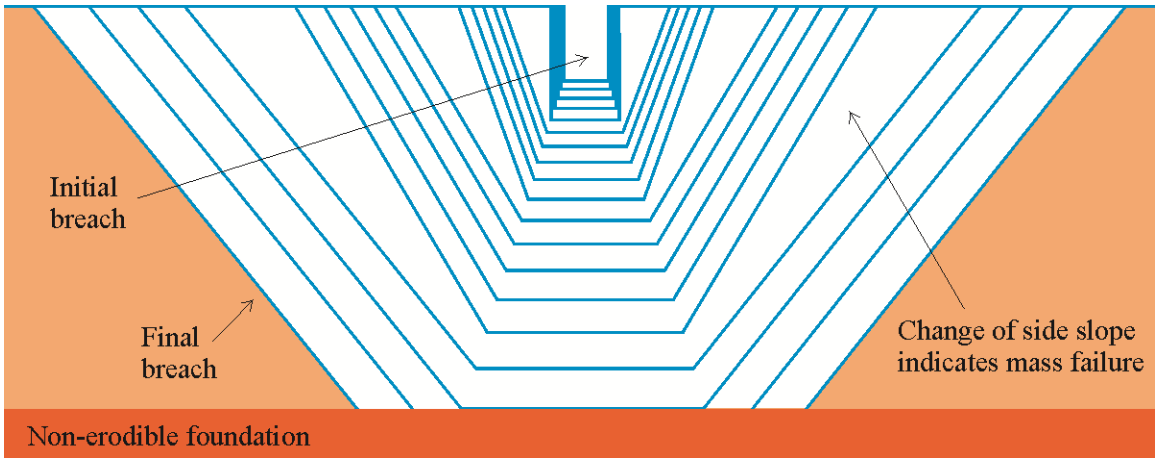

Fig. 4.11. Temporal Evolution of Breach Cross-Section by DLBreach
(Reduction of side slope is due to breach deepening and mass failure)

4.5. Breaching by Headcut Migration

When headcut is considered as the breaching mode, the longitudinal section of the breach is approximated as shown in Fig. 4.12(a), also described in Section 2.1.2. As the headcut migrates upstream, the breach top flat reach upstream of the headcut experiences the action of hydraulic shear and may lower and widen. This erosion process is computed using the cohesive sediment erosion model presented in Section 4.2, which is not repeated here.

Various kinds of empirical and numerical models have been established to determine the headcut migration (Temple 1992; Temple and Moore 1994; Wu and Wang 2005). DLBreach implements three energy-based headcut migration models to determine the time averaged migration rate of headcut. The first option is the formula used in the SITES program (USDA-NRCS 1997):

$$\frac{dx}{dt} = C_1\left[\left(qH\right)^{1/3} - A_0\right] \tag{4.28}$$

where C_1, A_0= material-dependent coefficients, q = unit discharge (ft^2/s) and H = headcut height (ft). The coefficient C_1 and A_0 are related to the headcut erodibility index:

$$C_1 = \begin{cases} -0.79\ln K_h + 3.04 & K_h < 18.2 \\ 0.75 & K_h \geq 18.2 \end{cases} \tag{4.29}$$

$$A_0 = \begin{cases} 0 & K_h < 0.01 \\ \left[189 K_h^{1/2} e^{-3.23/\ln(101 K_h)}\right]^{1/3} & K_h \geq 0.01 \end{cases} \tag{4.30}$$

where K_h is the headcut erodibility index. K combines constituent geological parameters: earth material strength, block or particle size, discontinuity shear strength or interparticle bond shear strength, and relative ground structure (USDA-NRCS 1997).

The second option is the formula of Temple (1992):

$$\frac{dx}{dt} = C_T q^{1/3} H_e^{1/2} \tag{4.31}$$

where C_T = material-dependent coefficient of headcut migration ($m^{-1/6}s^{-2/3}$), and H_e = elevation change in energy grade line through the headcut (m), approximated as the overfall height H. The unit of q is m^2/s here.

The third option is the formula of Temple et al. (2005)

$$\frac{dx}{dt} = C_2 \left(qH\right)^{1/3} \tag{4.32}$$

where C_2 = material-dependent coefficient ($s^{-2/3}$). The coefficient C_2 is linearly related to the erodibility coefficient k_d (Hanson et al. 2011) that can be measured using the submerged jet test device (Hanson and Cook 2004).

Among the three options, option 2 is tested well in the Model Testing chapter and used as the default option.

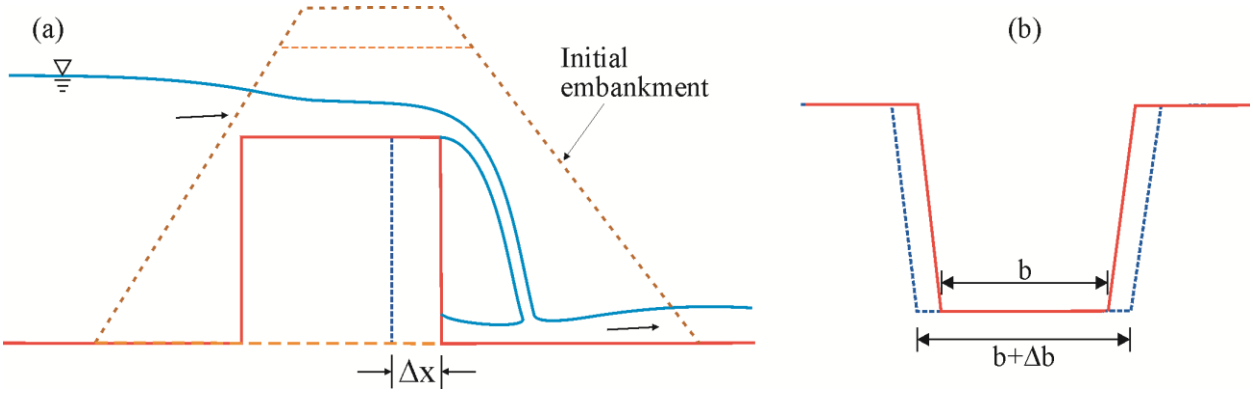

Fig. 4.12. Headcut Migration and Lateral Widening: (a) Longitudinal Section, (b) Cross-section

Note that Eqs. (4.28), (4.31) and (4.32) consider the migration of a headcut with constant height. When they are applied at the initial stage before the headcut reaches the dam crest, a correction is made to the migration rate by multiplying a factor of H/h_x. Here, H is the headcut height at dam crest, and h_x is the drop height at the brink point shown in Fig. 4.13. This treatment implies the early headcut migration is still controlled by the headcut overfall flow

energy, but the eroding material is only that at the brink point and with a smaller height. Since the eroding material is less, the headcut migration rate is faster. In order to make this correction factor works at the downstream toe, it is implemented as min(H/h_x, 0.01H).

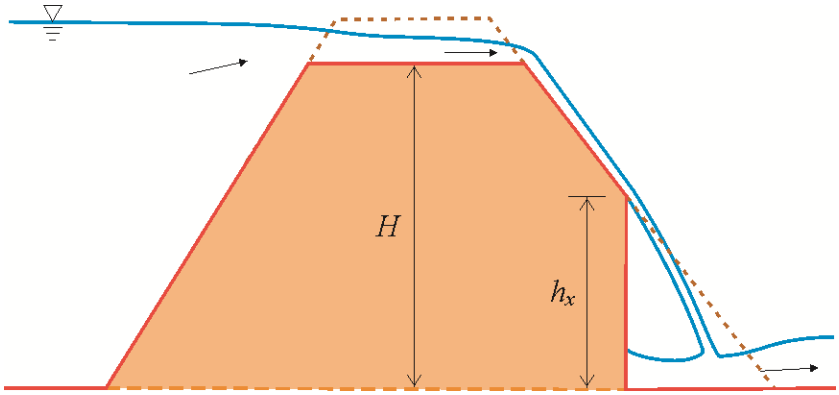

Fig. 4.13. Headcut Migration at the Initial Stage before Reaching the Dam Crest

As the headcut moves upstream, the channel immediately downstream of the headcut expands laterally due to erosion at the toe of the side walls. The lateral erosion or widening rate is assumed to be proportional to the headcut migration rate, i.e., $\Delta b = \alpha_c \, n_{loc} \, \Delta x$. Δx is defined in Fig. 4.12, and the proportionality coefficient α_c is tested as about 0.165 using the data reported in the chapter of Model Testing but may vary for different soils.

The stability of the embankment body upstream of the headcut is assessed by comparing the driving and resistance forces in the horizontal direction. A horizontal sliding failure mode is used, with the failure plane along the bottom of the embankment body, as shown in Fig. 4.14. The driving forces for the failure include the water pressure on the upstream slope of the embankment and the flow shear on the top section of the breach, whereas the resistance forces include the soil cohesion and friction at the embankment bottom and two sides of the headcut, and water pressure from the tailwater. If the resultant driving force is larger than the resultant resistance force, a failure will occur; otherwise, the headcut will be stable. The input parameters of the stability analysis algorithm include the soil cohesion and internal friction angle.

Once the headcut loses its stability, the block of headcut may not be washed away instantaneously. In order not to disturb the flow and sediment calculations, DLBreach uses a virtual tank (a variable) to store the mass of the failed headcut block. The breach flow and sediment transport calculations are carried out without considering the failed headcut block, but the erosion does not apply to the breach morphology until the stored sediment in the virtual tank is empty. Then, the breach continues widening (and downcutting if the foundation is erodible). The widening process is simulated using the model described in Section 4.2.

Note that DLBreach provides two options for cohesive embankment breach by overtopping: surface erosion in Section 4.2 and headcut migration in this section. Headcut usually is the

breaching model for cohesive embankments. Therefore, the option of headcut migration is suggested as the default option.

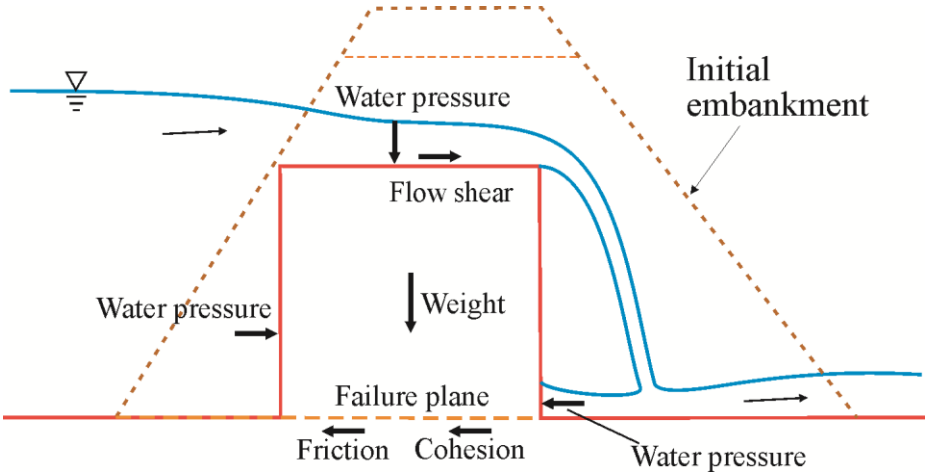

Fig. 4.14. Force Diagram on the Failure Block of the Headcut.

4.6. Breaching of Composite Embankment with Clay Core and/or Cover

If there is a clay cover on the top of the embankment, the model will start to erode the clay cover first and then the interior material. The cohesive soil erosion model in Section 4.2 is used to simulate the erosion of clay cover layer.

In the case of composite embankment with a clay core, the breach model in the previous section is used to calculate the erosion caused by overtopping flow at the top flat breach channel and the downstream slope at the early stage before the clay core is exposed to the flow. Once the clay core is exposed, the longitudinal section of the breach is conceptualized as shown in Fig. 4.15. The model determines the breach flow discharge using the broad-crested weir equation, and then computes the uniform flows at the downstream slopes of the clay core and lower shoulder. The erosions at the clay core top and downstream slope as well as the lower shoulder surface are calculated using the cohesive or non-cohesive sediment transport model depending on the soil properties. The sediment volume change is allocated along the bed and side walls at each reach in the same way as described in Section 4.3.

The stability of the clay core is assessed at each time step. The failure plane is assumed to be horizontal and intersect with the clay core downstream slope and the downstream shoulder surface, as shown in Fig. 4.15. The forces acting on the clay core failure block are similar to the case of headcut in Fig. 4.14, with addition of a pressure force from the upstream shoulder soil. The stability analysis algorithm used in the headcut case is extended to the clay core case. In addition, the failure mode of overturning has been also considered, but it is found that the sliding failure mode is more important in the test cases described in the Model Testing. Once the clay

core or its top portion loses stability, it is assumed that both the clay core failure block and the upstream shoulder soil are washed away. The collapsed core material is stored in a virtual tank as explained for headcut and pipe roof block failures, and release gradually to the downstream. After the clay core collapses, the breach will continue to enlarge vertically and laterally, which is simulated using the surface erosion model of homogeneous embankment with the volume-weighted average properties of the clay core and shoulder materials.

Fig. 4.16 shows the temporal evolution of the longitudinal breach profile in the case of composite dam with a clay core. The breach is divided into two reaches at the early stage before the clay core is exposed, as explained in Section 4.1. Once the core is exposed, the breach is divided into three reaches. Then, the clay core may fail due to significant erosion in the lower shoulder reach. After the core failure, the breach is divided into two reaches again. After the remaining material in the breach is washed out and the non-erodible foundation is exposed, the breach can still widen until the headwater is depleted or the tailwater is raised.

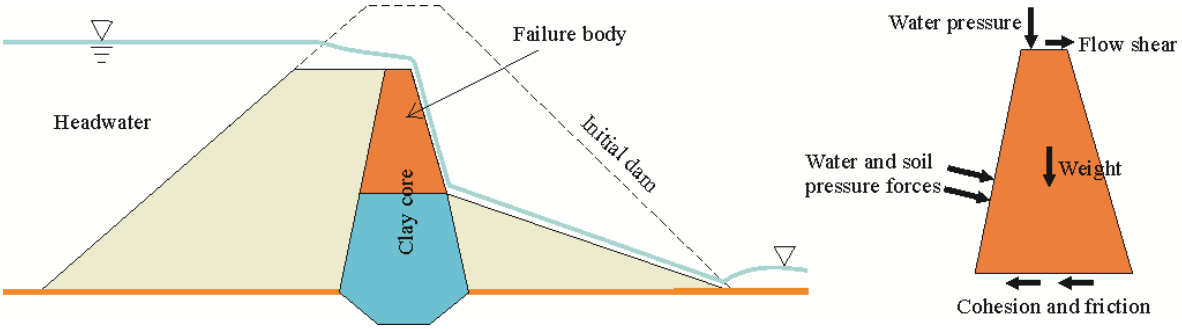

Fig. 4.15. (left) Sketch of breach of composite embankment with a clay core and (right) force diagram of the failure body.

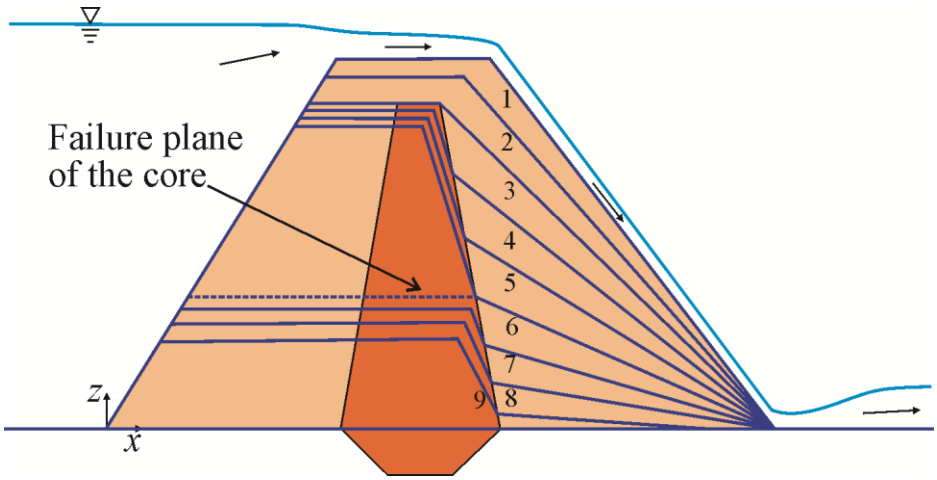

Fig. 4.16. Temporal Evolution of Longitudinal Profile of One-way Breach in the Case of Composite Dam (Numbers denote time slots)

4.7. Breaching by Piping

The erosion at the pipe perimeter is determined using the sediment transport model in Sections 4.1 and 4.2 for non-cohesive or cohesive soils. The erosion thickness is assumed to uniformly distribute on the pipe surface and along the length. The pipe is enlarged at each time step until the collapse of the roof part of the embankment.

The failure of the roof part is determined by comparing the driving and resistance forces in both vertical and horizontal directions. The failure is assumed along the vertical planes extended from two side walls of the pipe. In the vertical direction, the driving forces for the pipe roof failure are the weight of the failure body and the vertical component of the water pressure on the upstream slope above the pipe, and the resistance force is the soil cohesion on the two side failure planes. In the horizontal direction, the driving force is the horizontal component of the water pressure on the upstream slope above the pipe, and the resistance force is the soil cohesion on the failure planes. Once the driving force is larger than the resistance force in either vertical or horizontal direction, the roof part above the pipe will collapse. Then, the overtopping flow module is then used to simulate the breach process.

The failed pipe roof block is assumed to remove from the breach immediately, but stored in a virtual tank (a variable). In the next time steps, the model calculate the flow and sediment transport without considering the failed pipe roof material, but does not change the breach geometry until the mass stored in the virtual tank is completely eroded away. This treatment is also used for the side slope failure and clay core failure mentioned above. It allows gradual release of the failure block to the downstream and avoids the possible instability caused by sudden, discrete mass failure events during the breaching process.

4.8. Embankment Base Erosion

In the case of erodible foundation, the model allows erosion into the foundation. The breach is assumed to have a flat horizontal bottom surface and can lower to a value predefined according to the foundation material properties (Fig. 3.1(b)), but the base erosion does not affect the upstream and downstream water levels. The breach flow discharge is determined using Eq. (3.1) or (3.3). As erosion continues into the foundation, breach widens laterally until the breaching is finished.

4.9. Longshore Sediment Transport along the Shorelines

DLBreach considers the longshore sediment transport from the adjacent beach as a sediment source for the inlet or breach evolution. The longshore transport rate is calculated using the

formula of CERC (U.S. Army Coastal Engineering Research Center, 1984) or the formula of Kamphuis (2002). The CERC formula is written as

$$Q_s = K\sqrt{\frac{g}{\gamma_b}}\frac{H_{sb}^{5/2}\sin 2\alpha_b}{16(s-1)a'} \tag{4.33}$$

where Q_s is the longshore sediment transport (m^3/s), γ_b is the ratio of wave height to water depth at breaking (about 0.9), a' is the ratio of solid to total volume for the sediment, s is the specific gravity of sediment, H_{sb} is the significant wave height at breaking, α_b is the wave breaking angle, and K is a coefficient commonly taken as 0.32 for typical beach sands.

The Kamphuis (2002) formula is

$$Q_u = 2.27H_{sb}^2T_p^{1.5}\left(\tan\beta_b\right)d_{50}^{-0.25}\left(\sin 2\alpha_b\right)^{0.6} \tag{4.34}$$

where Q_u is the submerged mass transport alongshore (kg/s), $\tan\beta_b$ is the beach slope, and d_{50} is the sediment median diameter.

In the current version, only noncohesive sediment from adjacent shores is considered. The longshore sediment transport is set as the source in the nonequilibrium sediment transport model in the existing DLBreach.

Chapter 5. Model Parameters

The DLBreach model parameters are introduced in this chapter. Theses parameters are prepared and stored in one input file. The input file's formats refer to the technical report: Wu (2016), "Inputs and Outputs of DLBreach – A Simplified Physically-Based Dam/Levee Breach Model, Version 2016.4." The following text groups the parameters into several categories, and provides guidance on how to estimate some of the key parameters. Important suggestions are highlighted using colored text.

Time Period and Time Step

Time step is used in the calculations of head and tail water levels and breach morphology changes. It is in seconds. Its value can be from 0.1 s to 5 s, varying case by case. *For laboratory cases, it is smaller, such as 0.1-1 s. For field cases, it can be larger, such as 1-5 s.* It is suggested to try different time step values and make sure that the model is stable and the results are not dependent on the time step length.

The beginning and ending times of the simulation period are needed. Both are in seconds. The model stops when the ending time is met.

Embankment Dimensions and Configurations

The dam or levee embankment is approximated as a trapezoid along its cross-section. Its dimensions are characterized by height (in m, i.e., meters), crest width (in m), upstream slope (unitless), downstream slope (unitless) and length (in m). The upstream and downstream slopes are defined as vertical/horizontal (V/H) ratio. Note that the embankment height measures from the crest to bottom. Do not confuse it with the dam crest elevation referred to a geo-reference datum. The embankment length is the base length, which is the maximum bottom width which the breach can develop to.

If a clay core exists, it is approximated as trapezoidal along the embankment cross-section. The core height (in m), core crest width (in m), upstream slope (V/H), downstream slope (V/H), and distance of core crest center to the embankment crest center (positive for downstream, in m) are needed.

If a clay cover exists, its thickness (in m) is needed. The cover can be on the flat top and/or the up- and downstream slope reaches.

If the embankment foundation is erodible, the base erosion depth needs to be specified. It is defined as the hard bottom elevation with reference to the embankment base (a negative value indicating below the embankment base). It is in m. Note that the hard bottom elevation should be the average one over the breach bottom width, because DLBreach uses a trapezoidal cross section to represent the breach.

Breach Mode

The breach mode needs to be predefined: = 1 for overtopping, and 2 for piping.

For overtopping breach, a sub-classification is defined through the card *Overtopping_Mode*: =1 for overtopping of homogeneous embankment with surface erosion mode (i.e., non-cohesive or uncompacted cohesive embankment); =2 for overtopping of homogeneous embankment with headcut erosion mode (i.e. compacted cohesive embankment); and =3 for overtopping of

composite embankment with clay core. *The default overtopping breach mode is 1 (surface erosion) for non-cohesive embankment, and 2 (headcut) for cohesive sediment, and 3 for composite embankment.*

DLBreach requires information on one- or two-sided breach. It is indicated by a card *Breach_Location*: =2.0 for breach located in the middle, or =1.0 on one side.

Pilot Breach

If overtopping is the breach mode, the initial breach cross-section is assumed as a trapezoid. The initial breach depth and bottom width are needed. Both are in meter. The breach depth measures from embankment crest to the breach bottom.

If pipping is considered, the initial breach pipe is assumed to have a square cross-section. The breach width is needed. The initial pipe vertical location needs to be given, which is defined with the depth measuring from the embankment top to the bottom of the breach pipe.

Note that the initial breach dimension is important for the breach formation and failure times, but usually it does not significantly affect the peak flow and final breach width. *The initial overtopping breach was assumed about 0.2-0.4 m deep and 1.0-5.0 m wide and the initial piping breach was 0.2 m high and wide in in most of the field cases tested in the next chapters. If no measurement data is available, this can be a reference.*

Hydrodynamic Parameters

Water properties used in DLBreach are water density and kinematic viscosity. The water density is in kg/m^3 (usually is about 1000 kg/m^3). The kinematic viscosity of water is in m^2/s, and is related to temperature. It is usually about 0.000001 m^2/s.

The Manning's coefficient *n* at the flat top and up/downstream slope sections of the breach is needed. If the clay core and/or clay cover exist, the Manning's *n* for these two materials are also needed. *DLBreach suggests that for non-cohesive sediments, the Manning's n is calculated with Eq. (3.6), with A_n = 16 for laboratory cases and 12 for field cases. For cohesive sediments, the Manning's n is suggested as 0.016. However, DLBreach does not perform the calculations using Eq. (3.6). The user is responsible to specify the n values through the input file. This allows the user to have choice of using different n values. Nevertheless, it is recommended to follow the suggestions since the model was tested based on them.*

For piping breach, the local head loss coefficient at the pipe entrance is also needed, suggested as 0.05. For overtopping breach, if the Keulegan equation is used, the local head loss coefficient at the breach entrance is needed.

Sediment Parameters

DLBreach requires choice of sediment transport model. It is indicated by a card "*Noncohesive_or_Cohesive_Sediment*": =1 for non-cohesive sediment; =2 for cohesive sediment. Though the term "clay core" is used for the internal core type of structure, the model allows using the non-cohesive sediment transport model for the core if the core material is not cohesive, by specifying the card "*Core_Noncohesive_or_Cohesive*" 1 or 2, similar to *nsedmod.*

For both cohesive and non-cohesive sediments, the sediment diameter (in meter), specific gravity (unitless), porosity (unitless), clay content (in fraction between 0.0 and 1.0), cohesion (in Pa), and internal friction coefficient ($\tan\phi$) have to be given. For cohesive sediments, the

diameter is a representative diameter of flocs, and is suggested as 0.03 mm. For non-cohesive sediments, the cohesion is needed, set as zero if no apparent cohesion exists. Note that non-cohesive sediment may have apparent cohesion.

For cohesive sediments, the erosion coefficient k_d ($cm^3/N\text{-}s$) and critical shear stress τ_c (in Pa) are needed. Evaluation of these two parameters refers to the model testing chapters. *Both are preferably measured. 2.5-30.0 $cm^3/N\text{-}s$ were used for k_d, and 0.15 Pa for τ_c in the thirty-five test cases related to cohesive sediments in the next chapters. These values can be used as reference when no measured data are available. Among these two parameters, k_d is more important. In fact, k_d is the most important one among all DLBreach parameters in the case of cohesive embankment. It is recommended to conduct sensitivity analysis by varying k_d values.*

If a clay core or cover exists, the above soil properties are needed for each soil.

For non-cohesive sediment, the coefficient λ in Eq. (4.11) for adaptation length is needed. λ=6.0 is suggested for field cases, and 3.0 for laboratory cases.

If headcut is chosen as the breaching mode, three formulas can be used to calculate the headcut migration rate, as described in Section 4.5. For formula 1, i.e. Eq. (4.28), the erodibility index is needed. For formulas 2 and 3, i.e., Eq. (4.31) and (4.32), the coefficient C_t and C_2 are needed. *For the present version, the default option is formula 2, with C_t of around 0.0025-0.0049 ($m^{-1/6}s^{-2/3}$) suggested in the test cases in the next chapter.*

Breach Side Slope

The model allows using a constant breach side slope or determines it using Eq. (4.27) derived from a stability analysis. The default option is the stability analysis. If a constant side slope is used, this is specified through the card "*Breach_Side_Slope_Constant*". The side slope is defined as the ratio of Vertical/Horizontal.

Upstream Routing

DLBreach allows two options for upstream flow routing. Option 1 is to perform the reservoir water balance routing for dam breach modeling, and Option 2 is to specify the time series of water level for levee breach modeling.

In Option 1 for dam breaching, there are five approaches to giving the reservoir volume or surface area versus elevation curve. Approach 0 specifies the pair values of reservoir volume and elevation. Approach 1 specifies the pair values of A_s and z. Approaches 2-4 use the power law $A_s=\alpha z^m$. In Approach 2, the reservoir storage volume and surface area for a given water level are known, and the exponent m is determined from these known parameters by the model. In Approaches 3 or 4, the reservoir storage volume or surface area for a given water level is known, and the exponent m is suggested as 2 (between 1-3).

In Option 2 for levee breaching, the pair values of elapsed time and water level at the headwater are used to represent the time series.

In addition, the initial water levels (in m) at the head and tail water are needed to initialize the model.

Downstream Routing

DLBreach allows three options for downstream flow routing to determine the tailwater level at each time step. Option 1 assumes a uniform flow in the downstream channel, which is

approximated as a straight rectangular channel. The channel width, channel slope and Manning's *n* are needed.

Option 2 performs the water balance routing in the downstream storage basin. The basin volume or surface area versus elevation curve is needed and specified as their pair values.

Option 3 specifies the time series of tailwater levels measured or calculated using another hydrodynamic model.

Inflow to Reservoir and Downstream Basin

The model allows specifying the inflow discharge to the upstream reservoir and downstream storage basin by using pair values of time (**in hours**) and discharge (in m^3/s).

Flows through Spillways and Sluice Gates

The model calculates flows through spillways and sluice gates on the embankment and off-site.

Model Outputs

The model generates outputs in ASCII format, consisting of the following columns for parameters:

Time (in hours), breach flow discharge (m^3/s), flow discharge through spillways/gates on embankment (m^3/s), upstream water level with reference to embankment base (m), downstream water level (m), breach bottom elevation (m), breach bottom width (m), breach top width (m), flow area at the breach (m^2), breach side slope (V/H), cumulative water volume from breach and spillway/gate (m^3), sediment discharge at upstream (m^3/s), sediment discharge at downstream (m^3/s).

Chapter 6. Model Testing in Cases of Dam Breach

DLBreach was tested against 50 sets of laboratory experiment and field case study data of dam breach (Wu 2013). The used data were selected from Wahl's (1998) and Xu and Zhang's (2009) compilations of historical dam failures, as well as several laboratory and field experiments, such as Chinnarasri et al. (2004), the IMPACT program (Morris et al. 2005), and Hanson et al. (2005). Because many field cases and even some experiment cases did not have the complete data as required by the model, the data sets had to be carefully selected. First, the selected cases had embankment configurations, such as height, crest width, up- and downstream slopes, and soil type. Second, the initial reservoir water level was known and the reservoir characteristics were represented by the surface area and water level (A_s-h) curve, reservoir water volume or surface area. Third, the breach characteristics, such as peak discharge, final breach width and failure time, or some of them, were measured or estimated, to validate the developed model.

The sediment size, clay ratio, and soil porosity of each case were specified using measurements if available, or estimated using the description such as "rockfill" and "earthfill".

The slope stability model in Eq. (4.27) was tested using a couple of cases with known side slope, soil cohesion and internal friction angle. However, the soil cohesion and friction angle were not known for many field cases. On the other hand, the final breach side slope was known mostly. This provides a way to estimate the soil cohesion and friction angle based on the breach side slope model. The soil friction angle can be estimated according to soil types. The average frication angle is between 34^o–40^o for gravel, 32^o–38^o for sand, 24^o–33^o for silt, and about 22^o for clay (*http://www.geotechdata.info/parameter/angle-of-friction*). The actual friction angle may vary by $\pm 3^o$–6^o from the average value, because it is also affected by other properties of the soil, such as moisture, clay fraction, chemical composition, and compaction. Once the friction angle is estimated, the soil cohesion can thus be determined by using the known final breach slope. Furthermore, the soil cohesion and friction angle are important factors for the stability of headcut, pipe top block, and clay core, and in turn influence the breach peak discharge, breach width and failure time. Therefore, the estimated soil cohesion and friction angle can be validated indirectly by comparing these calculated breach properties against measured data.

The following sections describe validations of the developed model using various types of dam failures caused by overtopping and piping mechanisms.

6.1. Cases of Noncohesive Homogeneous Dam Breach by Overtopping

Model Parameters

Ten cases of non-cohesive homogeneous dam breach due to overtopping flow were simulated using DLBreach. Their dam configurations, soil properties and reservoir characteristics are shown in Tables 6.1 and 6.2. These cases include five laboratory cases and

one field experiment case of the IMPACT program (Morris et al. 2005; Hassan and Morris 2008), two built dam failures, and two landslide dam failures. The two built dams, Castlewood in Colorado and South Fork in Pennsylvania, were zoned earthfill/rockfill, but treated as non-cohesive homogeneous dams because the zoned structures are not known. The sediment sizes are given from the literature (Morris et al. 2005; Hassan and Morris 2008; Hancox et al. 2005; Fread 2001; Singh 1996; Chen 2015), except that the Castlewood case is newly estimated according to the description of the dam. The breach was located at one end of the dam for the IMPACT lab #4 and in the middle for the other cases. The soil porosity is given as 0.4 for the laboratory cases and 0.22 for the field cases, approximately corresponding to different sediment sizes in these two settings.

The IMPACT field case 2 has information on the soil cohesion and friction angle, from which Eq. (4.27) predicts a final breach side slope of 51.3^o (1.25V:1H), which is somehow different from the steeper slope shown in the photos of Morris and Hassan (2009), perhaps due to the freezing condition encountered during the experiment. The soil in the Castlewood case exhibits cohesion (or apparent cohesion), which is estimated using Eq. (4.27), whereas the soils in other eight cases are treated as cohesionless.

The reservoir characteristics of the IMPACT cases are represented by the surface area and water level (A_s-h) curve, and the reservoir filling is computed from the given initial water level by using the water balance equation (3.16) with the specified time series of inflow discharge. In the other four field cases, the reservoirs are characterized by the reservoir storage volume, surface area or A_s-h curve, and the simulations start from the moment when overtopping just occurs.

Results

Figs. 6.1 and 6.2 compares the measured and calculated breach flow hydrographs and reservoir water levels for the IMPACT field case 2, which is chosen as a representative for the ten cases tested. The model reproduces well the evolution of reservoir water level in the first filling period, but the results exhibit difference in the second filling period. The calculated water level responds to the inflow, but the measured water level maintains almost unchanged due to unknown reasons. However, the general trends of the breach discharge and reservoir water level varying in time are reasonably well reproduced by the model.

The model results of peak breach flow (Q_p), final breach width (B), time to peak discharge (T_p), and failure time (T_f) for the ten cases are presented in Table 6.2. Because the experimental cases started from predefined water levels lower than the initial breach bottom elevations, the failure time are not available, whereas in the field cases the time to peak breach discharge is usually not available because of difficulties in obtaining it. Therefore, only the time to peak is compared for the experimental cases, and only the failure time for the field cases. The failure time is defined in the model as the time period from the beginning of overtopping to the moment when 99% of the final breach width is reached. However, the failure time is defined as from

inception to completion of breach in field observations (Wahl 1998; Singh 1996), which is only descriptive and may inherit significant errors due to emergency circumstances of dam failures. Overall, the model reproduces well the peak breach discharge, final breach width, and failure time. The statistics of the comparison will be shown together with other cases in the end of this chapter.

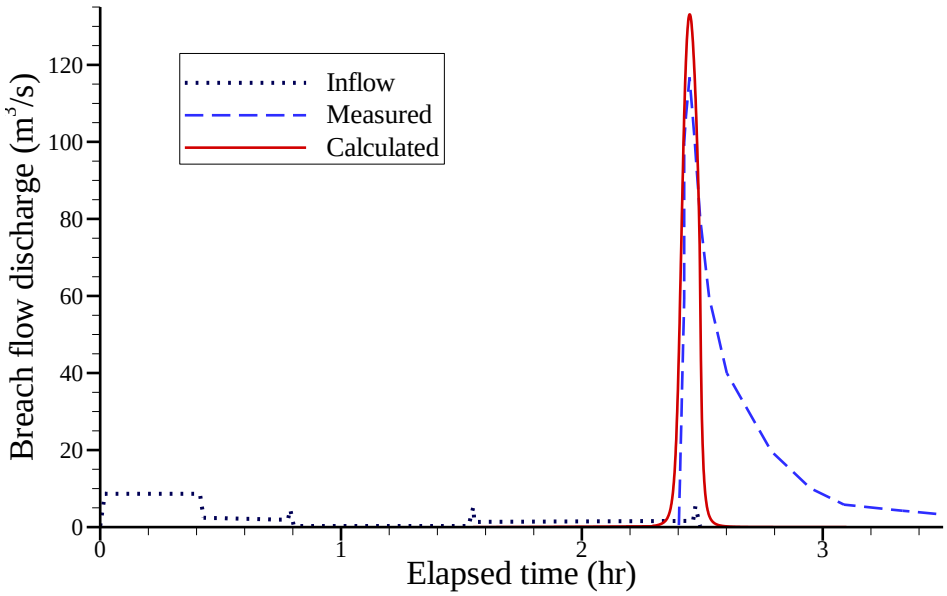

Fig. 6.1. Breach flow discharge for IMPACT field case 2

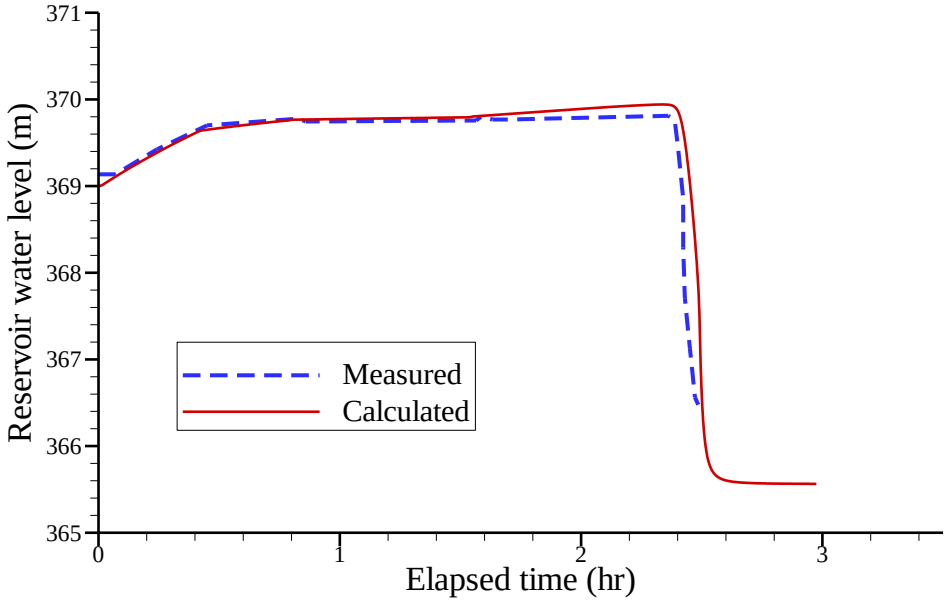

Fig. 6.2. Reservoir water level for IMPACT field case 2

Table 6.1. Conditions of non-cohesive dam overtopping failure cases

Dam No.	Dam name	Dam type	Dam height (m)	Crest width (m)	U/S slope (V/H)	D/S slope (V/H)	Reservoir storage (m^3)	Reservoir surface area (m^2)	Initial reser. level (m)	Initial breach depth (m)	Initial breach width (m)	Breach location	References
1	IMPACT Lab.#2	Earthfill	0.5	0.2	0.588	0.588		A_s-h	0.0	0.01	0.2	Middle	Morris et al. (2005)
2	IMPACT Lab.#4	Earthfill	0.5	0.2	0.588	0.588		A_s-h	0.0	0.01	0.2	One-side	Morris et al. (2005)
3	IMPACT Lab.#5	Earthfill	0.5	0.2	0.588	0.588		A_s-h	0.0	0.01	0.2	Middle	Morris et al. (2005)
4	IMPACT Lab.#6	Earthfill	0.5	0.2	0.5	0.5		A_s-h	0.0	0.01	0.2	Middle	Morris et al. (2005)
5	IMPACT Lab.#7	Earthfill	0.5	0.3	0.5	0.5		A_s-h	0.0	0.01	0.2	Middle	Morris et al. (2005)
6	IMPACT Field #2	Earthfill	5	2	0.526	0.625		A_s-h	4.10	0.10	2	Middle	Hassan & Morris (2008)
7	Castlewood, CO	Earth/rockfill/ masonary wall	21.34	4.9	0.333	1	4.23×10^6	8.094×10^5	21.34	0.4[a]	2.0[a]	Middle	Wahl (1998)
8	Yigong, China	Landslide dam	80	1.0[a]	0.068	0.068	2.38×10^9	5.04×10^7	80.0	5.0[a]	5.0[a]	Middle	Chen (2015)
9	Poerua, New Zealand	Landslide dam	80	0	0.21	0.45	$(5\text{-}7)\times10^6$	$\sim2\times10^5$	80.0	0.4[a]	3.0[a]	Middle	Hancox et al. (2005)
10	South Fork, PA	Zoned earth and rockfill	21.9	6	0.5	0.667	$\sim1.9\times10^7$		21.9	0.4[a]	3.0[a]	Middle	Singh(1996), Wahl(1998)

[a]: assumed values.

Table 6.2. Conditions and results of non-cohesive dam overtopping failure cases

Dam No.	Manning's n	d_{50} (mm)	p'	C (kPa)	tanϕ	Final side slope (V/H): measured vs. (model*)	Measured data				Calculated results			
							Q_p (m^3/s)	B (m)	T_p (hr)	T_f (hr)	Q_p (m^3/s)	B (m)	T_p (hr)	T_f (hr)
1	0.016	0.25	0.4	0	0.65[a]	(0.65)	0.91	2.75(av.)	1.20		0.903	2.560(av.)	1.205	
2	0.016	0. 25	0.4	0	0.65[a]	(0.65)	0.67	2.40(av.)	0.8		0.444	1.869(av.)	0.742	
3	0.016	0.25	0.4	0	0.65[a]	(0.65)	0.87	2.93(av.)	0.80		0.982	2.640(av.)	0.743	
4	0.016	0.25	0.4	0	0.65[a]	(0.65)	0.92	3.10(av.)	0.80		0.947	2.635(av.)	0.725	
5	0.016	0.25	0.4	0	0.65[a]	(0.65)	0.88	2.90(av.)	0.806		0.977	2.616(av.)	0.764	
6	0.034	4.65	0.22	0.9	0.9	(1.25)	117	15(av.)	2.45		133.11	17.07(av.)	2.447	2.484
7	0.057	100[a]	0.22[a]	15.5[a]	0.9[a]	2(2.03)	3570	54.9			3552.95	77.01	2.233	2.389
8	0.037	8	0.3	13	0.75	(1.01)	94013	432	6.17		98824.7	314.04	6.909	12.91
9	0.04	11	0.22[a]	0	0.8	0.8 (0.8)	2500	125		0.75	2819.63	134.26	1.175	1.562
10	0.041	14	0.22[a]	0	0.72	0.72 (0.72)	8500	128		0.75	10532.5	124.33	0.896	1.283

av.: average breach width, otherwise top width is compared. *: the final side slopes calculated with the model are given in parentheses on the sixth column.

6.2. Cases of Cohesive Homogeneous Dam Breach by Overtopping

Model Parameters

DLBreach was tested using eight cases of cohesive homogeneous dam breach by overtopping, including three laboratory cases and one field experiment case of the IMPACT program (Morris et al. 2005; Hassan and Morris 2008), one field experiment case of Hanson et al. (2005), and three built dam failures. The dam configurations, soil properties and reservoir characteristics of these cases are shown in Tables 6.3 and 6.4. All the dams were earthfilled and the breaches were located in the middle of dam length in the eight cases.

The soil cohesion and friction angle are known only in the IMPACT field case 1, in which the model predicts a vertical side slope at the beginning and a 45^o final breach side slope, which approximately agree with the photos provided by Morris and Hassan (2009). In the other seven cases, the soil friction angle ϕ is set between 26.5^o and 28.8^o (i.e. tanϕ =0.5–0.55); and the soil cohesion is back calibrated using the slope stability model from the known breach side slope in the Goose Creek case, but has to be estimated by trial and error to obtain generally good agreement between measured and calculated peak discharges, final breach widths and breach times in the remaining six cases in which the measured side slope is not available.

The soil porosity is given as 0.3–0.4 unless the measured values are available. The critical shear stress τ_c was set as 0.15 Pa and the Manning's n was set as 0.016 for all the eight cases. The measured erosion coefficient k_d was 10.3 and 17.68 cm^3/N-s for the USDA-ARS case E1S1 and IMPACT field case #1, respectively, whereas k_d had to be calibrated for the other cases. The calibrated k_d is between 5.35 and 7.2 cm^3/N-s for these cases, which are quite close to each other.

The implemented three headcut migration formulations have been tested. Because the soil properties are not available in most test cases, the model coefficients C_T, C_1 and C_2 need to be calibrated. It is found that C_T in Eq. (4.31) varies in a narrower range than C_1 and C_2. Eq. (4.31) is thus used to calculate the headcut migration rate. C_T is calibrated as 0.0049 m$^{-1/6}$s$^{-2/3}$ for the E1S1 case and 0.0025 m$^{-1/6}$s$^{-2/3}$ for the IMPACT field case 1, and the value of 0.0049 m$^{-1/6}$s$^{-2/3}$ is then used in other six cases.

Results

Table 6.4 presents the model results of peak breach flow, final breach width, time to peak discharge, and failure time for the eight cases. The failure time is defined as in the previous non-cohesive cases. Overall, the model reproduces well the peak breach discharge, final breach width and breach characteristic time.

Figs. 6.3 and 6.4 compare the measured and calculated breach flow hydrographs and breach widths varying with time for the experiment case E1S1 conducted by Hanson et al. (2005), chosen as a representative case of this group. The embankment was constructed 2.3 m high, with upstream and downstream slopes of 1:3 (vertical/horizontal) and a crest of about 1.84 m. The

embankment soil was non-plastic SM silty sand material, consisting of 5% clay, 25% silt, and 70% sand. The inflow discharge was 1.0 m^3/s. The initial breach channel was a trapezoid, 0.46 m deep and 1.83 m wide at its base. Fig. 6.3 shows that the measured breach hydrograph is slimmer than the calculated one. The peak breach flow is underestimated by the model, but the time to peak is well reproduced.

Fig. 6.4 shows that the calculated breach width increases very slowly at the beginning but significantly at the elapsed time of 20.5 minutes when the headcut migrates to the measurement location, the cross-section of the downstream top corner of the dam. The model differentiates the widths of the breach channels upstream and downstream of the headcut, and the downstream breach width is normally larger than the upstream one. This explains why the breach width increases suddenly as the headcut arrives at a specific location. Fig. 6.4 also shows that the measured breach width was about 0.5 m at the beginning, whereas the calculated breach width starts from the initial width (1.83 m) of the pilot breach channel. This might be due to that the concentrated flow forms a narrower channel on the downstream slope in the early development stage of the headcut, whereas the model assumes the same initial channel width at the flat top and downstream slope sections of the breach. Nevertheless, the general trend of the breach development is well captured by the model.

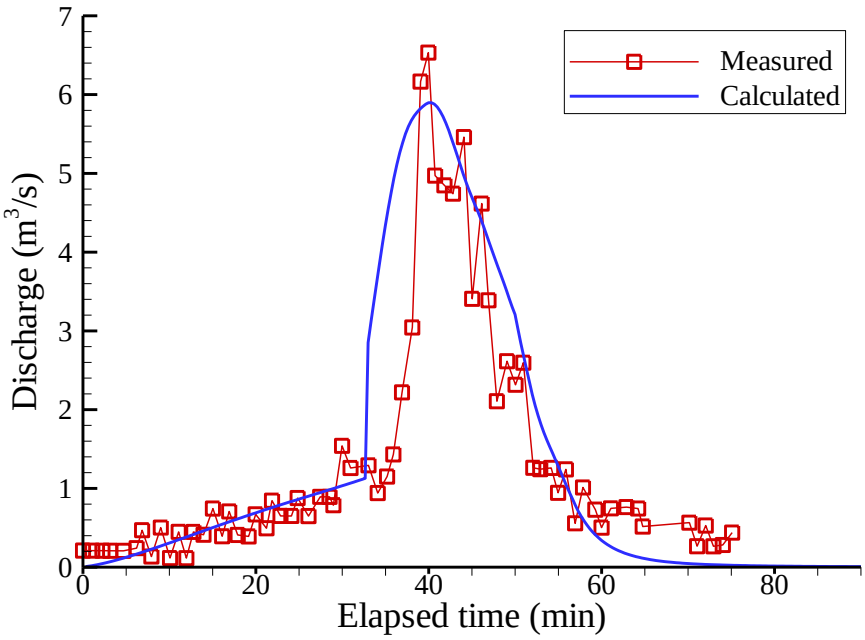

Fig. 6.3. Measured vs. calculated breach flow hydrographs for case E1S1

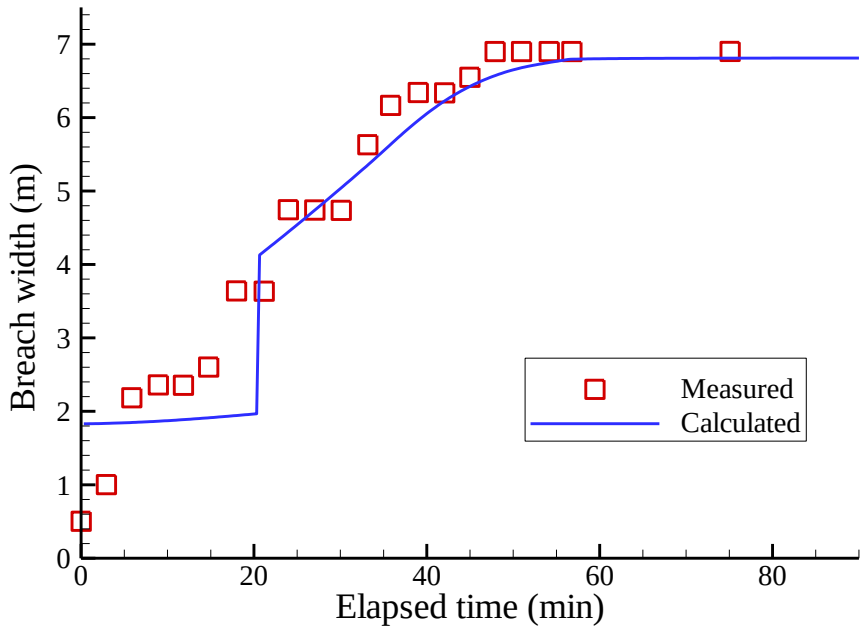

Fig. 6.4. Measured vs. calculated breach widths varying with time for case E1S1

Table 6.3. Conditions of cohesive dam overtopping failure cases

Dam No.	Dam name	Dam Type	Dam height (m)	Crest width (m)	U/S slope (V/H)	D/S slope (V/H)	Reservoir storage (m^3)	Inflow (m^3/s)	Initial reser. level (m)	Initial breach depth (m)	Initial breach width (m)	Breach location	Manning's n	References
11	IMPACT Lab.#10	Earthfill	0.6	0.2	0.5	0.5	A_s-h	$Q_{in}(t)$	0.58	0.05	0.14	Middle	0.016	Morris et al. (2005)
12	IMPACT Lab.#15	Earthfill	0.6	0.2	0.5	1.0	A_s-h	$Q_{in}(t)$	0.58	0.05	0.14	Middle	0.016	Morris et al. (2005)
13	IMPACT Lab.#16	Earthfill	0.6	0.2	0.5	0.333	A_s-h	$Q_{in}(t)$	0.58	0.05	0.14	Middle	0.016	Morris et al. (2005)
14	USDA-ARS E1S1	Earthfill	2.3	1.84	0.333	0.333	A_s-h	1.0	1.85	0.46	1.83	Middle	0.016	Hanson et al. (2005)
15	IMPACT Field #1	Earthfill	5.9	2.0	0.416	0.444	A_s-h	$Q_{in}(t)$	4.27	0.45	5.5	Middle	0.016	Hassan & Morris (2008)
16	Goose Creek, SC	Earthfill	6.7	3.0	0.667	0.667	1.06×10^7		6.7	0.2[a]	1.0[a]	Middle	0.016	Justin (1932), Wahl (1998)
17	Laurel Run, PA	Earthfill	12.8	6.1	0.333[a]	0.4[a]	V_w:5.55×10^5	100[a]	12.8	0.2[a]	1.0[a]	Middle	0.016	Wahl (1998)
18	Lijiaju, China	Earthfill	25.0	4.0	0.667	0.667	1.14×10^6		25.0	0.2[a]	1.0[a]	Middle	0.016	Xu & Zhang (2009)

Table 6.4. Conditions and results of cohesive dam overtopping failure cases

Dam No.	d_{50} (mm)	p'	Clay ratio	C (kPa)	tanϕ	k_d (cm^3/ N-s)	τ_c (Pa)	C_T in headcut Eq. (4.31)	Final side slope (V/H): measured vs. (model)	Measured data			Calculated results			
										Q_p (m^3/s)	B (m)	T_p (hr)	Q_p (m^3/s)	B (m)	T_p (hr)	T_f (hr)
11	0.005	0.4	0.45	20[a]	0.5[a]	7.6[a]	0.15	0.0049[a]	(vertical)	0.31	1.85	0.67	0.330	1.700	0.465	
12	0.005	0.4	0.45	20[a]	0.5[a]	7.6[a]	0.15	0.0049[a]	(vertical)	0.35	1.73	0.35	0.473	1.384	0.335	
13	0.005	0.4	0.45	20[a]	0.5[a]	7.6[a]	0.15	0.0049[a]	(vertical)	0.43	2.31	0.32	0.516	1.519	0.457	
14	0.025	0.35	0.05	15[a]	0.55[a]	10.3	0.15	0.0049[a]	(vertical)	6.53	6.90	0.666	5.897	6.810	0.672	
15	0.007	0.46	0.26	4.9	0.42	17.68	0.15	0.0025[a]	(1.07)	390/ 340		5.1/ 4.9	388.01		4.937	
16	0.03[a]	0.3[a]		13.2[a]	0.50[a]	5.35[a]	0.15	0.0049[a]	2(2.00)	565	30.5		536.02	39.12	3.150	7.827
17	0.03[a]	0.35[a]		25[a]	0.55[a]	7.2[a]	0.15	0.0049[a]	2.4(2.3)	1050	35.1(av.)		940.90	31.38(av.)	0.764	0.865
18	0.03[a]	0.3[a]		25[a]	0.55[a]	5.7[a]	0.15	0.0049[a]	(1.33)	2950			3190.6	64.27	0.611	0.659

6.3. Cases of composite dam breach by overtopping

Model Parameters

Six cases of composite dam breaching due to overtopping flow were used to test DLBreach. As listed in Tables 6.5 and 6.6, these cases include three laboratory cases of Chinnarasri et al. (2004) using cohesionless dam body with a 0.03 m thick clay cover, one field experiment case of earthen dam with clay core in the IMPACT program (Morris et al. 2005; Hassan and Morris 2008), and two built dam failures. The built dam Banqiao was earthfill with a clay core (Xu and Zhang 2009), and the other built dam Oros was zoned earthfill/rockfill (Gee 2008). The clay core dimensions in Banqiao Dam are assumed. The zoned structures of the Oros Dam are complex and thus approximated as the composite dam with a clay core.

The dam bases are allowed to erode in the cases of Banqiao and Oros, resulting in improved peak breach discharges in the simulations. In the Banqiao case, a base erosion of about 5 m was reported, i.e. the final breach height was about 5 m higher than the dam height (Xu and Zhang, 2009). A base erosion of 9 m is allowed in the simulation, considering that the scour hole near the dam might be somehow refilled by upstream incoming sediments in the end of the failure. A peak upstream inflow of 13,000 m^3/s was reported, and is thus used in the simulation.

The soil cohesion and internal friction angle before the core collapses are determined using the same approach as that in the cohesive homogeneous dam. After the core collapses, the dam material properties are represented by the volume-weighted average values of the core and shoulder materials. In addition, the sands in the test cases of Chinnarasri et al. (2004) exhibit apparent cohesion, which are estimated from the measured side slope. The breach was located in the middle of dam length in all the cases of this group.

Results

Table 6.7 summarizes the model results of peak breach flow, final breach width, time to peak discharge and dam failure time for these six cases. Overall, the model reproduces well these breach parameters.

Fig. 6.5 compares the measured and calculated breach discharges for the IMPACT field case 3, chosen as a representative of these six cases. It used a composite dam of 6.0 m high, failed due to overtopping (Morris et al. 2005; Hassan and Morris 2008). The upstream and downstream shoulders of the dam were built from rockfill with a central moraine core. The non-cohesive sediment transport model is used in this case because the moraine core sediment median size is about 7 mm and the shoulder rockfill sediment median size is 85 mm. The model predicts a final breach side slope of 62^o (1.89V:1H), which agrees generally well the photos provided by Morris and Hassan (2009). The measured and calculated peak discharges are 242.0 and 225.9 m^3/s, respectively. The calculated time to peak discharge is slightly later than the measured one. The agreement of calculated and measured breach hydrographs in Fig. 6.5 is plausible.

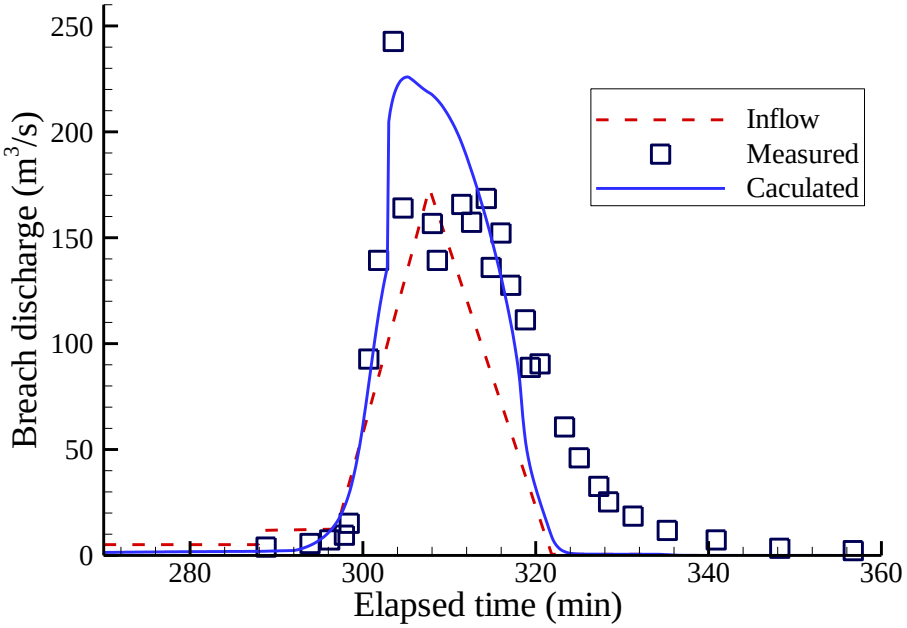

Fig. 6.5. Breach flow hydrograph for IMPACT field case 3

Table 6.5. Conditions of composite dam overtopping failure cases

Dam No.	Dam name	Dam type	Dam height (m)	Crest width (m)	U/S slope (V/H)	D/S slope (V/H)	Reservoir storage (m^3)	Inflow (m^3/s)	Initial reser. level (m)	Initial breach depth (m)	Initial breach width (m)	Breach location	Manning's *n* (Shoulder, Core/Cover)	References
19	Chinnarasri Test C1	Earthfill w/clay cover	0.6	0.3	0.333	0.333	A_s-h	0.0297	0.55	0.05	0.2	Middle	0.018, 0.016	Chinnarasri et al. (2004)
20	Chinnarasri Test C2	Earthfill w/clay cover	0.6	0.3	0.333	0.333	A_s-h	0.0384	0.55	0.05	0.2	Middle	0.018, 0.016	Chinnarasri et al. (2004)
21	Chinnarasri Test C3	Earthfill w/clay cover	0.6	0.3	0.333	0.5	A_s-h	0.029	0.55	0.05	0.2	Middle	0.018, 0.016	Chinnarasri et al. (2004)
22	IMPACT Field #3	Rockfill w/moraine core	5.9	3.0	0.645	0.645	A_s-h	$Q_{in}(t)$	4.5	0.24	6.1	Middle	0.055, 0.0365	Hassan & Morris (2008)
23	Banqiao, China	Earthfill w/clay core	24.5	8.0	0.384	0.5	V_w:6.075×10^8	13000	24.5	0.4[a]	5.0[a]	Middle	0.02, 0.016	Xu & Zhang (2009)
24	Oros, Brazil	Zoned earth/rockfill	35.4	5.0	0.276[a]	0.24[a]	6.6×10^8; A_s-h	1733	35.8	0.4[a]	5.0[a]	Middle	0.03, 0.021	Gee (2008)

WSL(t): given time series of water level in reservoir.

Table 6.6. Conditions of composite dam overtopping failure cases (continued)

Dam No.	Core											Shoulder				
	Height (m)	Crest width (m)	U/S slope	D/S slope	d_{50} (mm)	p'	Clay ratio	C (kPa)	tanϕ	k_d (cm^3/ N-s)	τ_c (Pa)	d_{50} (mm)	Specific gravity	p'	C (kPa)	tanϕ
19												0.44	2.5	0.35	1.27[a]	0.7[a]
20												0.44	2.5	0.35	0.65[a]	0.7[a]
21												0.44	2.5	0.35	0.45[a]	0.7[a]
22	5.25	1.5	4	4	7	0.244	0.0	20.0	1.0			85	2.65	0.235	0.4[a]	0.9
23	23[a]	3[a]	4[a]	4[a]	0.03[a]	0.3	-	30.0[a]	0.5[a]	18.0[a]	0.15	0.2	2.65	0.35	0.0	0.37[a]
24	35.4	5	0.9[a]	0.45[a]	0.2	0.35[a]	0.1	41.2	0.51	7.9[a]	0.15	2.5[a]	2.65	0.28[a]	0.0	0.85[a]

Table 6.7. Conditions and results of composite dam overtopping failure cases

Dam No.	Clay cover					Base erosion (m)	Final side slope (V/H): measured vs. (model)	Measured data				Calculated results			
	Thick-ness (m)	p'	Clay ratio	k_d (cm^3/ N-s)	τ_c (Pa)			Q_p (m^3/s)	B (m)	T_p (hr)	T_f (hr)	Q_p (m^3/s)	B (m)	T_p (hr)	T_f (hr)
19	0.03	0.4	0.9	6.8	0.15	0	4.5(4.58)	0.35	1.50		0.0833	0.408	1.818	0.0605	0.0828
20	0.03	0.4	0.9	6.8	0.15	0	2.0(2.06)	0.44	1.90		0.05	0.434	2.046	0.0547	0.0794
21	0.03	0.4	0.9	6.8	0.15	0	1.6(1.61)	0.405	2.13		0.058	0.506	2.316	0.0519	0.0724
22						0	(1.89)	242		5.1		225.9	17.16	5.086	
23						-9.0	0.36(0.52)	78100	372		5.5	71782.9	430.5	2.314	4.160
24						-4.0	1(1)	12000-58000	200		8.5	41371.0	200.0	2.734	6.866

6.4. Piping breach cases

Model Parameters

Twenty six cases of embankment breaching due to piping flow were computed using DLBreach. Shown in Tables 6.8 and 6.9, these cases include one field experiment case (IMPACT field #5) using moraine soil (Morris et al. 2005; Hassan and Morris 2008), four built dam failure cases (#26–29 in Table 6.8) using cohesionless soils, and twenty one built dam failure cases using cohesive soils. Twenty five cases were caused by piping, whereas the Sheep Creek case was caused by seepage, which is approximated as piping. The breach was located near one end of the dam for the cases of Davis Reservoir, Lake Frances, and Teton Dam, and in the middle for the other cases.

For the cases of La Fruta, Lake Latonka, and Lower Latham, the dam height is not available or much different from the breach height, so that the breach height is used to represent the dam height. Correspondingly, for La Fruta and Lake Latonka, the reservoir storage volume is replaced by the water volume above the breach bottom at failure, denoted as V_w. In several other cases, V_w is also used because the storage capacity is much different. In the cases of La Fruta, Lake Latonka, Lower Latham and Lower Two Medicine, the unavailable up- and downstream slopes are estimated using the dam height, bottom and top widths, from which the sum of the two slopes is derived. Various combinations of the two slopes are tested, and it is found that the model results are not significantly sensitive to them and thus equal up- and downstream slopes are used.

The soil porosity was given as 0.3–0.4, if they were not available in the measurements. For many piping cases, the initial piping location was unclear and was assumed to be near the dam bottom. The initial pipe was assumed to be 0.2 m wide and high for all cases, except 0.1 m is used in the Teton Dam case. The maximum base erosion depth was specified as the difference of dam height and breach height reported in Wahl (1998).

Results

Fig. 6.6 compares the measured and simulated breach flow discharges for the case of Teton Dam failure, chosen as a representative of the twenty six piping cases. The Teton Dam in Idaho was 93 m high, constructed in 1975 and failed in June 1976 due to piping. It is a one-sided breach case. The model shows the initial development of the breach due to piping, followed by the sudden collapse of the top. The breach flow increases rapidly due to this collapse and keeps constant for a while; then it increases significantly because of the wash-out of the flat crest of the weir. The calculated peak discharge is 64,272.7 m^3/s, while the measured peak discharge is 65,120 m^3/s (between 45,339-79,343 m^3/s). The measured peak discharge is represented by one point in Fig. 6.6, to compare with the calculated discharge hydrograph.

Table 6.9 presents the model results of peak breach flow, final breach width, time to peak discharge, and failure time for the twenty five cases. These important breach parameters are

generally well reproduced by the model. For the IMPACT field case #5, the moraine soil had cohesion but its median size was 7 mm, so that both the cohesive and non-cohesive sediment models are used and the predicted peak breach discharge is 151.95 and 119.97 m^3/s, respectively. The cohesive sediment model's prediction is more close to the measured peak discharge 171 m^3/s in this case.

The IMPACT field case #5 has the measured soil cohesion and friction angle, from which Eq. (4.27) predicts a vertical breach side slope that agrees well with the photos provided by Morris and Hassan (2009). In the case of Teton Dam Eq. (4.27) predicts an about 44.4^o final breach side slope based on the soil cohesion and friction angle similar to the values used by Singh (1996); this angle agrees with the measured 45^o. Together with a couple of cases in the previous subsections, these have validated the side slope model in Eq. (4.27) to certain extent.

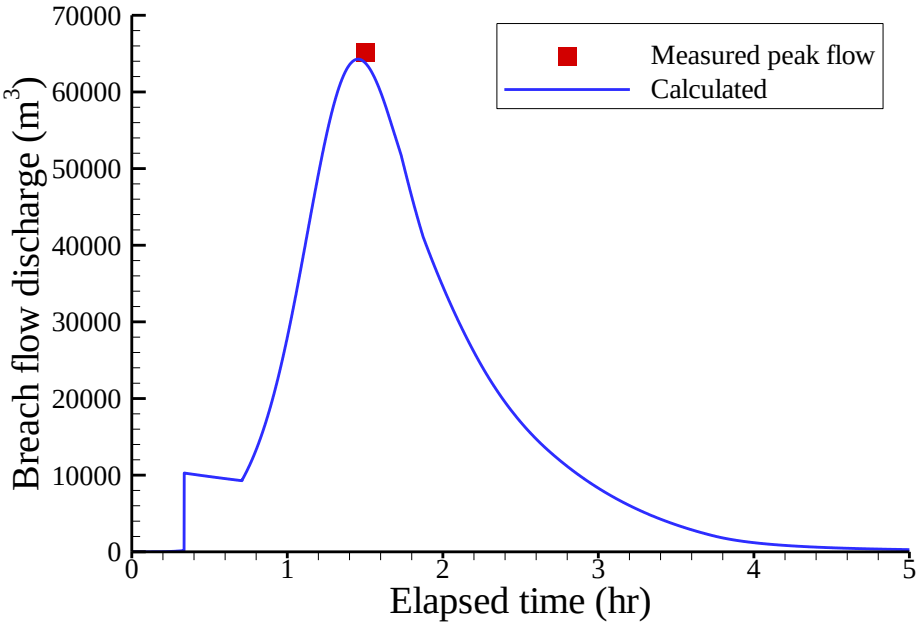

Fig. 6.6. Breach flow hydrograph for Teton Dam failure case

Table 6.8. Conditions of piping dam failure cases

Dam No.	Dam name	Dam type	Dam height (m)	Crest width (m)	U/S slope (V/H)	D/S slope (V/H)	Reservoir storage (m^3)	Reservoir surface area (m^2)	Initial reser. level (m)	Breach location	Manning's *n*	Base erosion (m)	References
25	IMPACT field #5	Moraine	4.3	2.8	0.714	0.714		A_s-h	4.0	Middle	0.036	0.0	Hassan & Morris (2008)
26	Big Bay, MS	Earthfill	15.6	17.0	0.333	0.333	1.75×10^7	3.64×10^6	13.5	Middle	0.02	-2.5[a]	Yochum et al. (2008)
27	Bradfield, UK	Rockfill	28.96	3.66	0.4	0.4	2.96×10^6		24.0	Middle	0.051	0.0	Wahl(1998), Justin(1932)
28	Lawn Lake, CO	Earthfill	7.9	2.4	0.667	0.333	9.87×10^5		7.9	Middle	0.021	0.0	Wahl(1998), Fread (2001)
29	Hell Hole, CA	Rockfill	67.06	21.3	0.667	0.667	V_w:3.06×10^7		45.72	Middle	0.051	0.0	Wahl (1998)
30	Apishapa, CO	Earthfill	34.14	6.1	0.333	0.5	2.25×10^7	2.59×10^6	31.04	Middle	0.016	0.0	Wahl(1998), Justin(1932)
31	Baldwin Hills, CA	Earthfill	47.2	19.2	0.5	0.556	1.1×10^6	7.689×10^4	43.0	Middle	0.016	0.0	Gallegos et al. (2009)
32	Bullock Draw Dike, UT	Earthfill	5.79	4.3	0.5	0.333	1.13×10^6		3.05	Middle	0.016	0.0	Wahl (1998)
33	Davis Reservoir, CA	Earthfill w/ concrete facing	11.89	6.1	0.5	0.5	1.3×10^7		11.58	One side	0.016	0.0	Singh (1996)
34	French Landing, MI	Earthfill	12.19	2.4	0.5	0.4	2.19×10^7		8.53	Middle	0.016	-2.0	Wahl(1998), Waymarking
35	Frenchman Creek, MT	Earthfill	12.5	6.1	0.333	0.5	2.1×10^7		10.8	Middle	0.016	0.0	Wahl (1998)
36	Hatchtown, UT	Earthfill	19.2	6.1	0.5	0.4	1.48×10^7		17.7	Middle	0.017	0.0	Wahl(1998), Sherard(1953)
37	Horse Creek, CO	Earthfill w/ concrete facing	12.19	4.9	0.667	0.571	2.1×10^7	4.856×10^6	8.23	Middle	0.016	-0.6	Wahl(1998), Justin(1932)
38	Johnston City, IL	Earthfill	4.27	1.8	0.211	0.364	5.75×10^5		3.05	Middle	0.016	-0.9	Wahl (1998)
39	Kelly Barnes, GA	Earthfill	11.58	6.1	1	1	V_w:7.77×10^5	1.7×10^5	11.3	Middle	0.016	-1.3	Wahl (1998)
40	La Fruta, TX	Earthfill	H_b:14.0	4.9	0.4[a]	0.4[a]	V_w:7.89×10^7		7.9	Middle	0.016	0.0	Wahl (1998)
41	Lake Avalon, NM	Earthfill	14.64	10.37	2.0	0.667	7.75×10^6		13.74	Middle	0.016	0.0	Wahl(1998), Singh(1996)
42	Lake Frances, CA	Earthfill	15.24	4.9	0.333	0.5	8.65×10^5	1.74×10^5	14.0	One side	0.016	-1.9	Wahl(1998), Justin(1932)
43	Lake Latonka, PA	Earthfill	H_b:8.69	6.1	0.594[a]	0.594[a]	V_w: 4.09×10^6		6.25	Middle	0.016	0.0	Wahl(1998), Singh(1996)
44	Little Deer Creek, UT	Earthfill	26.21	6.1	0.436	0.436	1.73×10^6		22.9	Middle	0.016	-0.9	Wahl (1998)
45	Lower Latham, CO	Earthfill	H_b:7.01	4.6	0.333[a]	0.333[a]	7.08×10^6		5.79	Middle	0.016	0.0	Wahl (1998)
46	Lower Two Medicine, MT	Earthfill	11.28	3.7	0.4[a]	0.4[a]	V_w:2.96×10^7		11.28	Middle	0.016	0.0	Wahl (1998)
47	Rito Manzanares, NM	Earthfill	7.32	3.7	0.746	0.746	2.47×10^4		4.57	Middle	0.016	0.0	Wahl (1998)
48	Sheep Creek, USA	Earthfill	17.07	6.1	0.333	0.5	V_w:2.91×10^6	3.44×10^5	14.02	Middle	0.016	0.0	Wahl (1998)
49	Spring Lake, RI	Earthfill w/ clay and gravel	5.49	2.4	1.333	1.333	1.35×10^5	7.284×10^4	5.49	Middle	0.022	0.0	Wahl (1998)
50	Teton, ID	Zoned earthfill	93	10.5	0.333	0.4	3.56×10^8	A_s-h	83.5	One side	0.016	0.0	Wahl(1998), Singh(1996)

Table 6.9. Conditions and results of piping dam failure cases

Dam No.	Initial piping elev. (m)	d_{50} (mm)	p'	Clay ratio	C (kPa)	tanϕ	k_d (cm^3/N-s)	τ_c (Pa)	Final side slope (V/H): measured vs. (model)	Measured data			Calculated results			
										Q_p (m^3/s)	B (m)	T_f (hr)	Q_p (m^3/s)	B (m)	T_p (hr)	T_f (hr)
25	4.1	7	0.244		20	1.0	8.74	0.15	(vertical)	171			151.95/ 119.97	10.78/ 7.42	0.401/ 0.407	
26	14.0	0.2	0.35[a]		9[a]	0.6[a]			1.05(1.09)	4160	96.0	1.0	4853.49	101.54	0.717	1.319
27	22[a]	50[a]	0.21[a]		2[a]	1.0[a]			(1.22)	1150		0.75	1287.33	35.92	0.0	1.116
28	6[a]	0.25	0.3[a]		3[a]	0.65[a]			1.04(1.06)	510	29.57		584.69	38.13	0.260	0.600
29	53.0[a]	50[a]	0.2[a]		2.7[a]	0.9[a]			1.04(1.04)	7360	175.1	5	7065.45	138.91	0.752	2.435
30	13.0	0.005	0.3[a]		60[a]	0.6[a]	5.35	0.15	2.27(2.17)	6850	91.5	2.5	8155.94	80.57	1.904	2.160
31	25.0	0.03[a]	0.3[a]		60[a]	0.7[a]	5.35	0.15	3.2(3.21)	1130	23	1.3	1347.96	22.50	0.535	1.229
32	5.0[a]	0.03[a]	0.35[a]		18[a]	0.55[a]	9.2	0.15	4.76(4.65)		13.6		46.308	13.53	3.792	6.689
33	11.0[a]	0.03[a]	0.3[a]		36[a]	0.55[a]	5.7	0.15	4(3.93)	510	21.34	7	556.94	21.83	4.193	8.567
34	11.5[a]	0.03[a]	0.3[a]		8.5[a]	0.55[a]	3.5	0.15	1.03(1.06)	929	41		817.25	47.24	5.099	7.728
35	4[a]	0.03[a]	0.3[a]		22[a]	0.55[a]	5.7	0.15	2(1.97)	1420	67		1537.62	56.35	3.211	6.665
36	6[a]	0.074	0.3[a]	0.18	4[a]	0.25[a]	3.0	0.15	0.41(0.40)	3080	180	3.0	3430.3	130.71	2.778	3.418
37	11.0[a]	0.03[a]	0.35[a]		7[a]	0.50[a]	12.0	0.15	1.0(0.96)		76.2		1033.72	75.42	2.539	4.989
38	4.0[a]	0.03[a]	0.3[a]		4[a]	0.45[a]	3.5	0.15	1(1.09)		13.4		28.74	13.69	3.005	5.221
39	11.5[a]	0.03[a]	0.35[a]		8[a]	0.5[a]	28.0	0.15	1.18(1.11)	680	35	0.5	564.83	34.05	0.019	0.469
40	13.0[a]	0.03[a]	0.3[a]		39[a]	0.55[a]	2.5	0.15	3.33(3.40)		58.8(av.)		949.01	57.88(av.)	19.60	34.960
41	4.0[a]	0.03[a]	0.35[a]		24[a]	0.55[a]	12.5	0.15	1.92(1.95)	2320		2.0	2268.39	52.77	0.742	1.885
42	14.0[a]	0.03[a]	0.35[a]		20.5[a]	0.55[a]	15.0	0.15	1.59 (1.54)		30.0	1.0	749.39	25.21	0.171	0.719
43	8.0[a]	0.03[a]	0.35[a]		4[a]	0.45[a]	8.5	0.15	0.847(0.849)	290	33.5(av.)	3.0	351.92	35.86(av.)	2.607	4.692
44	20[a]	0.03[a]	0.3[a]		25[a]	0.5[a]	5.35	0.15	1.33(1.30)	1330	49.9		1504.71	39.09	0.363	1.528
45	4.5[a]	0.03[a]	0.35[a]		15[a]	0.5[a]	5.5	0.15	(2.32)	340			345.30	35.34	4.492	8.555
46	10.0[a]	0.03[a]	0.35[a]		3.5[a]	0.4[a]	5.3	0.15	0.667(0.666)	1800	67(av.)		1801.48	68.24(av.)	3.665	6.804
47	7.0[a]	0.03[a]	0.35[a]		7.5[a]	0.5[a]	7.2	0.15	1.30(1.29)		19.0		53.22	12.45	0.136	0.314
48	16.0[a]	0.03[a]	0.35[a]		29[a]	0.55[a]	15.0	0.15	2(2.01)		30.5		692.88	30.65	0.135	4.007
49	5[a]	0.3[a]	0.35[a]		4[a]	0.45[a]	20.0	0.15	1(0.99)		20.0		115.34	20.18	0.111	0.423
50	45[a]	0.03[a]	0.3[a]		25	0.65	8.0	0.15	1(0.98)	65120	151(av.)	4.0	64272.7	138.83(av.)	1.455	5.333

6.5. Overall Statistics of Model Performance

The overall performance of the model in the 50 cases tested above was assessed by comparing the measured and calculated peak discharges, breach widths, times to peak discharge, and failure times whenever the measured data are available, as shown in Figs. 6.7–6.9. Fig. 6.7 includes 42 data points, which means that 42 out of the 50 cases have peak discharge measurement data. For 92.9% of the cases (39 out of the 42 cases), the calculated peak discharge values deviate within ±25% from the measured values. This agreement is very encouraging. Fig. 6.8 includes 43 points or cases, in which the final breach top width or average width is used if available. For 76.7% of the 43 cases, the calculated breach widths are within ±25% from the measured values. Fig. 6.9 contains 32 data points of peak discharge time or failure time. Considering most cases have the measured values of only either the time to peak discharge or failure time, all the available characteristic times are plotted together in Fig. 6.9, termed as "breach time". For 62.5% of the 32 points, the calculated times to peak breach discharge or failure times deviate within ±25% from the corresponding measured values.

To further quantify the model performance, the root-mean-square relative error, E_{rms}, is defined as

$$E_{rms} = \sqrt{\frac{1}{N}\sum_{i=1}^{N}\left(1-\frac{\text{Calculated}}{\text{Measured}}\right)^2} \tag{6.1}$$

where N is the number of the data points. The root-mean-square relative error is 14.5%, 16.5% and 34.1% for the peak breach discharges, breach widths and times in Figs. 6.7–6.9, respectively. In addition, the correlation coefficient R^2 is 0.997, 0.970, and 0.939 for peak breach discharges, breach widths and times, respectively. The model shows higher errors for the breach time than the peak discharge and breach width. This is due to the breach time is more difficult to measure and model. Overall, the model performs encouragingly well.

Note that the above model performance statistics have uncertainties because several parameters, such as the initial breach dimensions, soil cohesion, friction angle, porosity and erosion coefficient have to be assumed or estimated in many field cases. It is found that the initial breach dimensions do not significantly affect the peak discharge and final breach width, but are important for the calculated failure time. A smaller initial breach channel will take longer time to fully develop to a failure.

The erosion coefficient k_d is found to be the most important parameter in cases where cohesive sediments are dominant. Table 6.10 summarizes the k_d values used in the thirty-five test cases with cohesive sediments. k_d was measured in only two cases, and calibrated in the other thirty-three cases. The typical k_d values for the thirty five cases are within 2.5-28 cm^3/N-s. for 62.9% of the 35 cases, the typical k_d values are within 5-10 cm^3/N-s. Compared with the k_d

values reported in literature, this range of values is relatively narrow. More testing is needed to validate this.

Table 6.10. Values of Erosion Coefficient k_d

k_d range (cm^3/N-s)	No. of cases within k_d range	% within k_d range
2.5-5	4	11.4%
5-10	22	62.9%
10-20	8	22.8%
20-30	1	2.9%

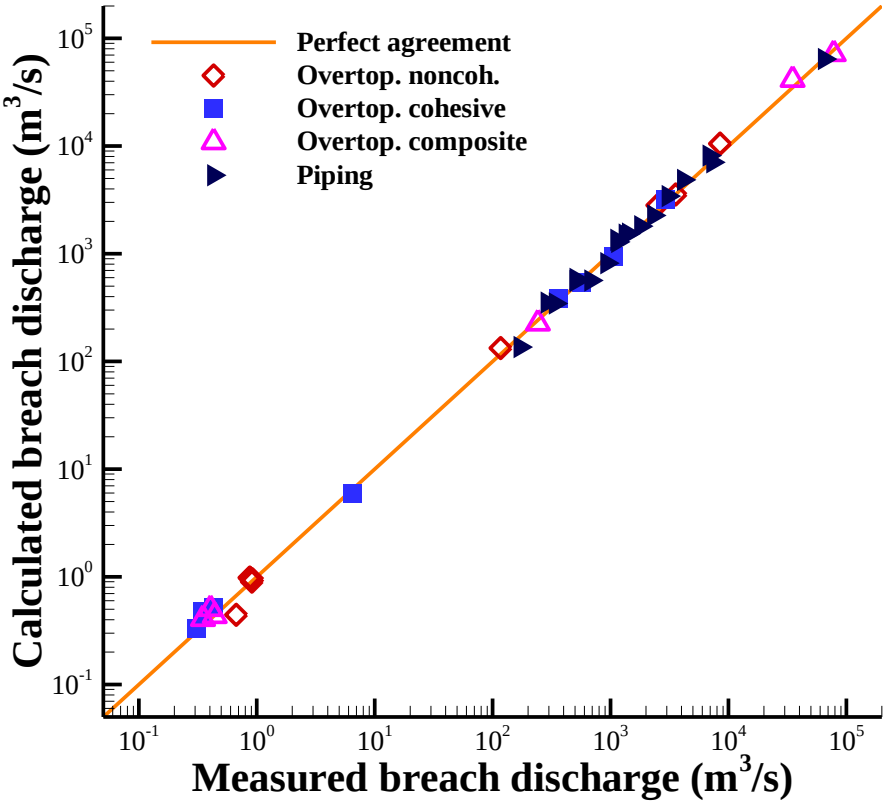

Fig. 6.7. Measured vs. calculated peak outflow discharges of all test cases

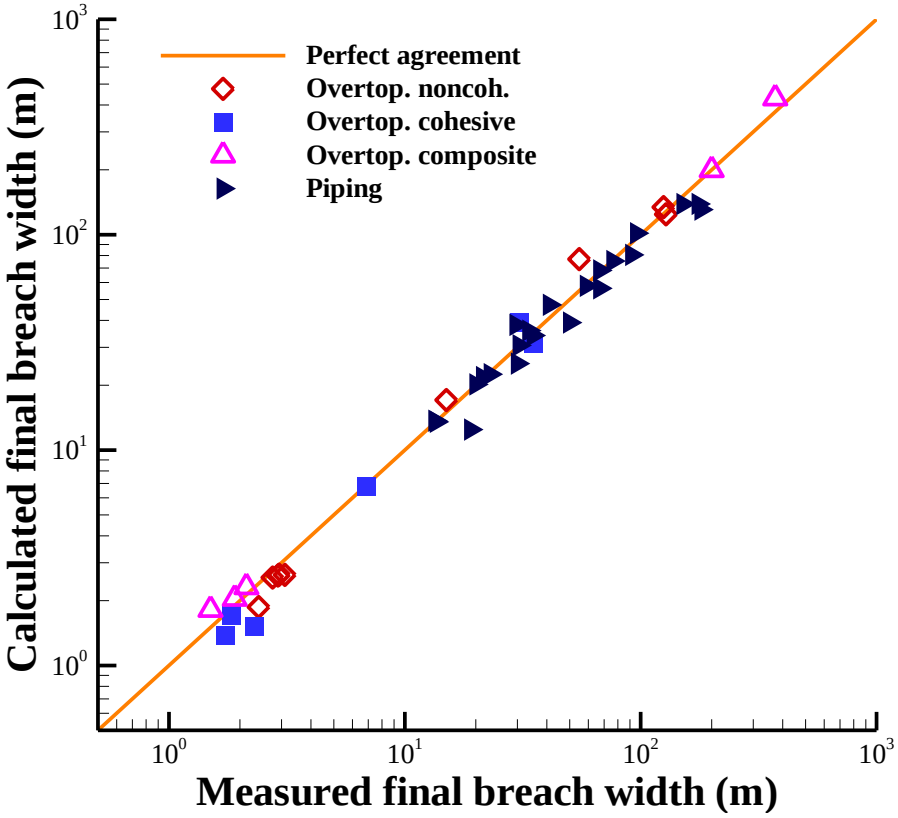

Fig. 6.8. Measured vs. calculated breach widths of all test cases

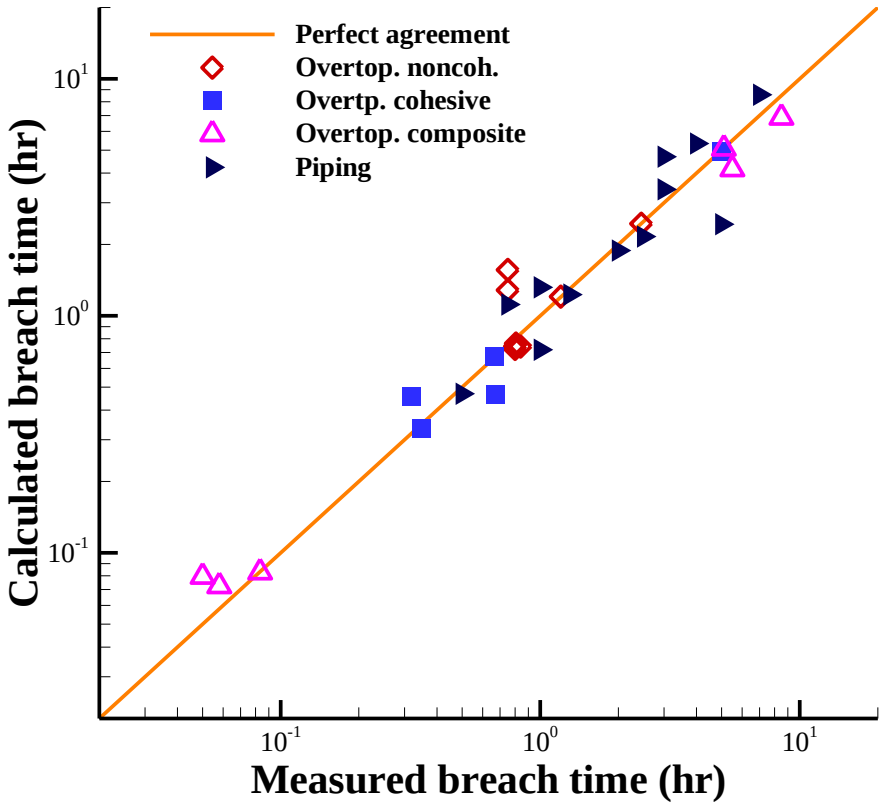

Fig. 6.9. Measured vs. calculated breach characteristic times of all test cases

Chapter 7. Model Testing in Cases of Levee and Barrier Breach

The model has been tested using two cases of coastal dike and barrier breaching and two cases of inland levee breaching. They are the 94' field experiment of sea dike breach in the Zwin Channel Estuary reported by Visser (1998), the Mecox Inlet breaching and closure occurred in Sept. 10-18, 1985 monitored by Smith and Zarillo (1988), the Yahekou Fuse Plug Dam breach experiment, and the 1997 Sutter Bypass Levee breaching. The four test cases are described in this chapter.

7.1. Dike Breach in Zwin Channel Estuary

The developed model was tested using the Zwin'94 field experiment of sea dike breaching conducted at the Zwin Channel Estuary near the Dutch-Belgian border. The Zwin channel connects the nature reserve "Het Zwin" with the North Sea. At high water, the width of the mouth is about 150 m. The reserve surface area is about 1.5 km^2, consisting largely of marshes and gullies (Visser, 1998). A sand dike was built across the Zwin Channel, as shown in Fig. 7.1. Its crest was 3.3 m above the mean sea level (NAP). The seaward side and bay side slopes were 1:1.6 and 1:3, respectively. The crest was about 8.0 m wide. The bottom elevation of the Zwin Channel near the sand dike varied between 0.5 and 0.9 m, with an average of 0.7 m above the mean sea level. The dike sediments consisted of 'original' Zwin sand with a median diameter of 0.185 mm and additional sand with a median diameter of 0.315 mm transported alongshore from the Belgium coast. The initial breach was 0.8 m deep, about 1.0 m wide near its bottom or 3.6 m wide near the crest of the dike (Fig. 7.2). The tidal level outside the dike was measured during the breaching, and the highest water level was 0.27 m above the initial breach bottom (2.77 m above NAP). The experiment was conducted in quiet autumn weather with wind speed of about 2 m/s and negligible wave height against the sand dike (Visser, 1998).

The simulation considered a sand dike with the same geometry and material as used in the experiment. Because the topography in the polder area was not clear, the flow routing in the bay area was not conducted. Instead, the model simulated the breaching by imposing the measured water surface elevations on the sea and bay sides. The water levels were measured on Stations MS-1 through MS-5, whose locations are marked in Fig. 7.1, and the measured values are plotted in Fig. 7.3. The stations MS-1, 2 and 3 were on the sea side, and stations MS-4 and 5 were on the bay side. The breach occurred from the sea side due to elevated tide. The water levels on MS-1, 2 and 3 exhibit some disturbance by the breach flow, and thus they are not the exact tide level on the seaside. The tide level on the seaside was reconstructed by using a cosine wave with the maximum tide level of 2.77 m and a tide period of 12 hours, as shown by the solid line in Fig. 7.4. Compared with the measured water level at MS-1, the reconstructed tide level is higher during the breaching phase.

On the bayside or landside, the water levels measured at MS-4 and 5 exhibit difference in the first 30 minutes, but agree with each other afterwards. This indicates the water levels were affected by the breach outflow in the beginning period. The water level in the bay was reconstructed by replacing the water level in the first 30 minutes by a linear variation. Considering in the beginning period the breach flow might be mostly supercritical, the downstream water level in the bay did not affect the breach flow significantly. Therefore, the possible errors in the reconstructed bay water levels in the beginning period might be ignored.

The dike consisted of local sediments with a median diameter 0.185 mm and supplement sediments with a median diameter of about 0.315 mm transported from nearby shores. Considering the local sediments played a more important role, particularly in the bottom portion of the dike, the sediment diameter of 0.185 mm was used as the representative diameter in the simulation. A smaller representative diameter was chosen also because the newly constructed sand dike might not be compacted as much as the local sediment in the dike base. The sediment porosity was set as 0.45. The sediment was considered noncohesive. The internal friction was assumed 29^{o}. The non-equilibrium adaptation length of sediment was calibrated as $2.4B$, in which B is the breach channel width at the water surface. This value is slightly lower than the recommended range of $(3\text{-}6)B$. The Manning roughness coefficient n of the breach channel was set as 0.018.

Fig. 7.5 compares the calculated and measured breach top widths in the Zwin case. The breach growth trend was generally reproduced by the model. The calculated maximum breach top width is 39.2 m, which is in a good agreement with the measured value of 41.0 m. The model predictions are somehow off around the elapsed time of 10 minutes. The reason is that the flat top usually erodes slower and has a narrower channel width than the downstream slope segment. Around 10 minutes, the flat top was eroded away and the downstream slope took over, so the breach width increased rapidly then. The simulation shows that the breach was almost completed in about 40 minutes, whereas the experiment shows that the breach continued growing in a small rate.

Fig. 7.6 compares the calculated and measured velocities in the breach. The calculated velocities are cross-sectional average, while the measured velocities were obtained at the breach and MS-5 by floating markers on the water surface. Even with this difference, the values of measured and calculated velocities agree encouragingly. The velocities measured at MS-5 are slightly smaller than those measured at the breach, and are included in the figure as a reference. The calculated values agree well with the measured breach velocity at the beginning and with the MS-5's data in the tailing part.

The dike was built on the original erodible channel bed, so the dike subbase erosion occurred as observed in the experiment. In the experiment, vibration probes were used to measure the erosion depth, and three time slots of the longitudinal section along the breach axis were obtained, as shown in Fig. 7.7. We derived the averaged breach bottom elevations in these three time slots using the values on the three vibration probes just above the downstream

(bayside) toe of the dike. The measured average scour depth is about 2.05 m (the maximum about 2.3 m) at the time of 24 minutes. The three measurement data are shown in Fig. 7.8. The model simulation did not limit the subbase erosion (by setting the base erosion limit to a value much larger than the final erosion depth). The calculated breach bottom elevation agrees well with the three measurement data. Because the vibration probes were set within 3 m below the dike baseline, no measurement data of bottom elevation are available after the elapsed time of 24 min. However, the model predicted a scour hole of 3.72 m in depth. Compared with the dike height of 2.6 m, the scour hole is quite deep and cannot be ignored in the breach modeling.

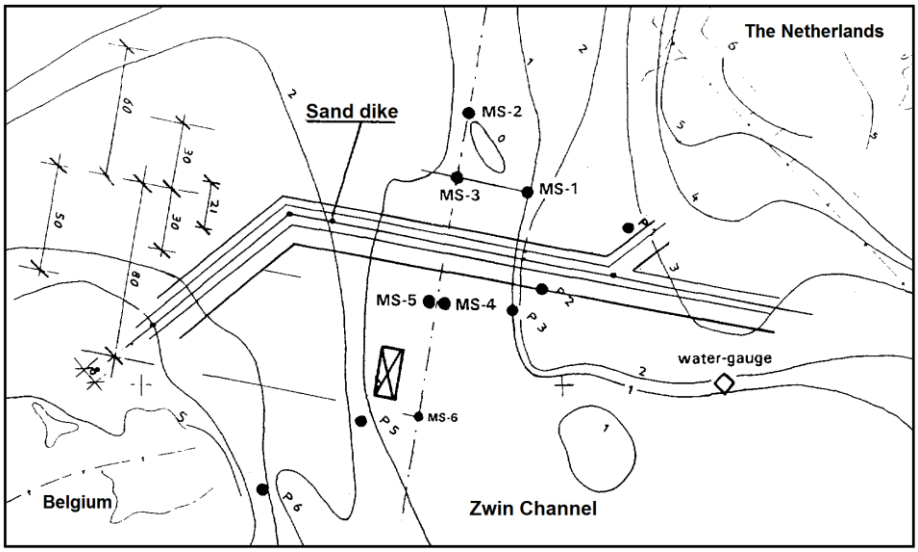

Fig. 7.1 Plan View of the Dike Constructed in the Zwin Channel Estuary (Visser, 1998)

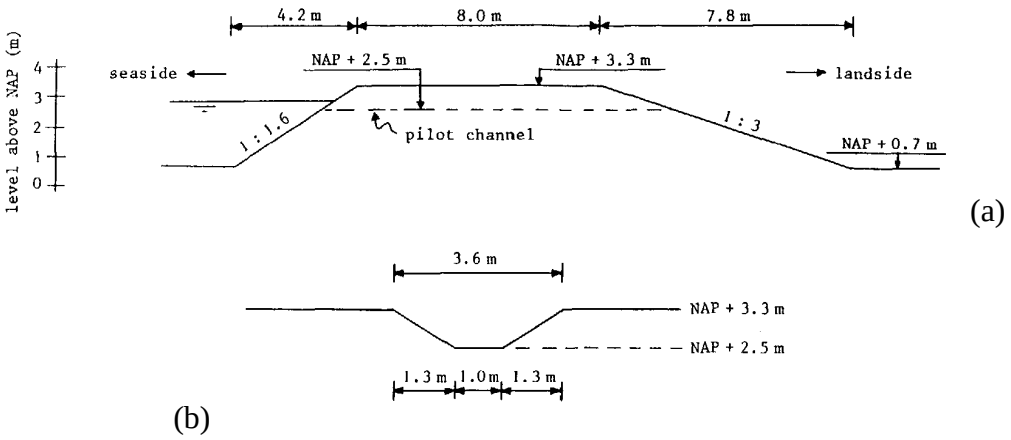

Fig. 7.2 Dike Constructed in the Zwin Channel Estuary: (a) Cross-Section of the Dike; (b) Cross-Section of the Pilot Breach (Visser, 1998)

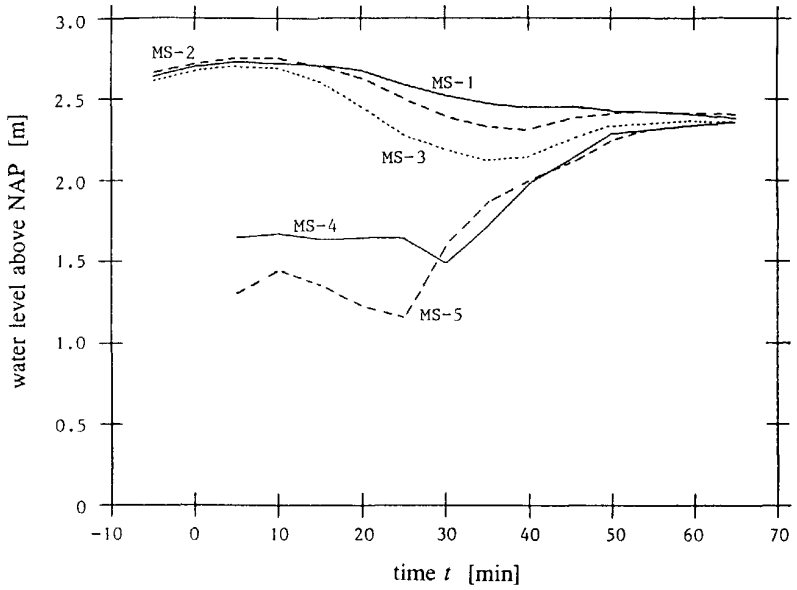

Fig. 7.3 Water Levels Measured at MS-1 through MS-5 (Visser, 1998)

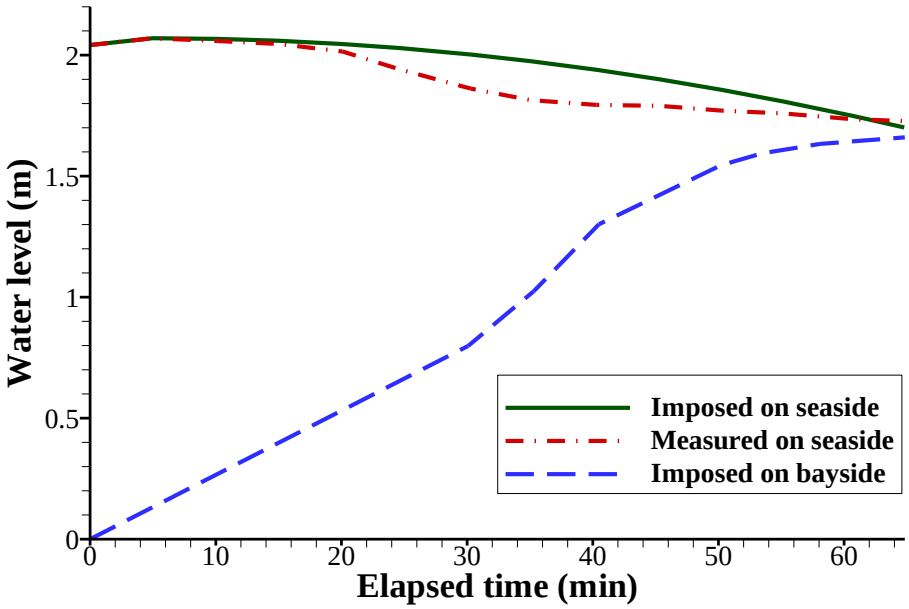

Fig. 7.4 Water Levels Imposed on Seas and Bay Sides in the Zwin Case

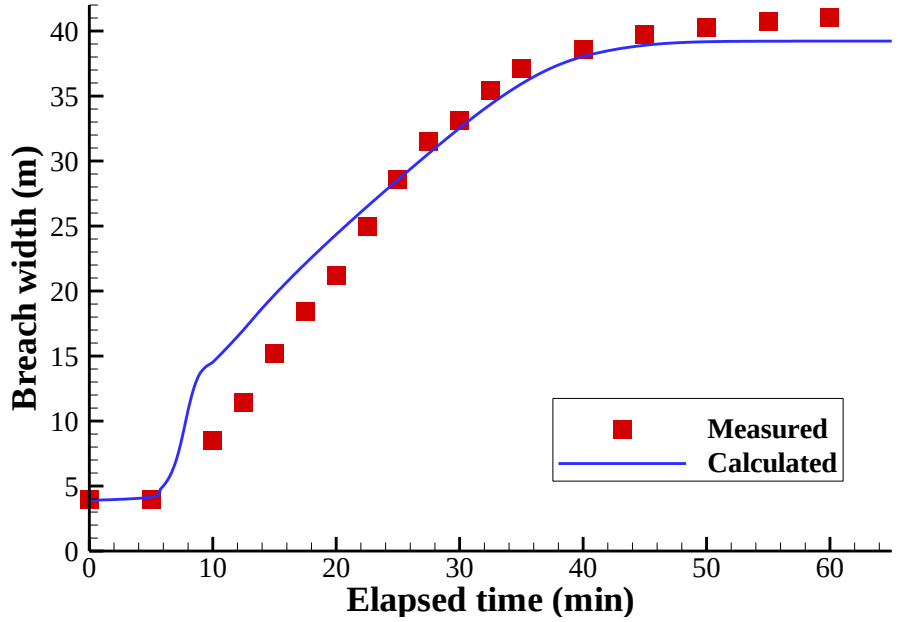

Fig. 7.5 Comparison of Calculated and Measured Breach Top Widths in the Zwin Case

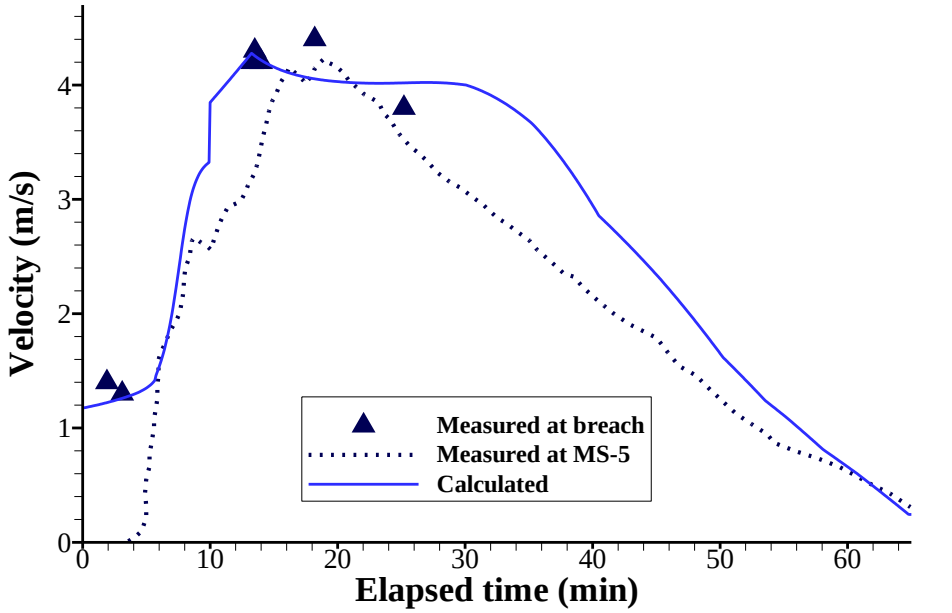

Fig. 7.6 Comparison of Calculated and Measured Breach Velocities in the Zwin Case

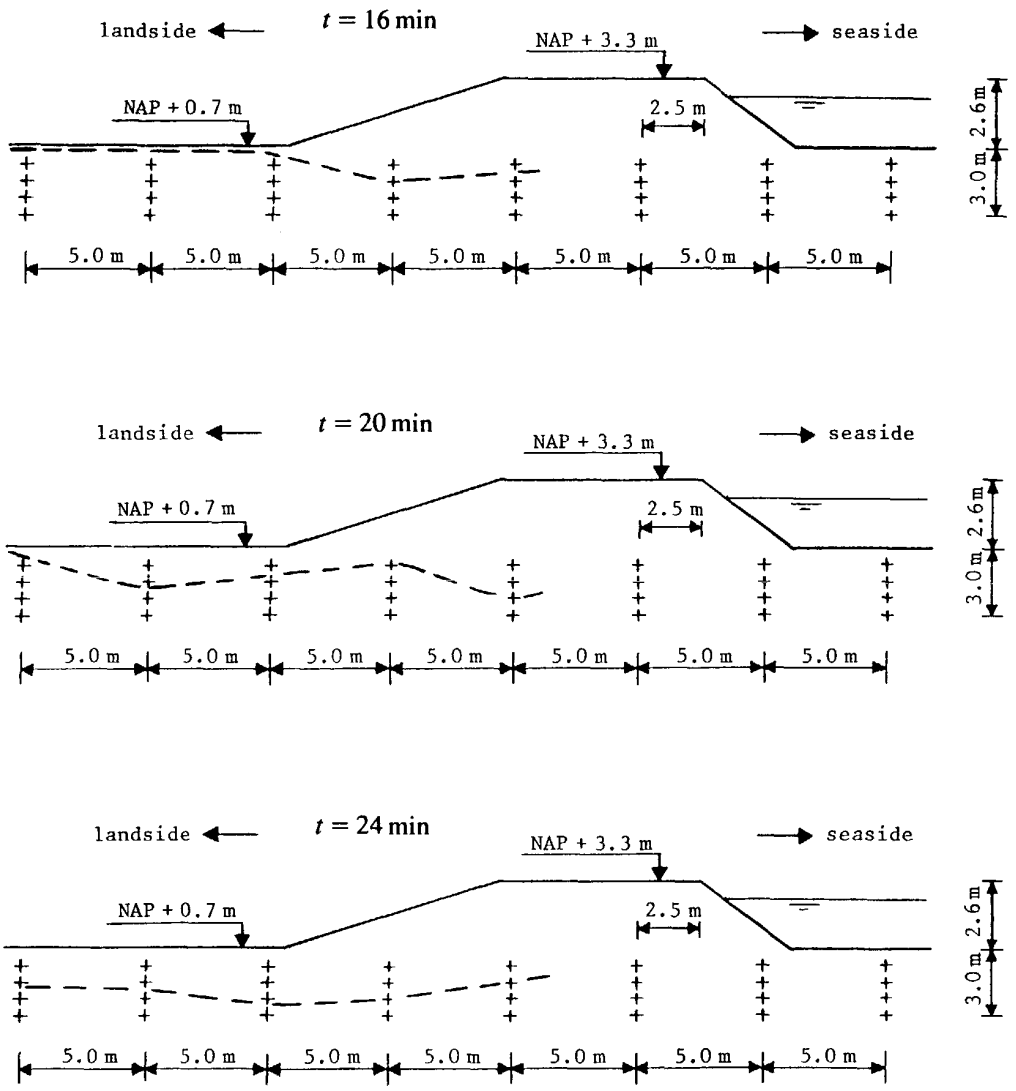

Fig. 7.7 Development of Scour Hole in the Breach-Axis Measured in the Zwin Case: (dashed lines for scour hole; + indicates the locations of vibration probes) (Visser, 1998)

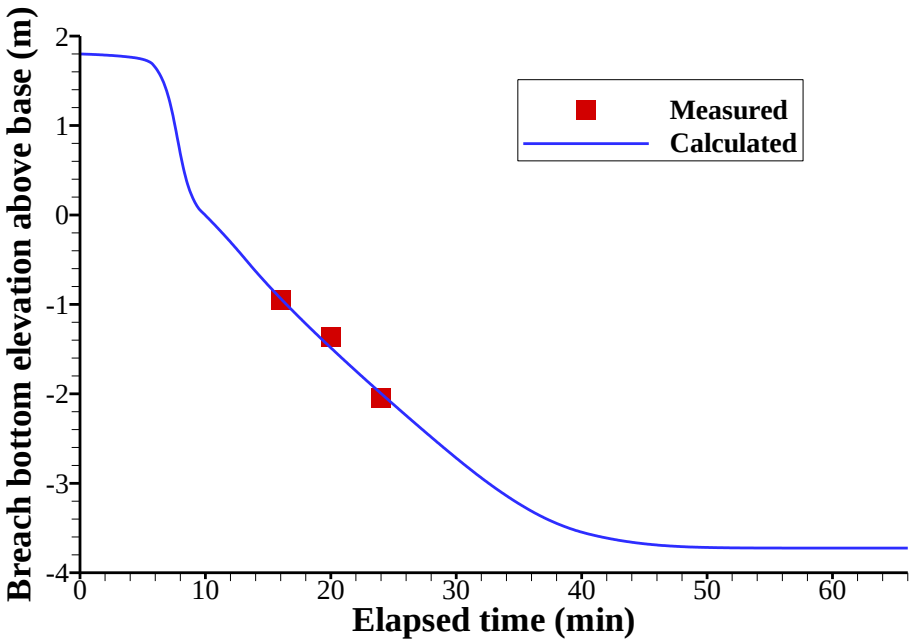

Fig. 7.8 Comparison of Calculated and Measured Breach Bottom Elevations in the Zwin Case

7.2. Breaching and Closure of Mecox Inlet, NY

Mecox Bay is located on the south shore of eastern Long Island, New York (Fig. 7.9). The bay is approximately 4 km^2 in area, and generally 1 to 2 m deep. It is separated from the Atlantic Ocean by a 400 m wide barrier beach. Mecox Inlet is an ephemeral inlet. The inlet has been periodically opened to lower the water level and flush the bay, artificially about seven times per year and naturally about once a year via barrier breaching by storm. Regardless of the manner by which it is opened, Mecox Inlet has closed naturally within 1 to 2 weeks (Smith and Zarillo, 1988).

Mecox Inlet was opened manually in Sept. 10, 1985 and closed naturally in Sept. 18, 1985. Smith and Zarillo (1988) monitored and reported the inlet evolution in this period. The measurement data are used to test the present model. Fig. 7.10 shows the plan view of Mecox Inlet and the locations of measurement devices. Fig. 7.11 shows the measured water levels on the bay and sea sides. One can see that in most of the time the bay water level was higher than the sea water level. The bay water level decreased due to the inlet opening and experienced slight effect of tides. Fig. 7.12 shows the measured wave heights during the eight days of measurement. In the first four days the significant wave height was about 0.4 m, and in the remaining days the wave height increased significantly.

The wind velocity was measured at 1.5 m above the ground. An offshore wind of about 16 m/s was found in the first two days, and then the wind changed direction and became less

important for the breaching process. The wind speed of 16 m/s at 1.5 m above the ground is converted to a 22 m/s at 10 m above the ground, which is used in the model. This conversion is based on a wind velocity profile of power law with an exponent of 1/6.

Figs. 7.13 and 7.14 show the daily inlet evolution process described by Smith and Zarillo (1988). One can see that the inlet reached the maximum width in day 1, then shrank gradually and closed between day 7 and 8. The inlet closure was due to deposition of the sediment transported from the east beach.

Even though the measurement data in this case are quite comprehensive, there are still some parameters that need to be estimated. The barrier is about 400 m, whereas in the inlet location it is about 230 m during the measurement period, as shown in Fig. 7.10. The beach slopes on both sides of the barrier are not known. Therefore, the bayward beach slope is assumed 1/40 and the seaward beach slope is 1/15, according to the general knowledge of the barrier in this area. The barrier is assumed 2 m high, and its top is 1 m above the mean sea level. This means the barrier bottom is 1 m below the sea level. The barrier foundation is not allowed to erode in the model simulation because no significant subbase erosion was observed in the measurement. The initial breach was 1 m deep and 5 m wide according to Smith and Zarillo (1988).

The representative sediment diameter is set as 0.5 mm, by referring to a study of Sanchez and Wu (2011) at Shinnecock Inlet, which is about 9 km western from Mecox Inlet. The sediment porosity is assumed 0.45, and internal friction angle is 29^o. The non-equilibrium adaptation length is set as $3B$. The Manning's roughness coefficient is set as 0.036 because of the large-scale bars and spit in and near the inlet. The longshore sediment transport is calculated by using the formula of Kamphuis (2002) with a scaling factor of 1.135. This scaling factor is multiplied to Eq. (4.34) for the longshore transport rate. The value of 1.135 is calibrated by comparing the inlet closure time. A larger scaling factor leads to a quicker inlet closure.

The wind fetch (distance of tide gages to the inlet) is about 500 and 400 m on the bay and sea sides, respectively. Considering the geometry near the inlet, the effective fetch is set as 750 and 400 m on the bay and sea sides, respectively. This means that the correction factor λ_w is 1.5 and 1.0 on the bay and sea sides, respectively. The coefficient α_w in Eq. (3.26) for wave setup is set as 0.45. This value is relatively large, compared to the literature values (Dean and Walton, 2010). This value is used by comparing the calculated and measured bay water levels. It is found that the wave setup is a significant portion of sea water level to maintain the bay water level, since the sea water level is significantly lower than the bay water level in most of the time during the study period as shown in Fig. 7.11.

Considering the water surface area in the bay and its tributaries might have uncertainties, two simulation scenarios are considered. The first scenario imposes the measured water levels (Fig. 7.11) on the two sides of the inlet. This approach can avoid the uncertainties inherited from the unknown topography in the bay basin and focus only on the inlet evolution. The second scenario imposes the measured sea water level (Fig. 7.11) and assumes the bay surface area, A_w, as a function of bay depth, h, (above the dike base) (Wu, 2013, 2015):

$$A_w = \alpha h^m \tag{3.1}$$

where α is set as 4000000.0, and exponent m is 2.5. These parameters give a bay surface area of 4 km^2 at the sea level. The exponent m is between 1 and 3 according to Wu (2013, 2015). The present value of 2.5 is within this range.

Fig. 7.15 shows the comparison of calculated and measured inlet cross-section areas. The measured values are the average area between flood and ebb tides. The calculated is the time-varying flow area at the inlet for the first scenario by imposing the water levels on both sides of the inlet. The inlet cross-sectional area increases rapidly in the first day when the breaching process dominates. Then the area maintains around the maximum level until day 4 when the waves become strong. During day 4 and 8, the inlet shrinks due to the increased longshore sediment deposition at the inlet. The inlet is closed between day 7 and 8. The calculated results of cross-sectional flow area are very encouraging and agree well with the measured data in magnitude.

Fig. 7.16 shows the comparison of calculated and measured flow velocities in the inlet. The calculated values are the cross-sectional average for the first scenario, where the measured values are the surface velocities based on floating markers in a reach of about 20 m. The model predicts well the velocity in the first one and half days, slightly overpredicts during day 2 and 5, and significantly underpredicts during day 6 and 7. It is not clear why the measured velocities became larger even though the inlet was shrinking. This might be related to the strong waves, which make the surface velocity measurement more difficult. In general, the simulation and measurement are in good agreement.

Figs. 7.17 and 7.18 compare the calculated inlet flow areas and velocities of the first and second scenarios against the measured data. Both scenarios give similar trends, the cross-sectional area in the second scenario is larger, while the velocities of both scenarios are very close.

Fig. 7.19 compares the calculated bay water levels of the second scenario against the measured data. The model predicts lower bay levels than the measurement for day 2 to 5, but the bay water level regains a little after day 6. The general trend of the bay water level drawdown is obtained by the model, but the time of lowest bay water level is not. Because the time of lowest water level is also related to the bay topography, climate and meteorological conditions, it is difficult to resolve this mismatch without information on these conditions.

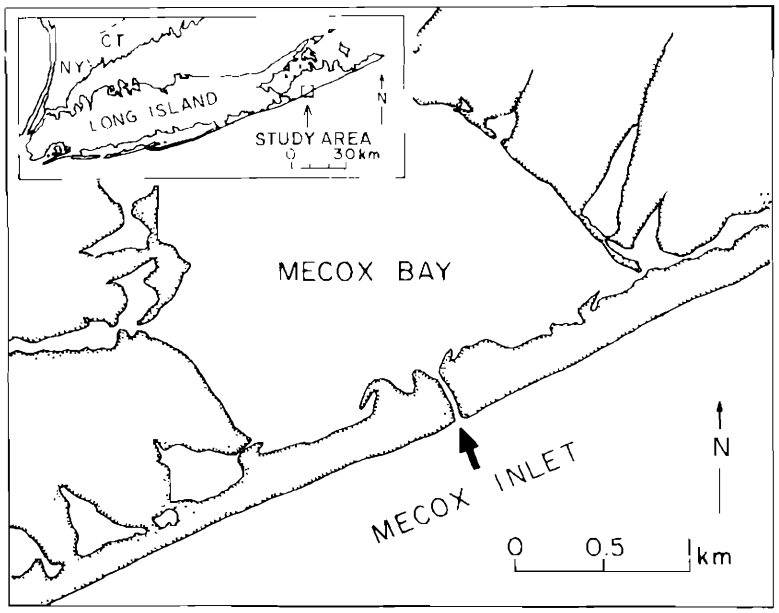

Fig. 7.9 Map of Study Area: Mecox Inlet, NY (Smith and Zarillo, 1988)

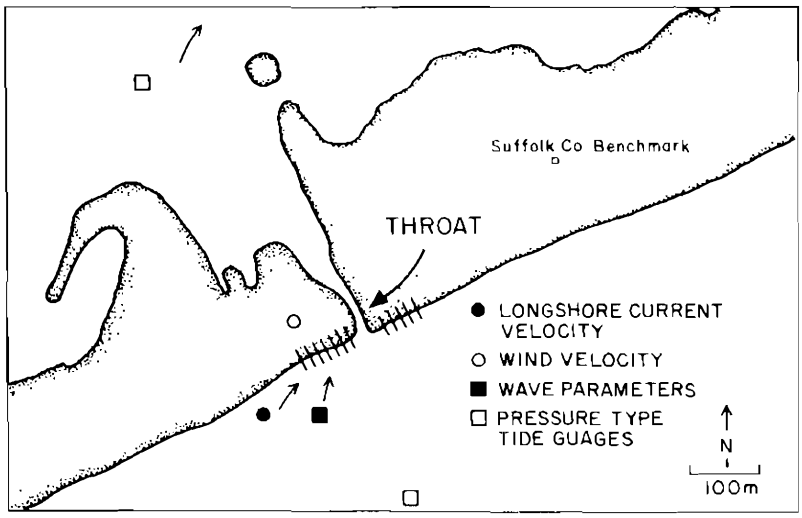

Fig. 7.10 Plan View of Mecox Inlet and Locations of Measurement Devices (Smith and Zarillo, 1988)

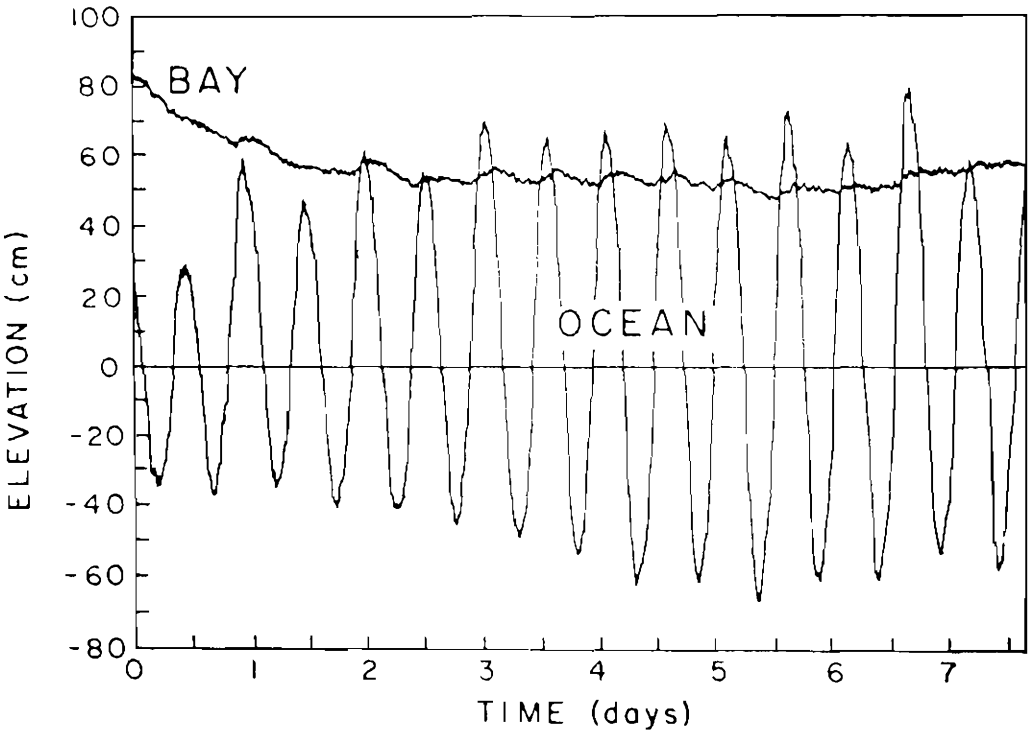

Fig. 7.11 Water Levels Measured on Bay and Sea Sides (Smith and Zarillo, 1988)

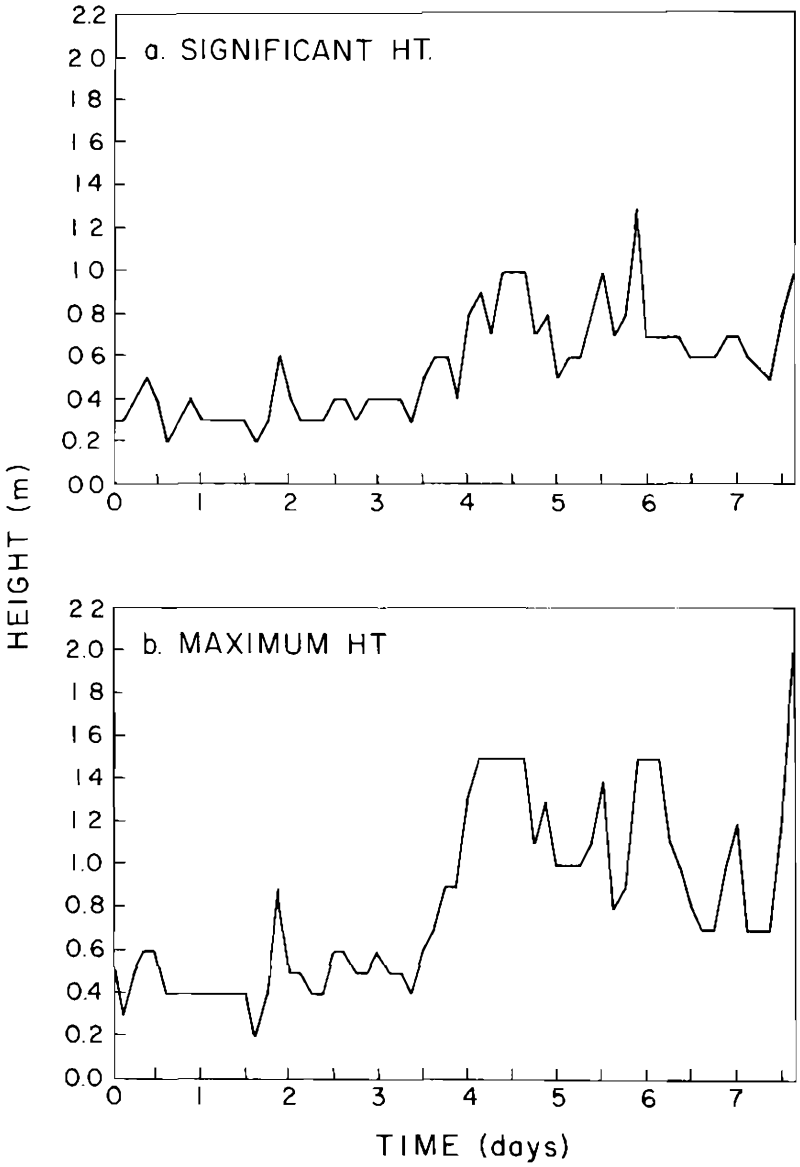

Fig. 7.12 Wave Heights on the Seaside (Smith and Zarillo, 1988)

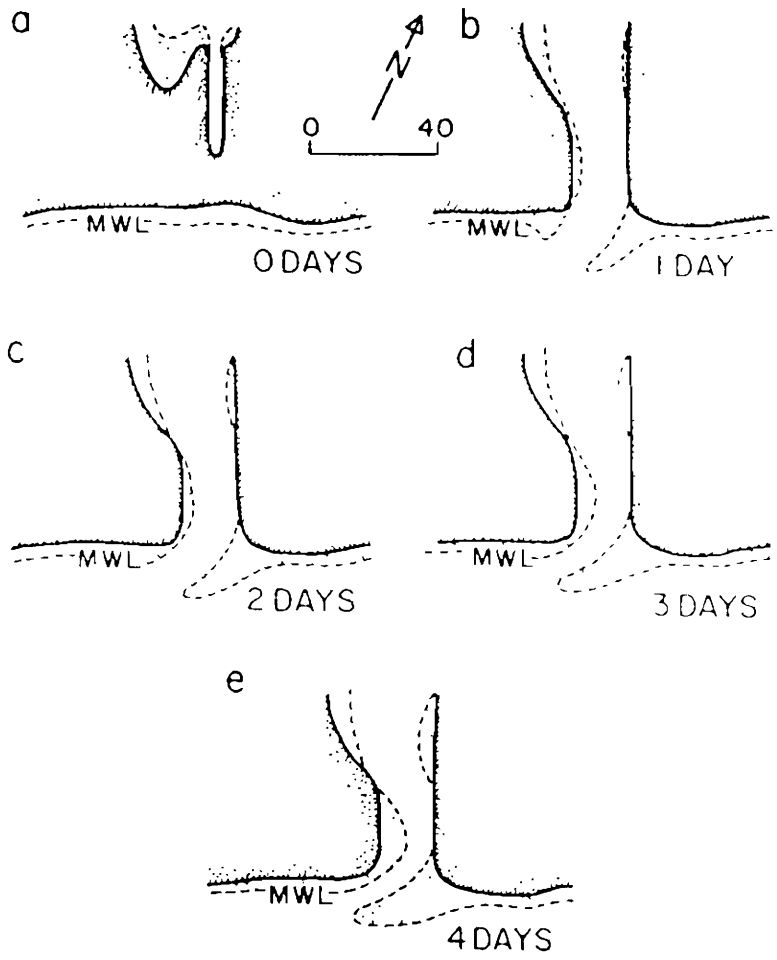

Fig. 7.13 Morphology of the Mecox Inlet during the First Four Days (Smith and Zarillo, 1988)

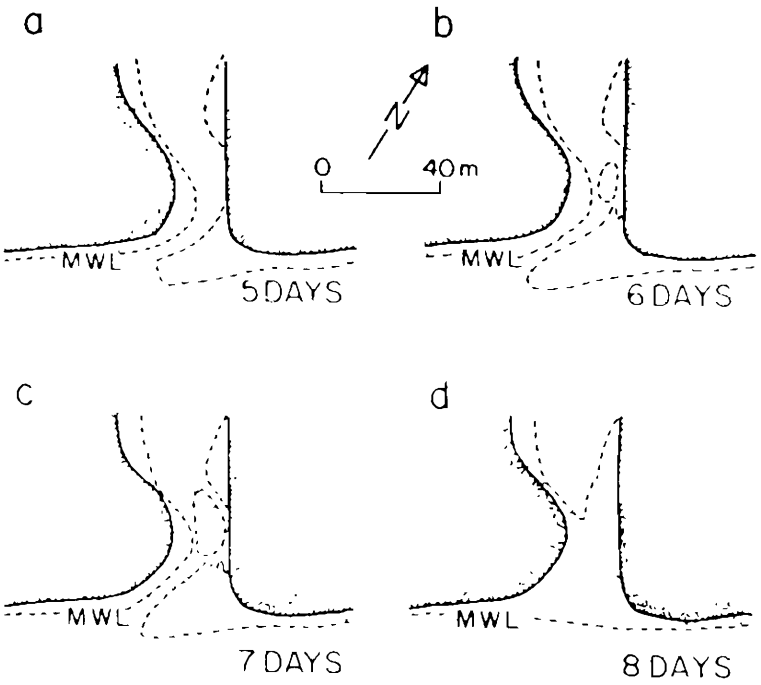

Fig. 7.14 Morphology of the Mecox Inlet during the Last Four Days (Smith and Zarillo, 1988)

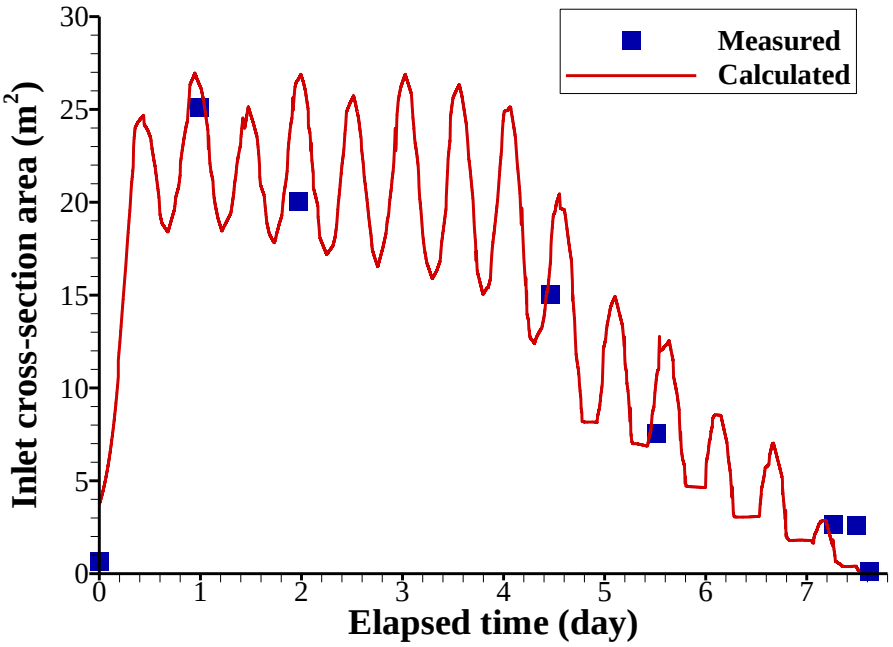

Fig. 7.15 Comparison of Calculated and Measured Inlet Flow Cross-Section Areas in the Mecox Case

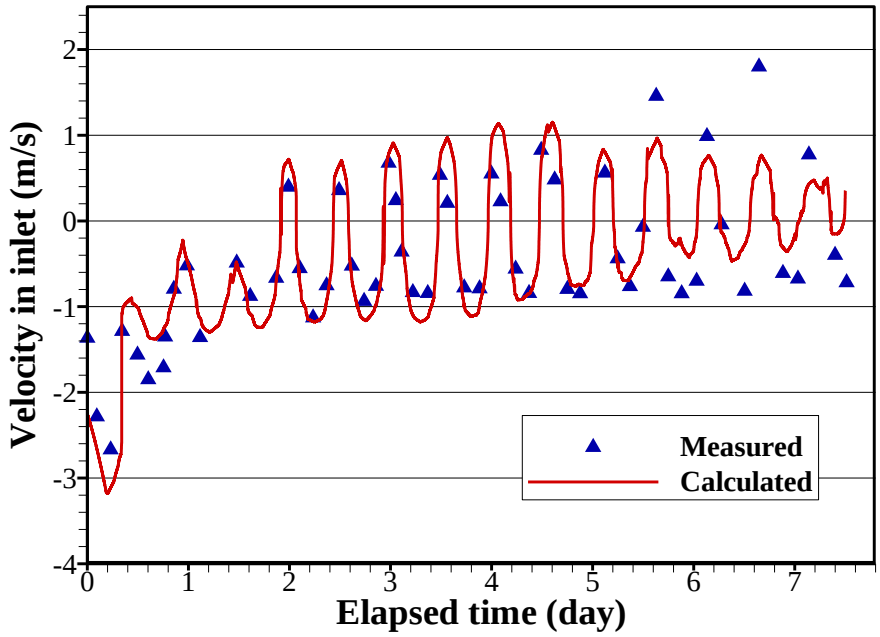

Fig. 7.16 Comparison of Calculated and Measured Inlet Flow Velocities in the Mecox Case

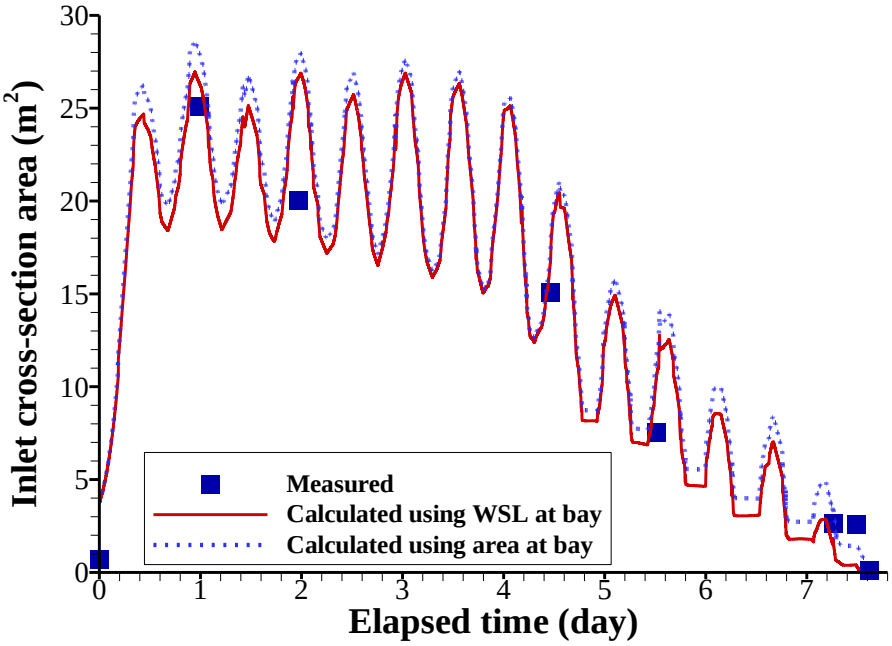

Fig. 7.17 Comparison of Measured Inlet Cross-Section Areas against Those Calculated by Specifying Bay Area or Water Surface Level (WSL)

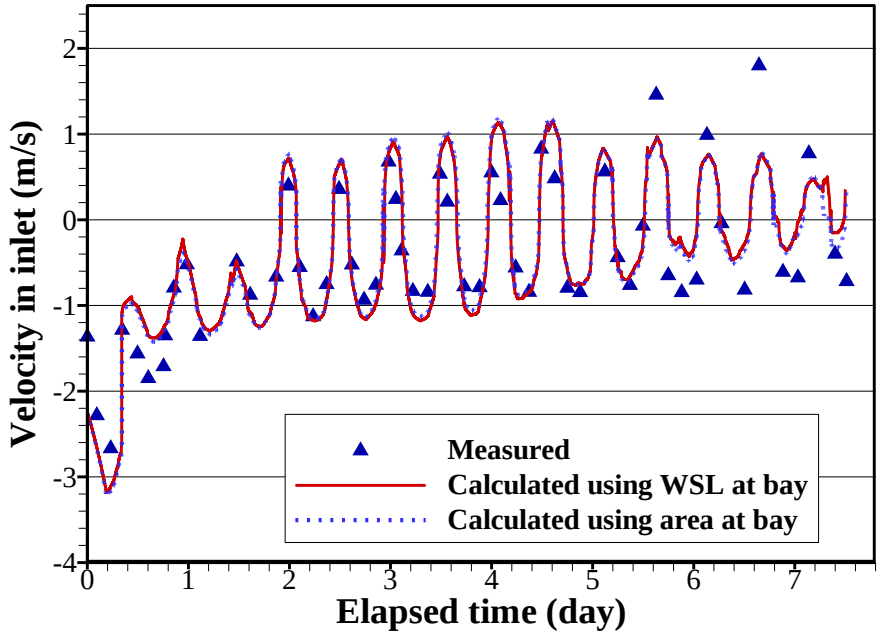

Fig. 7.18 Comparison of Measured Inlet Velocities against Those Calculated by Specifying Bay Area or Water Surface Level (WSL)

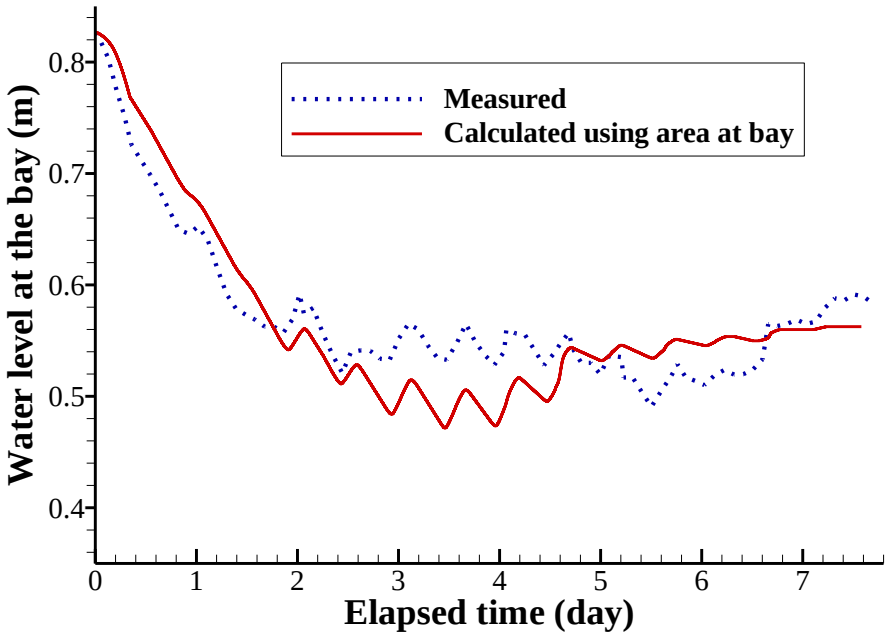

Fig. 7.19 Comparison of Measured Water Levels of the Mecox Bay against Those Calculated by Specifying Bay Area

7.3. Yahekou Fuse Plug Dam Breach

A fuse plug dam breach test was conducted on March 18, 1982 in the spillway chute of the main dam of the Yahekou Reservoir, Henan, China (Pan et al., 1993). This dam breach case can be used as a levee breach example because it exhibited typical levee breach features and the water levels upstream and downstream of the test dam were measured.

The test fuse plug dam was a sand fill dam with a clay core and a clay cover on the downstream surface. The plan view and cross-section of the test dam are shown in Figs. 7.20 and 7.21, and the geometric properties of the dam body and clay core are shown in Table 7.1. The dam was 5.6 m high, 41 m long at the top and 31 m long at the bottom. It had a crest of 4 m wide and a reservoir with a capacity of 46,000 m^3. The reservoir was about 318 m long and 60 m wide. The test dam's upstream slope was 1:3.0 (vertical/horizontal) while the downstream slope was 1:2.5. The core was made of heavy loam. The core's top was 0.5 m lower than the dam crest. It was 0.8 m wide in its top (1.08 m on the site of pilot channel) and 2.5 m wide in the bottom. Both upstream and downstream slopes of the clay core were 1:0.17. The dam body was protected with block stone of 0.3 m at the upstream slope and heavy loam of 0.3 m thick at the downstream slope. A 1.3 m deep and 1.5 m wide pilot breach channel was made to initiate the breaching process.

Water levels were measured by gauges installed in front of the pilot channel, at the downstream toe of the dam and 56.8 m downstream from the dam axis. A mesh with a mesh size of 1.50×1.75 m was drawn on the downstream slope surface of the dam to measure the erosion process by using video tape recorder and cameras. A total of 577 electric contract probes were embedded in the core and dam shells, each of which was connected to a lamp on an analogue board on the dam body, to indicate the erosion process through the lamp on-off signals.

Two simulations are conducted. In the first simulation (denoted as "DS WSL"), the measured upstream and downstream water levels are imposed as boundary conditions for the breach model, as shown in Fig. 7.22. The second simulation, denoted as "DS channel", assumes uniform flow in the downstream channel, which is represented with a 40 m wide rectangular channel with a bed slope of 2% and a Manning's n of 0.03. Both simulations use the same model parameters, except the different tailwater conditions mentioned here.

The geometric and soil properties are set mostly as the measured values as shown in Tables 7.1 and 7.2. Noting that the measured median diameter of the sand is between 0.45 and 1.5 mm, and the value used in the simulation is 0.8 mm. The measured internal friction angle of the sand is between 29^o and 38^o, whereas the corresponding value used in the simulation is 29^o. The measured cohesion of the core soil is 23.5 kPa, whereas the core soil cohesion used in the simulation is 21.0 kPa. Slightly lower values for the sand internal friction angle and core soil cohesion are used to obtain slightly better agreement between the simulation and measurement.

This treatment may be reasonable because of possible variations of these parameters during the experiments in which the soils may be affected by increased moisture and pore pressure.

The Manning's n is set as 0.023 and 0.016 for the shoulder sand and core clay beds, respectively. For the non-cohesive sediment transport, the adaptation length is set as 3 times the breach channel width at the water surface. For the core and cover soil erosion, the erodibility coefficient k_d is set as 3.9 $cm^3/N \cdot s$ and the critical shear stress for erosion τ_c is set as 0.15 Pa.

The experiment showed that the breach could erode on both the left and right sides in the first about 23 minutes, but afterwards the breach met a non-erodible spillway wall on the left bank. This means the breach was two-sided in the first 23 minutes and became one-sided in the remaining time. On the other hand, the reservoir of the dam is small compared to the inflow volume. The revoir capacity was 46,000 m^3, while the total water volume through the breach was about 470,000 m^3 according to the simulations. This means that this breach case is controlled by the upstream inflow, not the reservoir water. It has more levee breach features. As shown in Fig. 7.20, the test dam was constructed in the chute of the spillway and located at the downstream of a bend. After the initial stage of the breaching when the reservoir water was depleted and the breach eroded to the dam bottom, the flow in the chute and through the reach was a type of open channel flow over a steep bed slope. The flow out of the bend would hit the right side of the dam and the breach, causing more intense erosion on the right bank of the breach than a normal dam breach. Considering these special features, a two-sided breach is assumed in the entire breach period, i.e., the parameter n_{loc} in Eq. (4.16) is set 2.0 all the time in this case.

In addition, the broad-crested weir flow does not work well after this initial stage of breach when the common channel flow features became significant. Therefore, the breach period is divided into two stages: in the initial stage of about 23 minutes the weir flow equation is used to determine the breach flow, and in the remaining time the Keulegan equation is used to determine the breach flow. For the Keulegan equation, the local head loss coefficient at the breach entrance is set as 0.18, which is much smaller than 1.0 used for general levee breach flow. A smaller head loss coefficient at the breach entrance represents the fast channel flow features in the upstream in this case as mentioned above.

The calculated breach flow discharges and breach widths are compared with the measurements in Figs. 7.23 and 7.24, respectively. The calculated breach flow discharges and breach widths generally increase with time, agreeing well with the measured data. Again, this implies the breach exhibited a typical levee breach process. In the meantime, due to changes in the upstream water level the calculated results exhibit secondary variations, which are not obvious in the measurements. In the elapsed time of about 23 min, the increasing trends of breach discharge and breach width were slow down, due to the decrease of the upstream water level. After this, the breach discharge and width increased more rapidly due to the increase of water level and widening of the breach.

The calculated breach flows and breach widths from the two simulations are very close. The water levels at the downstream side calculated in the second simulation agree well with the

measured values after the elapsed time of 23 min, as shown in Fig. 7.22. This indicates the breach model's assumption of a uniform flow at the downstream channel is reasonable in this case. There is some deviation between the calculated and measured downstream water levels in the time period from 10 to 20 minutes. However, this deviation in tailwater level does not affect the simulated breach flow and breach evolution because the breach flow is supercritical.

Table 7.1 Geometries of the Test Dam and Its Clay Core

	Dam body	Core
Height (m)	5.6	5.1
Crest width (m)	4.0	0.8
Upstream slope (V/H)	1/3	1/0.17
Downstream slope (V/H)	1/2.5	1/0.17
Eccentric distance (m)	-	-1.6

Table 7.2 Soil Properties of the Shoulder, Clay Core and Clay Cover Used in the Simulations

	Sand shoulder	Clay core	Clay cover on D/S slope
d_{50} (mm)	0.8 (0.45-1.5)		
Porosity (-)	0.43	0.38	0.38
Clay ratio (-)	0.0	0.29	0.29
Cohesion (kPa)	0.0	21.0 (23.5)	21.0 (23.5)
Internal friction angle	29^o (29^o-38^o)	18^o	18^o
k_d (cm^3/N-s)		3.9	3.9
τ_c (Pa)		0.15	0.15

Note: Values in parentheses are measured.

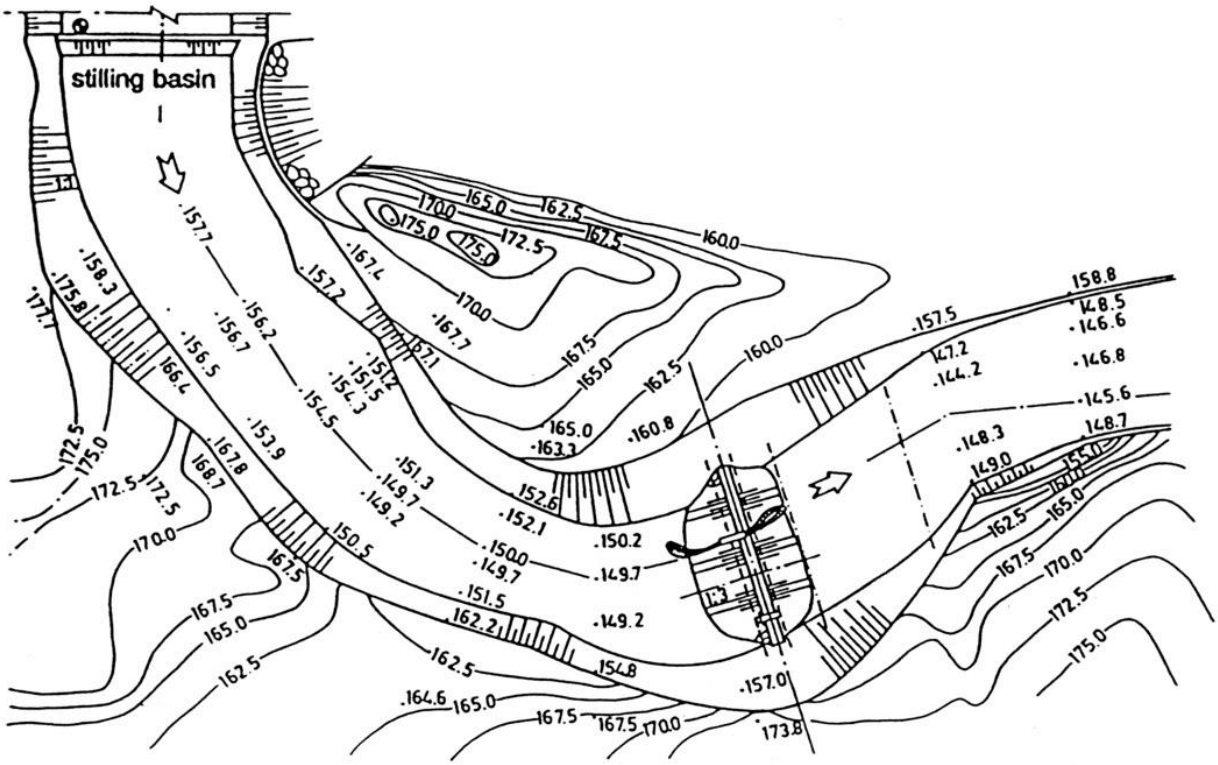

Fig. 7.20 Plan View of the Yahekou Fuse Plug Dam (Pan et al., 1993)

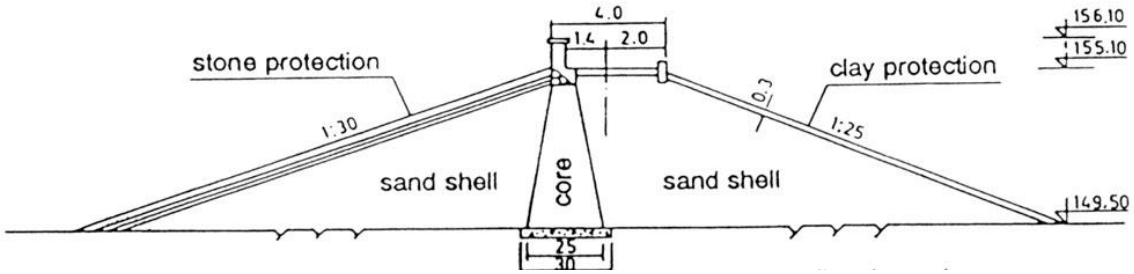

Fig. 7.21 Cross-section of the Yahekou Fuse Plug Dam (Pan et al., 1993)

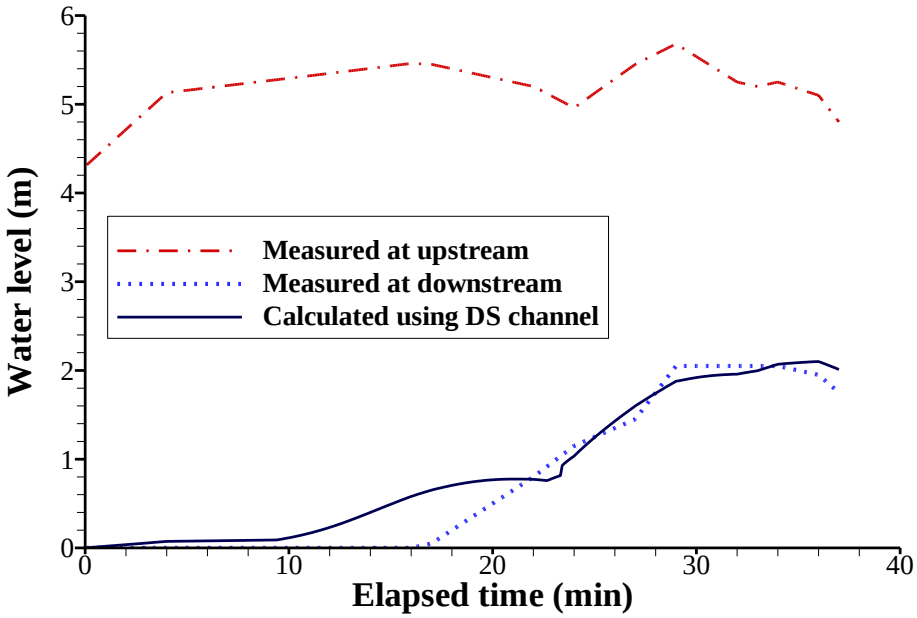

Fig. 7.22 Water Levels Upstream and Downstream of the Yahekou Fuse Plug Dam

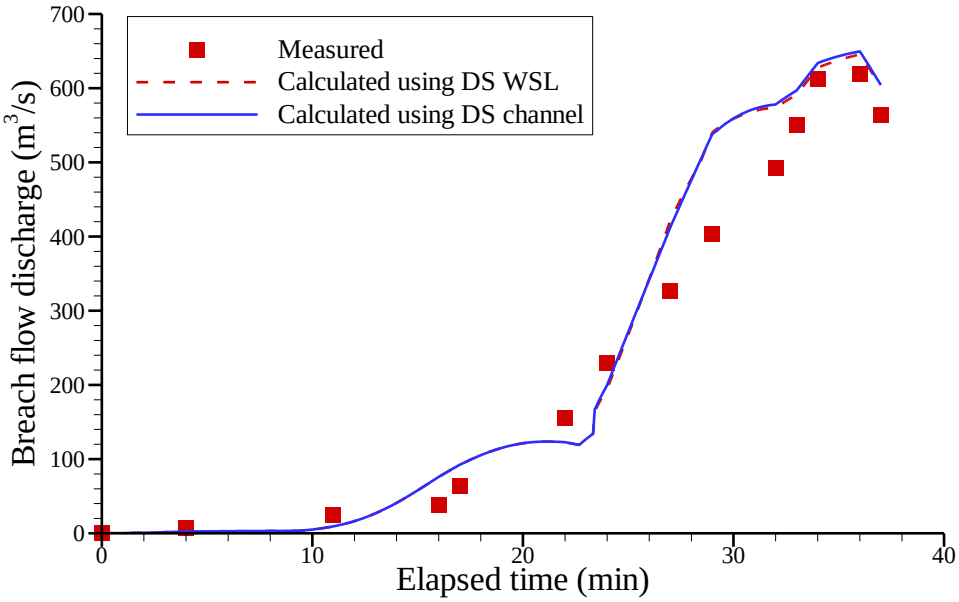

Fig. 7.23 Measured and Calculated Breach Flow Discharges for the Yahekou Fuse Plug Dam Breach Test

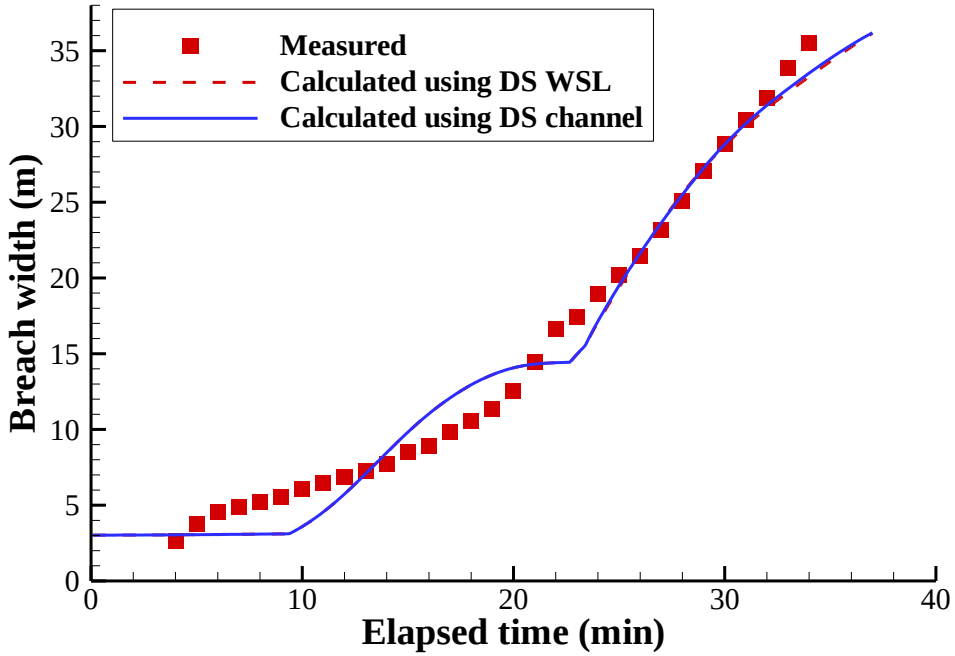

Fig. 7.24 Measured and Calculated Breach Widths for the Yahekou Fuse Plug Dam Breach Test

7.4. Sutter Bypass Levee Breach

A series of storms dumped warm, heavy rains into a nearly double than average snow pack in the Sierra Nevada Mountains in late December 1996, and caused record flows throughout the California Central Valley in early January 1997. High flows on the Sacramento River activated overflow weirs, diverting water into the Sutter Bypass channel. Shortly after the peak flow passed on January 4, 1997, the southwest levee of Sutter Bypass failed suddenly, inundating the Meridian Basin. No problems or seepage were noted at 5:00pm, but the breach was observed and reported by 6:30 pm (Risher and Gibson, 2016). The breach grew rapidly, reaching 30 m in an hour and 150 m by 1:00 am (USACE Sacramento District, 1997; Risher and Gibson, 2016). Aerial photos in the next morning show a breach over 200 m wide and still growing (Flood Emergency Action Team, 1997), see Fig. 7.25. The levee crest was a few meters higher than the river water at the time of breach, indicating the failure was due to piping or seepage. In the following day (Jan 5, 12:00 pm), the levee at the south end of the basin was cut to allow the water to return to the Bypass (Fig. 7.26). This engineered relief breach eventually grew into a full breach. On the evening of 6 January large rip rap stones were dumped on both sides of the levee breach to prevent further erosion (Risher and Gibson, 2016). The final breach was about 274 m (900 ft). The breach reached about 4 m below the levee base. Approximately 50 square miles of the Meridian Basin was inundated. Virtually every facility in the basin was destroyed or

damaged, including nearly 100 homes and a school standing in 4 feet of water (Sutter County, CA, 2015).

Fig. 7.25. Photo of Sutter Bypass Levee Breach (http://ww3.hdnux.com/photos)

Fig. 7.26. Relief Cut of the Levee at the South End of the Meridian Basin Developed to a Full Breach (Photo taken three weeks after the breach)
(http://www.water.ca.gov/historicaldocs/irwm/feat-1997/jand1.html)

The levee was built from dredge spoils in the early 1900s. It was placed wet of optimum and received little compaction. In 1940 the basin was flooded and the landside of the levee was damaged by extensive erosion. The levee was raised and landside repaired using borrow material from the Sutter Bypass. The levee surface material is mostly clay while deeper materials include more silt and sand. This likely left the original levee more pervious than the repair. In 1955 and 1958 boils, ground heaving, and excessive seepage were observed nearby prompting more than 3 km of repairs. The 1997 breach site was just upstream of the 1958 repair work (Risher and Gibson, 2016). The soil layer structures are estimated using boring information, as shown in Fig. 7.27 (Paul Risher, 2016, personal communication). The representative soil in the levee body was silty sand (SM) or clayey sand (SC), considering piping as the breach mode.

The levee embankment height was 6.96 m, and crest width was 6.098 m. The riverside (upstream) slope was 0.303:1 (V/H), and the landside (downstream) slope was 0.357:1. The simulation using DLBreach here assumes an initial pipe of 0.15 m high and wide, located at 0.46 m above the levee toe. The orifice flow equation (3.13) is used to compute the piping flow discharge at the piping stage. The overtopping breaching process was divided into intensive breaching and general evolution periods based on Eq. (3.6). The broad-crested weir equation (3.1) is used for the intensive formation period where supercritical flow is expected. The Keulegan equation (3.3) is used for the general evolution period, in which the flow may be

subcritical and tailwater effect exists. The entrance head loss coefficient is set as 1.0 in the Keulegan equation.

Cohesive sediment erosion model is used in this test case. The soil is assumed to have a diameter of 0.1 mm, porosity of 0.4, clay content of 5%, cohesion of 10 kPa, and internal friction angle of 18^o. The critical shear stress for erosion is set as 0.15 Pa. The soil erodibility k_d is calibrated as 14.5 cm^3/N·s by comparing the calculated and measured breach widths. This k_d value is larger than the value 10.3 cm^3/N·s measured by Hanson et al. (2005) for SM soil. A Manning's n of 0.016 is used. A maximum subbase erosion of about 4 m was observed. Because DLBreach approximates the breach cross-section as a trapezoid, the subbase erosion limit is set as 2 m in the simulation to represent the average bottom elevation.

The volume versus elevation, $V(z)$, curve of Meridian Basin is shown in Fig. 7.29. The curve is obtained by using the 1-foot contour lines generated from a Lidar data collection in 2008 provided by Jarvis Jones, Sutter County Development Services, CA. It is found that Meridian Basin has several roads (Highway 20, Progress Road, etc.), which are about 40-42 ft high. These roads are a few feet higher than the farm lands in the basin, particularly in the south parts of the basin. In order to account for the effect of the roads on the flood propagation, the basin is divided into four zones, as shown in Fig. 7.28. The $V(z)$ relation is calculated for each zone using the 1-foot contours. The breach was located in zone 1. The flood water could reach zones 2, 3, and 4 only after the water level in zone 1 rose above the top of the roads. Therefore, the basin $V(z)$ curve is modified by considering the road effect. The modified basin $V(z)$ curve uses only the curve of zone 1 when the elevation is below 41 ft (i.e., 5 ft above the levee base), and then uses the sum of all the four zones' volumes when the elevation is above 41 ft. The modified basin $V(z)$ curve is also shown in Fig. 7.29 using the red solid line. The regular and modified $V(z)$ curves are tabulated in Table 7.3.

The time series of water levels in the Sutter Bypass Channel at the breach location was calculated by Risher and Gibson (2016) using HEC-RAS. The riverside water level was falling after the flood peak on the Sacramento River and Sutter Bypass Channel, as shown in Fig. 7.30. Fig. 7.30 also shows the times of relief cut of downstream (D/S) levee and dumping of the rip rap stones. The levee at the south end of the basin was cut in Jan. 5 (about 12:00 pm) to allow the water to return to the Bypass. The final geometry of the relief breach is given in Table 7.4. The relief breach is considered in the simulation as weirs with different crest elevations. The weir flow discharge coefficient is set as 1.7.

Two simulations are conducted using the regular and modified basin $V(z)$ curves, while other parameters are the same. Fig. 7.31 compares the calculated and measured breach widths. Both simulations reproduce generally well the measured breach width development, although the simulation using the modified $V(z)$ curve gives somehow better results than using the regular $V(z)$ curve without effect of roads. Each simulation started from 18:00 pm of Jan. 4. In about 10 minutes, the pipe roof failed. This indicates the piping process is not actually simulated. This is normally done by assuming a relatively large initial pipe. On the other hand, the soil does not

have strong cohesion. After the pipe failed, overtopping breach mode took over. Then the breach widened quickly in the first 24 hours, and then the widening died out due to rising of the water level in the basin and falling of the riverside water level. The measured final breach width at the time of rip rap stones dumped is 274 m (900 ft). The calculated breach widths using the regular and modified $V(z)$ curves in the corresponding time are 270.4 and 277.9 m, respectively. The errors are quite small.

Fig. 7.30 shows the calculated basin water levels. The water started to fill the basin when the simulation started. The simulation using the modified $V(z)$ curve gives a faster rising in the basin water level, due to that only zone 1 was used to store the water in the early filling stage. In Jan. 5, 12:00 pm when the south levee was cut for relief, the basin water level calculated using the modified $V(z)$ curve was 2.11 m above the levee base, which is equivalent to 43 ft above the reference datum in the U.S. The ground level of the Meridian Elementary school is about 44 ft. This explains well why the south basin levee was cut to relieve the flood pressure to the town of Meridian. After the relief cut, the basin level still continued to rise until about 12 hours later when the riverside and basin water levels became close. The final basin water level calculated using the modified basin $V(z)$ curve is about 3.66 m above the levee base, i.e. 48 ft above the reference datum. This gives a 4-ft water depth in the Meridian Elementary School ground. This calculation result agrees very well the reported water depth there. This excellent agreement is attributed to the predictions of riverside water level by HEC-RAS as well as the breaching process and basin water filling calculated by the present levee breach model.

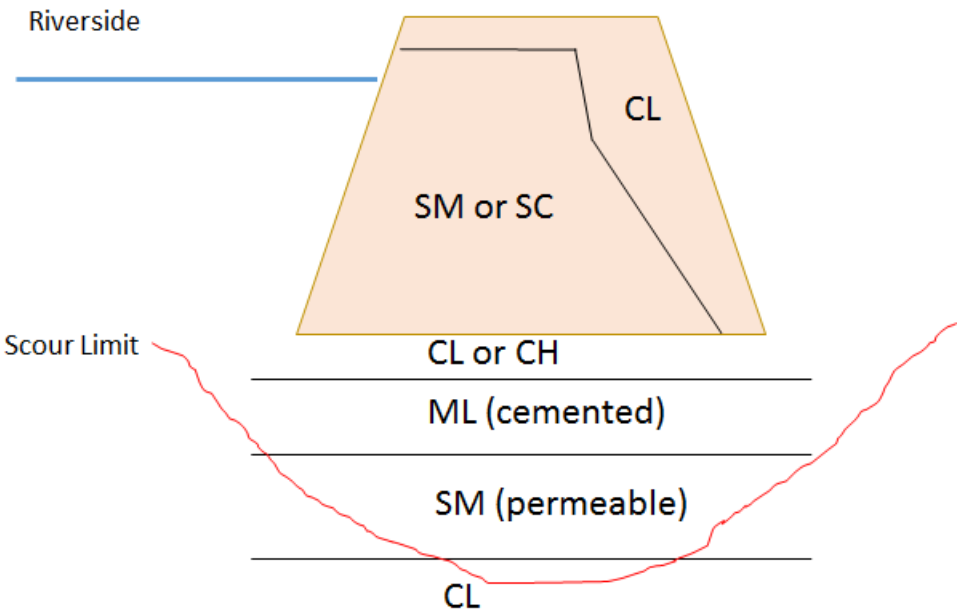

Fig. 7.27. Estimate of Embankment and Foundation Soils (CL – clay, >70% fines; SM – silty sand, 12%-70% fines; SC – clayey sand, 12%-70% fines; ML – silt, >70% fines) (Risher, 2016, personal communication)

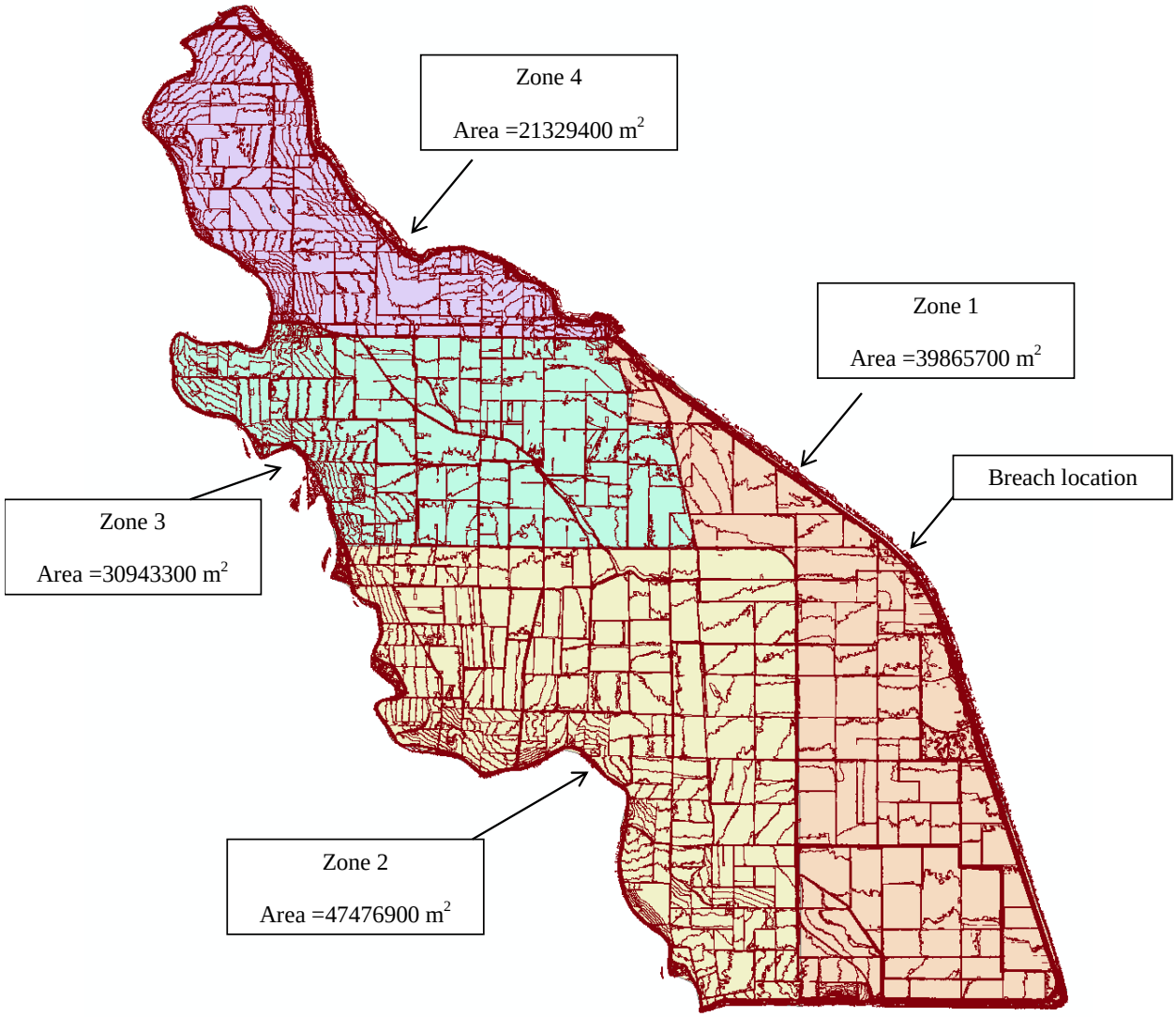

Fig. 7.28. Meridian Basin divided to four zones by roads which are a few feet above the lower farm lands

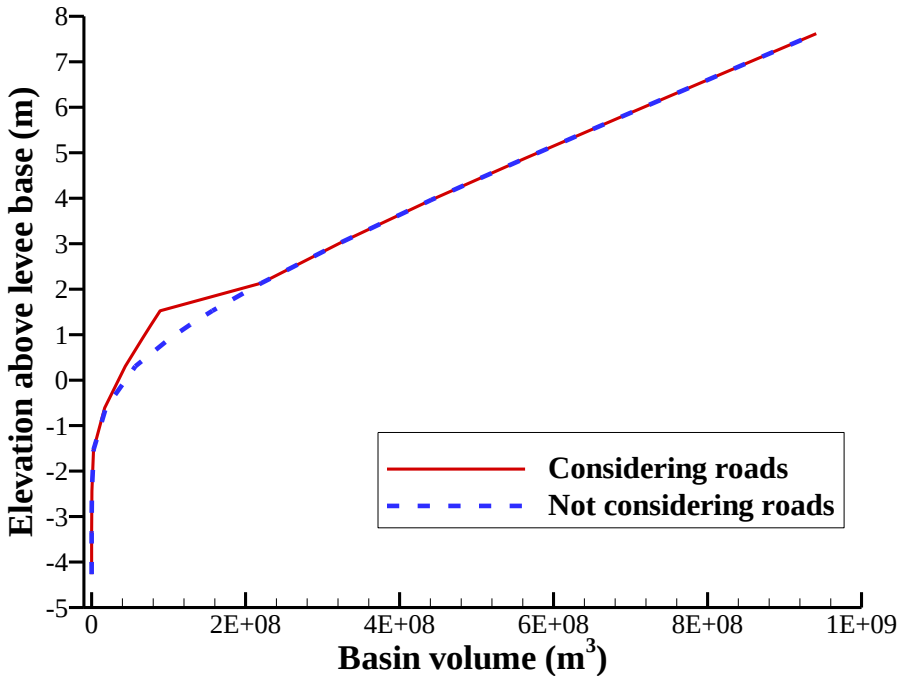

Fig. 7.29. Volume and level *V*(*z*) curve of Meridian Basin (levee base at 36 ft above the U.S. reference datum)

Table 7.3. Meridian Basin Volume vs. Elevation

Elevation		Basin volume (m^3)	
above sea level (ft)	above levee base (m)	without considering roads	with considering roads
22	-4.27	584.9	584.9
25	-3.35	69532.4	69532.4
28	-2.44	399900.7	395979.3
31	-1.52	2580678.7	2509458.1
34	-0.61	18491462.0	16953334.5
37	0.30	56799763.7	43731798.4
39	0.91	101294758.3	65832330.4
40	1.22	127935098.3	77311638.4
41	1.52	156838861.9	88937960.1
43	2.13	220403963.5	220403963.5
46	3.05	326397223.4	326397223.4
49	3.96	441057989.5	441057989.5
52	4.88	562807858.0	562807858.0
55	5.79	687969826.1	687969826.1
58	6.71	814327405.6	814327405.6
61	7.62	941119965.6	941119965.6

Table 7.4. Downstream Relief Breach Geometry (Risher, 2016, personal communication)

Distance (ft)	Distance (m)	Elevation above sea level (ft)	Elevation above levee base (m)
0	0.00	57.3	6.49
105.98	32.41	57.58	6.58
207.45	63.44	57.92	6.68
307.13	93.92	48.92	3.94
311.13	95.14	39	0.91
386.13	118.08	39	0.91
391.13	119.61	49	3.96
466.13	142.54	44	2.44
541.13	165.48	49	3.96
656.13	200.64	49	3.96
661.13	202.17	46	3.05
801.13	244.99	46	3.05
806.13	246.51	49	3.96
934.13	285.66	49	3.96
939.13	287.19	41	1.52
1089.13	333.06	41	1.52
1094.13	334.58	48.81	3.90
1194.36	365.24	57.43	6.53
1261.22	385.68	56.9	6.37

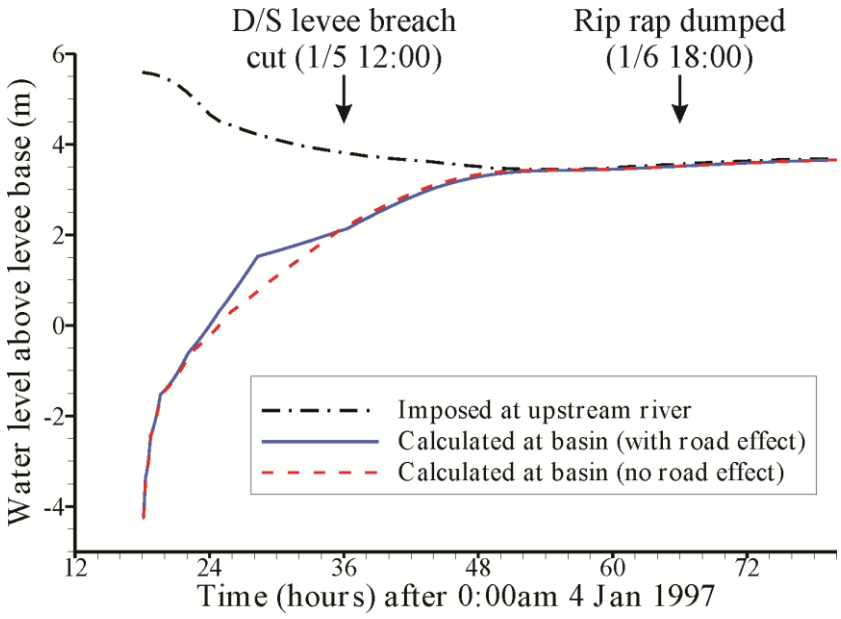

Fig. 7.30. Imposed Riverside Water Level ad Calculated Basin Water Levels, with Timing of D/S Levee Cut and Rip Rap Dumping

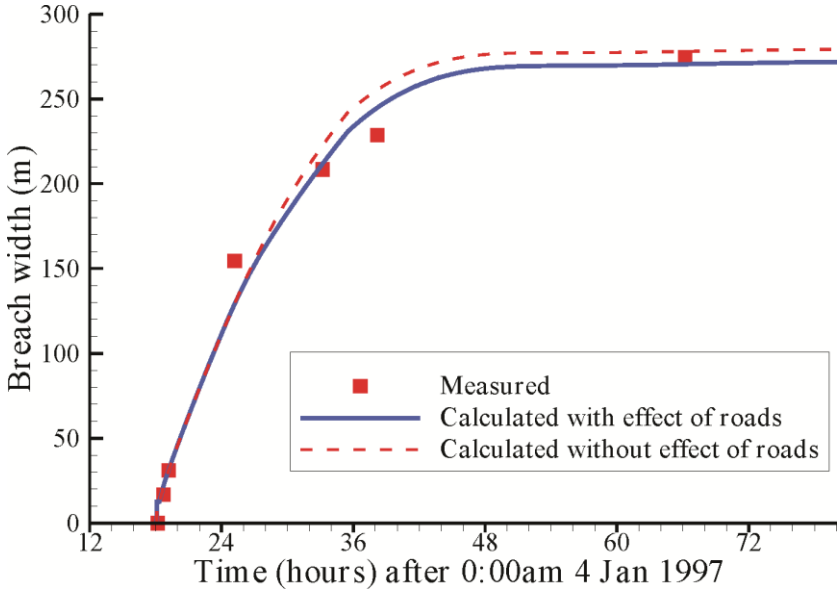

Fig. 7.31. Comparison of Measured and Calculated Breach Widths

Chapter 8. Conclusions

The simplified earthen embankment breach model DLBreach is introduced in this report. The model uses the one-way breach for inland dam and levee breaching by unidirectional flows, and the two-way breach for coastal and estuarine levee and barrier breaching, in which flow may reverse. The model approximates the breach caused by overtopping flow as a flat broad-crested weir with trapezoidal cross-section, upstream and downstream connected with straight slopes ending at the embankment toe in the case of homogeneous non-cohesive embankment and with a headcut in the case of homogeneous cohesive embankment.

The model divides the breaching process into two stages. The first stage is the intensive breaching stage, in which the breach flow is supercritical, controlled by upstream. The second stage is the general breach or inlet evolution stage, in which the flow is subcritical, controlled by downstream or both upstream and downstream. In the first stage the breach flow is calculated using the weir flow equation, and in the second stage the breach flow is calculated using the Keulegan equation. The Keulegan equation is the simplified energy equation for steady nonuniform flow with local head loss due to channel contraction and expansion, added the wind driving force to consider the effect of wind. In the case of piping, the breach flow is assumed through a pipe with a rectangular cross-section at the initial stage and determined using the orifice flow equation until the collapse of the pipe roof, and then overtopping breaching takes place.

The breach model considers wave overtopping. The formula of Hughes and Nadal (2009) is used to calculate the average discharge due to wave overtopping in addition to the surge overflow through the breach in the case that the surge level is higher than the breach bottom elevation. When the surge level is lower than the breach bottom elevation, the average discharge due to wave overtopping is calculated by using the formula of van der Meer and Janssen (1995). The average wave overtopping discharge is added to the surge overflow discharge for the hydrodynamic and sediment routing.

The breach model is able to consider wave and wind setup. The wave setup is roughly assumed to be proportional to the significant wave height. The wind setup is estimated by using the formula of McCartney (1976). The wave setup is added to the sea water level and the wind setup is added on the bay and sea sides when calculating the breach flow discharge.

Sediment transport at the breach flat top section, in the pipe and on the downstream slope is calculated using the analytical solution of the non-equilibrium sediment transport equation, with the sediment entrainment rate determined by the combination of the Wu et al. (2000) bed-load formula and the Zhang (1961) suspended-load formula in cases of non-cohesive sediments and by the linear erosion formula in cases of cohesive sediments. The time-averaged headcut migration rate is determined using the Temple (1992) formula. In the case of composite embankment with clay core and cover, the erosion of downstream non-cohesive (or less cohesive) materials is first calculated using the non-equilibrium sediment transport model until

the clay core is exposed. In addition, the longshore sediment along the adjacent beach is considered as a sediment source from the sea side of the breach, and calculated using the formula of CERC (U.S. Army Coastal Engineering Research Center, 1984) and the formula of Kamphuis (2002).

Stability of the headcut, pipe roof block and clay core are assessed by comparing the driving and resistance forces. The forces considered include the water and soil pressures, flow shear, gravity, friction and cohesion. The stability of breach side slope is also assessed similarly. The breach side slope is between the steepest stable slope and the corresponding failure plane angle and thus set as their average. In order to handle the dam and levee breaching, the model determines the headwater level by routing the water balance in the reservoir or lake or specifying the time series of water levels in the cases of levees, and the tailwater level by using a time series of water levels measured or calculated by another hydrodynamic model, assuming uniform flow in downstream channel, or routing the water balance in the low basin. The model allows erosion of embankment base, which is often encountered in cases of levees and some dams with erodible foundation materials.

DLBreach was first tested using 50 sets of laboratory experiment and field case study data on dam breaching. The calculated breach parameters agree well the measured data. 92.9%, 76.7% and 62.5% of the tested cases have less than 25% errors and the root-mean-square relative errors are 14.5%, 16.5% and 34.1% for the peak breach discharges, breach widths and times. The correlation coefficient R^2 is 0.997, 0.970, and 0.939 for peak breach discharges, breach widths and times, respectively. Shown in the selected representative cases, the temporal evolutions of breach flow, breach width, and upstream water level are reasonably well reproduced by the model.

Then, the model was tested using the Mecox Inlet data collected by Smith and Zarillo (1988). Mecox Inlet is a small tidal inlet at eastern Long Beach, NY. It was opened manually in Sept. 10, 1985 and closed naturally in Sept. 18, 1985. The results for the eight-day breach development and closure are promising. The model has been also tested using the field experiments of sea dike breach in the Zwin Channel Estuary and the Yahekou Fuse Plug Dam breach, as well as a real-life levee breach case in the Sutter Bypass Channel, CA. These four levee and barrier breach cases involved noncohesive, cohesive and composite embankments breached by overtopping and piping in inland and coastal settings. The model has been proven to be stable and reliable.

It is recognized that most field test cases do not have complete information, such as initial breach, soil porosity, clay ratio, cohesion, internal friction angle and erodibility. It is found that the erosion coefficient k_d is the most important parameter in cases where cohesive sediments are dominant. In the thirty-seven test cases with cohesive sediments, the typical k_d values are within 2.5-30 $cm^3/N{\cdot}s$. This range of values is relatively narrow in comparison with the wide range of several orders reported in literature.

Further testing is needed to validate this model, particularly in more cases of levee and barrier breaching with wide varieties of soils and embankment configurations.

References

Allsop, N.W.H.A., Kortenhaus, A., and Morris, M.W. (2007). "Failure mechanisms for flood defence structures." FLOODsite Report T04-06-01, FLOODsite, www.floodsite.net

ASCE/EWRI Task Committee on Dam/Levee Breaching (2011). "Earthen embankment breaching." *J. Hydraulic Eng.*, ASCE, 137(12), 1549–1564.

Bodine, B.R. and Hebler, M.T. (1978). "H7780 – Wave Runup and Wind Setup – Computational Model." Southwestern Division, Corps of Engineers, 1200 Main Street, Dallas, TX.

Briaud, J., Ting, F., Chen, H., Cao, Y., Han, S., and Kwak, K. (2001). "Erosion Function Apparatus for Scour Rate Predictions." J. Geotech. Geoenviron. Eng., 127(2), 105–113.

Broich, K. (1998). "Mathematical modelling of dam-break erosion caused by overtopping." In M. Morris ed. CADAM - Concerted Action on Dambreak Modelling: 2nd Project Workshop, Munich, Germany.

Chee, S.D. (1984). "Washout of spillway dams - channels and channel control structures." *Proc. 1st Int. Conf. on Hydraulic Design in Water Resources Eng*., Southampton, U.K.

Chinnarasri, C., Jirakitlerd S. and Wongwises S. (2004). "Embankment dam breach and its outflow characteristics." *Civil Eng. and Envir. Systems*, 21(4), 247–264.

Cristofano, E.A. (1965). "Method of computing erosion rate of failure of earth dams." U.S. Bureau of Reclamation, Denver, CO.

Dean, R.G. and Walton, T.L. (2010). "Wave setup." Chapter 1, *Handbook of Coastal and Ocean Engineering*, edited by Y.C. Kim, World Scientific.

D'Eliso, C. (2007). "Breaching of sea dikes initiated by wave overtopping: A tiered and modular modeling approach." Ph.D. Dissertation, University of Braunschweig, Germany and University of Florence, Italy.

Engelund, F. and Hansen, E. (1967). *A Monograph on Sediment Transport in Alluvial Streams*, Teknisk Vorlag, Copenhagen, Denmark.

Faeh, R. (2007). "Numerical modeling of breach erosion of river embankments." *J. Hydraulic Eng.*, ASCE, 133(9), 1000–1009.

Fell, R., Wan, C. F., Cyganiewicz, J., and Foster, M. (2003). "Time for development of internal erosion and piping in embankment dams." *J. Geotechnical and Geoenvironmental Eng.*, ASCE, 129(4), 307–314.

Fletcher, B.P. and Gilbert, P.A. (1992). "Center Hill Fuseplug Spillway, Caney Fork River, Tennessee; Hydraulic model investigation." Techn. Rep. HL-92-15, Waterways Experiment Station, U.S. Army Corps of Engineers, Vicksburg, MS, U.S.

Flood Emergency Action Team (1997). Final Report. Governor's Task Force on 1997 Flooding in California.

Foster, M, Fell, R., and Spannagle, M. (2000). "The statistics of embankment dam failures and accidents." *Canadian Geotechnical Journal*, 37(5), 1000–1024.

Franca, M.J. and Almeida, A.B. (2004). "A computational model of rockfill dam breaching caused by overtopping (RoDaB)." *J. Hydr. Res.*, 42(2), 197–206.

Fread, D.L. (1984). "DAMBREAK: The NWS dam break flood forecasting model." National Weather Service (NWS) Report, NOAA, Silver Spring, MA.

Fread, D.L. (1988). "BREACH: An erosion model for earthen dam failures (Model description and user manual)." NOAA, Silver Spring, Maryland.

Fread, D.L. (2001). “Some existing capabilities and future directions for dam-breach modeling/flood routing,” *Proc. FEMA Workshop on Issues, Resolutions, and Research Needs Related to Embankment Dam Failure Analysis*, Oklahoma City, Oklahoma.

Froehlich, D.C. (1995). “Peak outflow from breached embankment dam.” *J. Water Resour. Plan. Manage. Div.*, ASCE, 121(1), 90–97.

Gallegos, H.A., Schubert, J.E., and Sanders, B.F. (2009). “Two-dimensional, high-resolution modeling of urban dam-break flooding: A case study of Baldwin Hills, California.” *Advances in Water Resources*, Elsevier, 32, 1323–1335.

Gee, D.M. (2008). “Comparison of dam breach parameter estimators,” Hydrology Engineering Center, US Army Corps of Engineers, Davis, CA.

Guo, J. (2002). “Logarithmic matching and its application in computational hydraulics and sediment transport,” J. Hydr. Res., IAHR, 40(5), 555–565.

Guza, R.T. and Thornton, E.B. (1981). “Wave setup on a natural beach.” *J. Geophys. Res*., 96(C2), 4133-4137.

Hancox, G.T., Mcsaveney, M.J., Manville, V.R., and Davies, T.R. (2005). “The October 1999 Mt Adams rock avalanche and subsequent landslide dam-break flood and effects in Poerua River, Westland, New Zealand.” *New Zealand Journal of Geology & Geophysics*, 48, 683–705.

Hansen, U.A. (1978). “Wave setup and design water level.” *J. Waterway Port Coast. Ocean Div*., 104(WW2), 227-240.

Hassan, M. and Morris, M.W. (2008). “IMPACT project field tests data analysis.” *FloodSite report T04-08-04*, FLOODsite, www.floodsite.net.

Hanson, G.J., and Cook, K.R. (2004). “Apparatus, test procedures, and analytical methods to measure soil erodibility in situ.” *Applied Engineering in Agriculture*, 20(4), 455–462.

Hanson, G.J., Cook, K.R., and Hunt, S.L. (2005). “Physical modeling of overtopping erosion and breach formation of cohesive embankments.” *Transactions of the American Society of Agricultural Engineers*, 48(5), 1783–1794.

Hanson, G.J., Tejral, R.D., Hunt, S.L., and Temple, D.M. (2010). “Internal erosion and impact of erosion resistance.” Proc. 30th U.S. Society of Dams Annual Conference, Sacramento, California, p. 773-784, CDROM.

Hanson, G.J., Temple, D.M., Hunt, S.L., and Tejral, R.D. (2011). “Development and characterization of soil material parameters for embankment breach.” *Applied Engineering in Agriculture*, 27(4), 587–595.

Harris, G.W. and Wagner, D.A. (1967). “Outflow from breached earth dams.” B. Sci. Thesis, Department of Civil Engineering, University of Utah, Salt Lake City, UT.

Holman, R.A. and Sallenger, A.H. (1985). “Setup and swash on a natural beach.” J. Geophys. Res., 90(C1), 945-953.

Hughes, S.A. and Nadal, N.C. (2009). “Laboratory study of combined wave overtopping and storm surge overflow of a levee.” Coastal Engineering, 56, 244-259.

Javid S. and Mohammadi, M. (2012). “Boundary shear stress in a trapezoidal channel.” Intl. Journal of Engineering, 25(4), 323-331.

Justin, J.D. (1932). Earth Dam Projects, John Wiley & Sons, Inc., New York, p. 345.

Kamphuis, J.W. (2002). Alongshore transport of sand. Proceedings of the 28th International Conference on Coastal Engineering. ASCE, pp. 2330–2345.

Knight, D.W., Demetriou, J.D., and Homed, M.E. (1984). “Boundary shear in smooth rectangular channels.” Agric. Water Manage., 110(4), 405–422.

Kraus, N.C. and Hayashi, K. (2005). "Numerical morphologic model of barrier island breaching." *Proc. 29th Coastal Eng. Conf.*, World Scientific Press, pp. 2120–2132.
Lou, W.C. (1981). "Mathematical modeling of earth dam breaches." Ph.D. Dissertation, Colorado State University, Fort Collins, CO.
Macchione, F. (2008). "Model for predicting floods due to earthen dam breaching. I: Formulation and evaluation; II. Comparison with other methods and predictive use." *J. Hydraul. Eng.*, ASCE, 134(12), 1688–1707.
MacDonald, T.C. and Langridge-Monopolis, J. (1984). "Breaching characteristics of dam failures.'' *J. Hydraul. Eng*., 110(5), 567–586.
Marsooli, R. and Wu, W. (2015). "Three-dimensional finite-volume model of dam-break flows with sediment transport over movable beds." Journal of Hydraulic Engineering, ASCE, 141(1), 04014066, 1–12, DOI: 10.1061/(ASCE)HY.1943-7900.0000947.
McCartney, B.L. (1976). "Wave Runup and Wind Setup on Reservoir Embankments." U.S. Army Corps of Engineers, Office of the Chief of Engineers, ETL 1110-2-221.
McNeil, J., Taylor, C., and Lick, W. (1996). "Measurements of erosion of undisturbed bottom sediments with depth." Journal of Hydraulic Engineering, 122(6), 316-324.
Meyer-Peter, E. and Mueller, R. (1948). "Formulas for bed-load transport," Report on Second Meeting of IAHR, Stockholm, Sweden, 39–64.
Mohamed, A.A.A., Samuels, P.G., Morris, M.W., and Ghataora, G.S. (2002). "Improving the accuracy of prediction of breach formation through embankment dams and flood embankments." *Proc. Int. Conf. on Fluvial Hydraulics (River Flow 2002)*, Louvain-la-Neuve, Belgium.
Morris, M.W. and Hassan, M.A.A.M. (2005). "IMPACT: Breach formation technical report (WP2)." IMPACT, www.impact-project.net
Morris, M.W. and Hassan, M. (2009). "Breach initiation and growth: Physical processes." HR Wallingford, UK, www.floodsite.net.
Morris, M.W., Hassan, M., and Vaskinn, K.A. (2005). "Breach formation technical report (WP2)." *IMPACT Project Report*, HR Wallingford, UK, www.impact-project.net.
Morris, M.W., Kortenhaus, A., and Visser, P.J. (2009). "Modelling breach initiation and growth." *FLOODsite Report T06-08-02*, FLOODsite, www.floodsite.net.
Nogueira, V.D.Q. (1984). "A mathematical model of progressive earth dam failure." *Ph.D. Dissertation*, Colorado State University, Fort Collins, CO.
Orendorff, B.D.E. (2009). "An experimental study of embankment dam breaching." Master Thesis, University of Ottawa, Canada.
Osman, A.M. and Thorne, C.R. (1988). "Riverbank stability analysis, I: Theory," *J. Hydraulic Eng.*, ASCE, 114(2), 134–150.
Pan, S., Mingsen, Q., Wang, L., Guoyi, X., Yongqiang, S., Longda, X., Cuiyu, M., Loukola, E., Pyyny, J., Reiter, P., Rytkonen, T. and Alanko, M. (1993). "Investigation report on dam safety research in China." Chinese-Finnish Cooperative Research Work on Dam Break Hydrodynamics, National Board of Waters and the Environment, Series A 167, Helsinki, 92 p.
Ponce, V.M. (1982). "Documented cases of earth dam breaches." *SDSU Civil Eng. Series*, No. 82149, p. 43, San Diego State University, CA.
Ponce, V.M. and Tsivoglou, A.J. (1981). "Modeling gradual dam breaches." *J. Hydraulics Division*, ASCE, 107(HY7), 829–838.

Powledge, G.R., Ralston, D.C., Miller, P., Chen, Y.H., Clopper, P.E., and Temple, D.M. (1989). "Mechanics of overflow erosion on embankments. I: Research activities; II: Hydraulic and design considerations." *J. Hydraul. Eng.*, ASCE, 115(8), 1040–1075

Pugh, C.A. (1985). "Hydraulic model studies of fuse plug embankments." REC-ERC-85-7, U. S. Bureau of Reclamation, Denver, CO, 33 p.

Ralston, D.C. (1987). "Mechanics of embankment erosion during overflow." Hydraulic Engineering, Proc. 1987 ASCE National Conf. on Hydraulic Eng., Williamsburg, VA, pp. 733–738.

Reeve, D., Chadwick, A., and Fleming, C. (2004). *Coastal Engineering: Processes , Theory and Design Practice*. Spon Press (Taylor & Francis Group), London, UK/New York, USA.

Richards, K. and Reddy, K. (2007). "Critical appraisal of piping phenomena in earth dams." *Bulletin of Engineering Geology and the Environment*, 66(4), 381–402.

Risher1, P. and Gibson, S. (2016). "Applying mechanistic dam breach models to historic levee breaches." FLOODrisk 2016 - 3rd European Conference on Flood Risk Management, Lyon, France

Rozov, A.L. (2003). "Modeling of washout of dams." *J. Hydr. Res.*, 41(6), 565–577.

Sanchez, A. and Wu, W. (2011). "A non-equilibrium sediment transport model for coastal inlets and navigation channels," Journal of Coastal Research, Special Issue, No. 59, pp. 39–48.

Sherard, J.L. (1953). "Influence of soil properties and construction methods on the performance of homogeneous earth dams," Technical Memorandum 645, Bureau of Reclamation, US Department of the Interior, Denver, CO.

Shigematsu, T., Liu, P.L.-F., and Oda, K. (2004). "Numerical modeling of the initial stages of dam-break waves." *J. Hydr. Res.*, 42(2), 183–195.

Sills, G.L., Vroman, N.D., Wahl, R.E., and Schwanz, N.T. (2008). "Overview of New Orleans levee failures: lessons learned and their impact on national levee design and assessment." *J. Geotech. Geoenviron. Eng.*, ASCE, 134(5), 556–565.

Singh, V.P. (1996), *Dam Breach Modeling Technology*, Kluwer Academic Publishes, Dordrecht/Boston/London, p. 242.

Singh, V.P. and Scarlatos, C.A. (1985). "Breach erosion of earthfill dams and flood routing: BEED model." Research Report, Research Triangle Park, N.C.: Battelle, Army Research Office.

Singh, V.P. and Scarlatos, C.A. (1988). "Analysis of gradual earth-dam failure." *J. Hydraulic Eng.*, ASCE, 114(1), 21–42.

Smith, G.L. and Zarillo, G.A. (1988). "Short-term interactions between hydraulics and morphodynamics of a small tidal inlet, Long Island, New York." Journal of Coastal Research, 4(2), 301-314.

Sutter County, CA (2015). Sutter County Operational Area Emergency Operations Plan, ANNEX 5 – Floods and Dam Failure.

Swamee, P.K. and Jain, A.K. (1976). "Explicit equations for pipe-flow problems." J. Hydraulics Division, ASCE, 102(HY5), 657–664.

Temple, D.M. (1992). "Estimating flood damage to vegetated deep soil spillways." *Applied Engineering in Agriculture*, 8(2), 237–242.

Temple, D.M., Hanson, G.J., Neilsen, M.L., and Cook, K.R. (2005). "Simplified breach analysis model for homogeneous embankments: Part 1, Background and model components." *Proc. 25th Annual USSD Conference*, Salt Lake City, Utah.

Temple, D.M., Hanson, G.J., and Neilsen, M.L. (2006). "WINDAM – Analysis of overtopped earth embankment dams." *Proc. ASABE Annual Int. Meeting*, American Society of Agricultural and Biological Engineers, Portland, Oregon.
Temple, D.M. and Moore, J.S. (1994). "Headcut advance prediction for earth spillways." *ASAE Paper No. 94-2540*, St. Joseph, Mich., ASAE.
Tinney, E.R. and Hsu, H.Y. (1961). "Mechanics of washout of an erodible fuse plug." J. *Hydraulics Div.*, ASCE, 87(HY3).
USACE, Sacramento District (1997). Collection of Emergency Situation Reports and Emergency Repair Design Documents. *Unpublished*.
U.S. Army Coastal Engineering Research Center (1984), Shore Protection Manual, U.S. Government Printing Office, Washington, DC.
U.S. Committee on Large Dams (1975). "Lessons from dam incidents, USA." ASCE, New York.
U.S. Department of Agriculture, Natural Resources Conservation Service (USDA-NRCS) (1997). "Chapter 51: Earth spillway erosion model." Part 628 Dams, National Engineering Handbook.
van der Meer, J.W., and Janssen, W. (1995). "Wave run-up and wave overtopping at dikes." In: Kabayashi, Demirbilek (Eds.), *Wave Forces on Inclined and Vertical Wall Structures*. American Society of Civil Engineers, pp. 1–27.
Visser, P.J. (1998). "Breach growth in sand-dikes." *Communications on Hydraulic and Geotechnical Eng*., Report No. 98-1, Delft University of Technology, The Netherlands.
Wahl, T. L. (1998), "Prediction of embankment dam breach parameters-A literature review and needs assessment." *Dam Safety Rep. No. DSO-98-004*, U.S. Dept. of the Interior, Bureau of Reclamation, Denver.
Walder, J.S. and O'Connor, J.E. (1997). "Methods for predicting peak discharge of floods caused by failure of natural and constructed earth dams." *Water Resour. Res.*, 33(10), 2337–2348.
Wang, P., Kahawita, R., Mokhtari, A., Phat, T.M., and Quach, T.T. (2006). "Modeling breach formation in embankments due to overtopping." *ICOLD Conference*, Barcelona, Spain.
Wang, Z. and Bowles, D.S. (2006). "Three-dimensional non-cohesive earthen dam breach model. Part 1: theory and methodology." *Advances in Water Resources*, 29, pp. 1528–1545.
Waymarking. "French Landing Dam," Water Dams on Waymarking.com, http://www.waymarking.com/waymarks/WM1VHW_French_Landing_Dam, visited on April 13, 2012.
Wu, W. (2007), *Computational River Dynamics*, Taylor and Francis, London. UK, p. 494.
Wu, W. (2013). "Simplified physically-based model of earthen embankment breaching", Journal of Hydraulic Engineering, ASCE, 139(8), 837–851.
Wu, W. (2016). Inputs and Outputs of DLBreach – A Simplified Physically-Based Dam/Levee Breach Model (Version 2016.4). Technical Report, Clarkson University, NY.
Wu, W., Marsooli, R., and He, Z. (2012). "A depth-averaged two-dimensional model of unsteady flow and sediment transport due to non-cohesive embankment break/breaching." *J. Hydraulic Eng*., ASCE, 138(6), 503–516.
Wu, W. and Wang, S.S.Y. (2005). "Empirical-numerical analysis of headcut migration." *Int. J. Sediment Research*, 20(3), 233–243.
Wu, W., Wang, S.S.Y. and Jia, Y. (2000). "Nonuniform sediment transport in alluvial rivers," *J. Hydr. Res*., IAHR, 38(6), 427–434.
Xu, Y. and Zhang, L.M. (2009). "Breaching parameters for earth and rockfill dams." *J. Geotech. and Geoenviron. Eng*., ASCE, 135(12), 1957–1969.

Yochum, S.E., Goertz, L.A., and Jones, P.H. (2008). "Case study of the Big Bay Dam failure: accuracy and comparison of breach predictions." *J. Hydraulic Eng*., ASCE, 134(9), 1285-1293, DOI: 10.1061/(ASCE)0733-9429(2008)134:9(1285).

Zhang, R.J. (1961). *River Dynamics*, Industry Press, Beijing, China (in Chinese).

Zhang, R.J. and Xie, J.H. (1993). *Sedimentation Research in China, Systematic Selections*, Water and Power Press, Beijing, China.

Zhu, Y.-H., Visser, P.J., and Vrijling, J.K. (2006). "A model for breach erosion in clay-dikes." in A. Sanchez-Arcilla (Ed.), *Coastal Dynamics 2005: Proc. 5th Int. Conference*, ASCE, Reston, U. S.